Fundamental Studies in Hydrogen-Rich Combustion: Instability Mechanisms and Dynamic Mode Selection

by

Raymond Levi Speth

S.B., Massachusetts Institute of Technology (2003)
S.M., Massachusetts Institute of Technology (2006)

Submitted to the Department of Mechanical Engineering
in partial fulfillment of the requirements for the degree of

Doctor of Philosophy in Mechanical Engineering

at the

MASSACHUSETTS INSTITUTE OF TECHNOLOGY

June 2010

Author .....
Department of Mechanical Engineering
May 3, 2010

Certified by .....
Ahmed F. Ghoniem
Professor
Thesis Supervisor

Accepted by .....
David E. Hardt
Chairman, Department Committee on Graduate Students

Fundamental Studies in Hydrogen-Rich Combustion: Instability Mechanisms and Dynamic Mode Selection

by

Raymond Levi Speth

Submitted to the Department of Mechanical Engineering
on May 3, 2010, in partial fulfillment of the
requirements for the degree of
Doctor of Philosophy in Mechanical Engineering

Abstract

Hydrogen-rich alternative fuels are likely to play a significant role in future power generation systems. The emergence of the integrated gasification combined cycle (IGCC) as one of the favored technologies for incorporating carbon capture into coal-based power plants increases the need for gas turbine combustors which can operate on a range of fuels, particularly syngas, a hydrogen-rich fuel produced by coal gasification. Lean premixed combustion, the preferred high-efficiency, low-emissions operating mode in these combustors, is susceptible to strong instabilities even in ordinary fuels. Because hydrogen-rich fuels have combustion properties which depend strongly on composition, avoiding the dynamics that energize combustion instability across all operating conditions is a significant challenge.

In order to explore the effect of fuel composition on combustion dynamics, a series of experiments were carried out in two optically-accessible laboratory-scale combustors: a planar backward-facing step combustor and an axisymmetric swirl-stabilized combustor. Fuels consisting of carbon monoxide and hydrogen, or propane and hydrogen were tested over a range of equivalence ratios and at various inlet temperatures. Dynamic pressure and chemiluminescence measurements were taken for each case. High-speed video and stereographic particle imaging velocimetry were used to explore the dynamic interactions between the flame and the flow field of the combustor.

Stable, quasi-stable, and unstable operating modes were identified in each combustor, with each mode characterized by a distinct dynamic flame shape and acoustic response which is dependent on the composition of the reactants and the inlet temperature. In both combustors, the quasi-stable and unstable modes are associated with acoustically driven flame–vortex interactions in the combustion-anchoring region. In the planar combustor, the flame is convoluted around a large wake vortex, which is periodically shed from the step. In the swirl-stabilized combustor, the flame shape is

controlled by the dynamics of the inner recirculation zone formed as a result of vortex breakdown. In both cases, the unstable mode is associated with velocity oscillation amplitudes that exceed the mean flow velocity. The apparent similarity between the response curves and flame dynamics in the two combustors indicate that the intrinsic local dynamics—instead of global acoustics—govern the flame response.

Analysis shows that for each combustor, the pressure response curves across a range of operating conditions can be collapsed onto a single curve by introducing an appropriate similarity parameter that captures the flame response to the vortex. Computations are performed for stretched flames in hydrogen-rich fuels and the results are used to explain the observed similarity and to define the form of the similarity parameter. This similarity parameter works equally well for both experiments across fuel compositions and different inlet conditions, demonstrating that it fundamentally embodies the reciprocity between the flow and the combustion process that drives the instability. A linear model of the combustor's acoustics shows that the onset of combustion instability at a particular frequency can be related to a time delay between the velocity and the exothermic response of the flame that is inversely proportional to the local burning velocity. This analysis captures the impact of the fuel composition and operating temperature on the mode selection through an appropriately-weighted strained flame consumption speed, further emphasizing the influence of local transport–chemistry interactions on the system response. This new result confirms the role of turbulent combustion dynamics in driving thermoacoustic instabilities.

Thesis Supervisor: Ahmed F. Ghoniem
Title: Professor

Acknowledgments

First and foremost, I would like to thank my advisor, Ahmed Ghoniem, for his exceptional guidance, expertise, and patience over the years. His consistent encouragement has helped me make this thesis a work I can be truly proud of. I am immensely grateful to him for providing me with the opportunity to do this research and develop my skills in a field which has both fundamental scientific value and current practical relevance. I would also like to thank the members of my thesis committee—Anuradha Annaswamy, Bill Green, and Doug Hart—for their enthusiasm and support.

Many thanks are due to the members of the Reacting Gas Dynamics Laboratory that I have had the pleasure of working with. I would like to thank Youssef Marzouk for being a fantastic role model and mentor during my first year in the group. Murat Altay and Duane Hudgins both deserve my gratitude for the many long hours they spent with me building both of the combustors and running the experiments. Without their help, I would probably still be down in the lab soldering wires together. I would like to thank Santosh Shanbhogue and Zach LaBry for their help with the experiments as well, and wish them the best of luck with their ongoing research.

Of course, none of this would have been possible without the love of my family—my father, Dan; my mother, Pat; and my sister, Roxie. Their life-long support and encouragement has contributed so much to making me who I am, and I simply cannot thank them enough for everything they have done for me. I also want to acknowledge the amazing support that I have received over the years from my entire extended family, especially from my dear grandmother, Marilyn Speth, who passed away last year.

I would like to recognize the many friends I have made since coming to MIT for their camaraderie and their contributions—intentional or otherwise—to this thesis. I would like to thank TB "Lobo" Schardl, Alejandro "Solace" Sedeño, Jessy "Jester" McQuaw, James "Plan B" Wnorowski, Forrest "Apocalypse" Green, and Mark

"Monkeylord" Mascaro[1] for all the Supreme times, and for likely extending the amount of time it took to complete the work contained in this thesis. My thanks go to Heidi Kador, Sam Kendig, and Ash Turza for their friendship and support as well. Finally, I would like to acknowledge James E. Tetazoo III and the inhabitants of the THiRD EAst Traveling Animal Zoo for fostering my interest in experimental combustion dynamics.

[1]This list has been inspected by QAI.

Contents

List of Figures

List of Tables

Chapter 1

Introduction

While coal is the most abundant and least expensive fossil fuel available, and is the primary source of energy for electrical generation in the United States [10], its combustion releases significant quantities of carbon dioxide into the atmosphere. One of the favored technologies for incorporating carbon capture into coal-based power plants is the integrated gasification combined cycle (IGCC) [12]. In an IGCC power plant, pulverized coal is partially oxidized in steam and oxygen to form a synthetic fuel composed primarily of hydrogen and carbon monoxide. After being cleaned of harmful compounds, (e.g., sulfurous compounds and particulates), this synthetic fuel mixture, or syngas, is burned in a gas turbine as part of a combined-cycle configuration [33, 38].

The combustion of hydrogen-rich alternative fuels is thus an important component of the IGCC concept. Lean premixed combustion, the high-efficiency, low-emissions operating mode used in these combustors, is susceptible to strong instabilities even in ordinary fuels [31, 32, 43, 48]. Because hydrogen-rich fuels have combustion properties which depend strongly on composition, avoiding the dynamics that energize combustion instability across all operating conditions presents a significant challenge. The goal of this thesis is to characterize the instability mechanisms associated with

hydrogen-rich combustion, and to develop a model which describes the dependence of dynamic combustor operating modes in terms of fundamental properties of the fuel mixture.

1.1 Hydrogen-Rich Fuels

The combustion properties of syngas are substantially different from the hydrocarbon fuels typically used in utility gas turbines. In particular, syngas flames have wider flammability limits and higher flame speeds than normal hydrocarbon flames, due in large part to their high hydrogen content [59]. These flame properties depend on the syngas composition, and in particular the concentration of hydrogen in the syngas. Previous research has shown that in the case of unstrained hydrocarbon–air flames, hydrogen addition has a relatively small impact on the laminar burning velocity and the lean flammability limit. For mixtures with 10% fuel volume H_2, the increase in burning velocity is typically 5% over a range of equivalence ratios [53]. In contrast, hydrogen enrichment has been shown to substantially increase burning velocity and to inhibit extinction in turbulent and strained flame environments [17, 25, 27].

Because of the complexity of turbulent combustion, it is often useful to employ models based on laminar flames. For example, many models of turbulent flames define a turbulent flame speed which depends on the turbulence intensity and the laminar flame speed [6]. Models of laminar flames may be extended to include the effects of stretch and curvature, which represent the perturbations experienced by a flame in a turbulent environment [36, 52]. Analytical studies have described the impact of stretch on premixed flames, typically using asymptotic analyses and simplified models of flame structure [7, 29, 37]. These studies yield simple expressions for the variation of the burning velocity and flame temperature from their unstretched values, emphasizing the interaction of stretch with preferential diffusion (i.e. non-unity Lewis

number) effects. Other investigators have studied the effect of syngas composition on laminar flame speeds, but these studies do not consider syngas mixtures as lean as those examined here [5, 40].

In the case of an IGCC power plant, one can envision a system where the gasification process is adjusted to produce specific syngas compositions to improve the ability of the system to handle a wide range of loads. In other cases, it may be desirable to separate some of the hydrogen from the syngas for alternative uses. Furthermore, there are long startup transients associated with the gasifier, during which there will be variations in the composition of the syngas [39]. It is therefore expected that syngas combustion systems will be required to operate over a wide range of fuel compositions, with corresponding variations in combustion properties.

1.2 Combustion Instability

Lean premixed combustion is the preferred operating mode for combustors in modern utility gas turbines, driven primarily by the need to meet increasingly stringent emissions regulations on pollutants, particularly CO and NO_x. In premixed combustors, the flame is anchored aerodynamically in a recirculation zone which brings the hot product gases into contact with the unburned mixture. These recirculation zones may be generated by a sudden expansion of the flow, in the wake of a bluff body, or as a result of vortex breakdown in a swirling flow.

Combustion instability is a major concern in continuous combustion systems, where pressure oscillations may couple with the heat release dynamics to form a positive feedback loop. A necessary condition for combustion instability to occur in a combustor is the pressure of in-phase oscillations of the heat release rate and the pressure. This result, known as the Rayleigh criterion [44], may be expressed in terms

of a Rayleigh index:

$$R = \frac{1}{\tau} \int_0^\tau \int_V p'(\mathbf{x}, t) q'(\mathbf{x}, t)\, dV\, dt \tag{1.1}$$

where p' and q' are perturbations in the mean pressure $\bar{p}$ and heat release rate $\bar{q}$, such that $p = \bar{p} + p'$ and $q = \bar{q} + q'$. When the Rayleigh index R is positive, the heat release rate and pressure oscillations are in phase and the instability grows if dissipation is weak. When the Rayleigh index is negative, oscillations in pressure and heat release are out of phase, and consequently damped.

In order for the Rayleigh index to be non-zero, there must be some physical mechanism present which couples the heat release and pressure oscillations. Previous research has identified several such mechanisms, including equivalence ratio oscillations [32] and flame–vortex interactions [43, 48]. Equivalence ratio oscillations may be produced when the pressure oscillations in the combustor affect either the fuel or air flow rate into the combustor, e.g., if either the fuel or air supply is not choked, or if the fuel is injected at a point where the pressure oscillations have produced oscillations in the velocity. This action produces spatial variations in the equivalence ratio, which in turn produce temporal variations in the heat release rate as the mixture is convected to the flame front [2].

Flame–vortex interactions can lead to combustion instability when vortex shedding, e.g., downstream of a combustor's sudden expansion, is driven by the velocity oscillations which accompany the pressure oscillations in the combustor [55]. The flame surface is convoluted by interaction with the periodically shed vortex, and the resulting changes in flame surface area couple the heat release rate to the pressure oscillations. Additionally, the stretching and convoluting of the flame surface by vortices alter the flame structure, and consequently the flame speed and the heat release rate. Fritsche et al. [16] observed several stable and unstable flames according to the equivalence ratio and inlet temperature in a swirl-stabilized combustor using

methane. They observed that the transition from stable to unstable combustion was also associated with a change in flame position and shape, pointing to the existence of different flame stabilizing mechanisms dependent on the characteristics of the reactants mixture. Wicksall and Agrawal [57] studied the effect of hydrogen enrichment on the stability of hydrocarbon flames. They found that when sufficient hydrogen is added to methane, the combustion becomes unstable and the flame becomes more compact. Moreover, adding hydrogen reduces the lean blowout limit significantly. Because hydrogen-rich fuels have combustion properties which depend strongly on composition, avoiding the dynamics that energize combustion instability across all operating conditions is a significant challenge.

1.3 Thesis Outline

We begin our study of hydrogen-rich combustion in Chapter 2 by formulating a numerical model of a strained flame stabilized in a planar stagnation flow. We use this model to compute strained flame speeds for a wide range of carbon monoxide–hydrogen mixtures and propane–hydrogen mixtures, over a range of equivalence ratios, inlet temperatures, and strain rates. The parameter space was chosen to encompass the conditions used in the experiments discussed in Chapters 3 and 4. We show that hydrogen has a significant impact on the flame response to stretch as a result of preferential diffusion effects which are proportional to the Lewis number of the fuel, and that the effects of hydrogen are strongest for mixtures near the lean flammability limit.

In Chapter 3, we explore the combustion dynamics observed in a laboratory scale, atmospheric pressure, lean premixed, axisymmetric swirl-stabilized combustor using hydrogen–carbon monoxide mixtures with various compositions as fuels. We use dynamic pressure, chemiluminescence, and particle imaging velocimetry measurements

to identify a series of distinct operating modes in the combustor as a function of the fuel composition, equivalence ratio, and inlet temperature. We develop a similarity transformation which captures the flame response to flow oscillations, demonstrating the role of turbulent combustion dynamics in driving thermoacoustic instabilities.

Chapter 4 covers a set of experimental results obtained in a backward-facing step combustor using propane–hydrogen mixtures with various compositions as fuels. As in the swirl-stabilized combustor, a sequence of stable and unstable operating modes are identified as a function of the various inlet parameters, and we apply a similarity transformation based on the density-weighted flame speed to collapse the dynamic mode data. The similarities in the operating modes of the two combustors, and the reduction of each combustor's response curves using related similarity transformations emphasizes the fundamental dependence of combustion dynamics on the local transport–chemistry interactions which govern flame propagation.

Chapter 2

Strained Flames

In order to understand the combustion dynamics of premixed syngas flames in the complex, turbulent environment of practical combustors such as those discussed in Chapters 3 and 4, it is helpful to start by studying the characteristics of flames in a simpler environment. The laminar strained flame can be thought of as a locally accurate model for combustion in a turbulent environment, where the influence of the surrounding turbulent flow field is reflected in the stretch rate imposed on the flame. The motion of the flame front can be decomposed into components representing translation, rotation, and stretch. Of these, only stretch alters the structure of the flame, and consequently alters the burning speed [35].

The stretch of a flame surface element δA is defined [8] as:

$$\kappa \equiv \frac{1}{\delta A}\frac{d\delta A}{dt} = \nabla_t \cdot \mathbf{v}_t + (\mathbf{V}\cdot\mathbf{n})(\nabla\cdot\mathbf{n}) \tag{2.1}$$

where $\mathbf{v}_t$ is the flow velocity tangential to the flame surface, $\mathbf{V}$ is the velocity of the flame, and $\mathbf{n}$ is the unit normal vector of the flame surface, pointing toward the reactants. Numerous analytical studies have described the impact of stretch on premixed flames, typically using asymptotic analyses and simplified models of flame structure [7, 13, 29, 37]. These studies yield simple expressions for the variation of

burning velocity and flame temperature from their unstretched values, emphasizing the interaction of stretch with preferential diffusion (non-unity Lewis number) effects. In particular, Law [29] gives the following linearized expressions for the burned temperature and flame speed of a stretched flame:

$$\frac{T_b}{T_b^o} = 1 + \left(\frac{1}{Le} - 1\right) Ka \tag{2.2}$$

$$\frac{S_u}{S_u^o} = 1 - \delta_T^o \boldsymbol{\nabla} \cdot \mathbf{n} + \left(\frac{1}{Le} - 1\right) \frac{Ka}{2T_b^o/T_a} \tag{2.3}$$

where the Karlovitz number is $Ka = (\delta_T^o/S_u^o)\,\kappa$. S_u^o and T_b^o are the flame speed and burned temperature of the unstretched flame, respectively. δ_T^o is the thermal thickness of the unstrained flame, and T_a is the activation temperature for the reaction.

For hydrogen-rich fuels such as syngas, where the Lewis number is significantly less than unity, Equation 2.3 shows that there should be a significant increase in flame speed for positively stretched flames.

2.1 Numerical Formulation

In this chapter, we will use numerical simulations of strained flames to investigate the burning properties of syngas and propane–hydrogen fuel mixtures. The flame simulated here is a laminar flame stabilized in a planar stagnation flow, as shown in Figure 2.1. Reactants are supplied on one side, products are supplied on other, and the flame stabilizes in the vicinity of the stagnation point. The products supplied in the counterflow are the equilibrium products at the adiabatic flame temperature corresponding to the supplied reactants mixture. The resultant potential flow velocity field is characterized by the time-varying strain rate parameter a. The stretch rate of the planar flame under steady conditions is simply $\kappa = a$.

The one-dimensional governing equations for the flame structure are found by

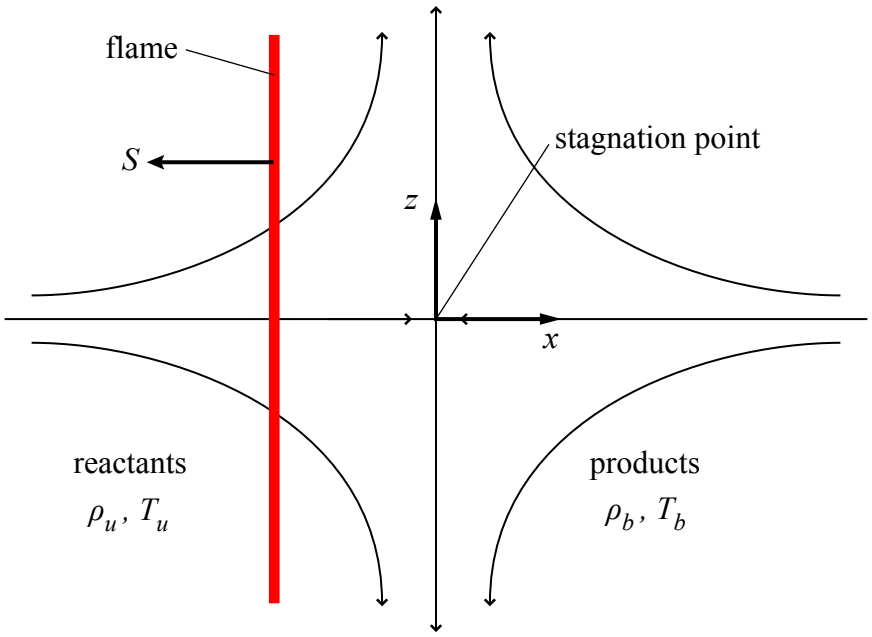

Figure 2.1: Schematic of a strained flame stabilized in a planar stagnation point flow.

using a boundary layer approximation across the flame thickness. The governing equations are solved numerically using an implicit finite difference method. The equations are discretized spatially on an adaptive non-uniform grid, producing a system of differential algebraic equations. The discretized equations are integrated using the Sundials IDA solver [22]. The IDA solver integrates the equations using the variable-order backward differentiation formula (BDF). At each timestep, this produces a system of nonlinear algebraic equations, which are solved using a preconditioned Newton–Krylov method (typically BiCGStab) [54]. Thermodynamic properties, transport coefficients, and chemical kinetic rates are calculated using the Cantera library [20]. Because of its strong influence on the diffusion of hydrogen, the Soret contribution to diffusive fluxes is included. Details of the numerical method may be found in previous papers [36, 52]. For the simulations of syngas flames, we use a modified version of the GRI-Mech 3.0 kinetic model [50] consisting of 50 reactions among 14 species, where the nitrogen-containing species and hydrocarbon species (with the exception of HCO) have been removed to control the computational cost.

For the simulations of propane–hydrogen flames, we use a mechanism developed by Williams with 235 reactions among 46 species [58].

There are many possible ways to define a flame speed for a strained flame. Here, we use the consumption speed S_c found by integrating the energy equation across the flame. The consumption speed is defined as:

$$S_c \equiv \frac{\int_{-\infty}^{\infty} q'''/c_p \, dy}{\rho_u (T_b - T_u)} \tag{2.4}$$

where q''' is the volumetric heat release rate, c_p is the specific heat of the mixture, y is the coordinate normal to the flame, ρ_u is the unburned mixture density, and T_u and T_b are the unburned and burned temperature, respectively. As the strain rate parameter a approaches 0, the consumption speed approaches the laminar burning velocity. The consumption speed defined based on the heat release rate rather than the fuel consumption rate is used because it provides a consistent definition of flame speed for multi-component fuel mixtures.

2.2 Syngas Flames

To understand the effects of stretch on syngas flames, we ran a comprehensive set of numerical simulations covering fuel compositions from 20% CO and 80% H_2 by volume to 80% CO and 20% H_2 by volume in increments of 10%, equivalence ratios ranging from 0.20 to 0.60 in increments of 0.05, inlet temperatures ranging from 300 K to 500 K in increments of 100 K, and strain rates ranging from 10 s^{-1} to 4800 s^{-1}. In all cases, the oxidizer was air and the pressure was atmospheric. The specific fuel mixtures and reactant temperatures considered here are chosen to correspond to the experimental conditions used in Chapters 3 and 4.

The laminar burning velocity as a function of equivalence ratio for each syngas composition considered is shown in Figure 2.2. The laminar burning velocity is

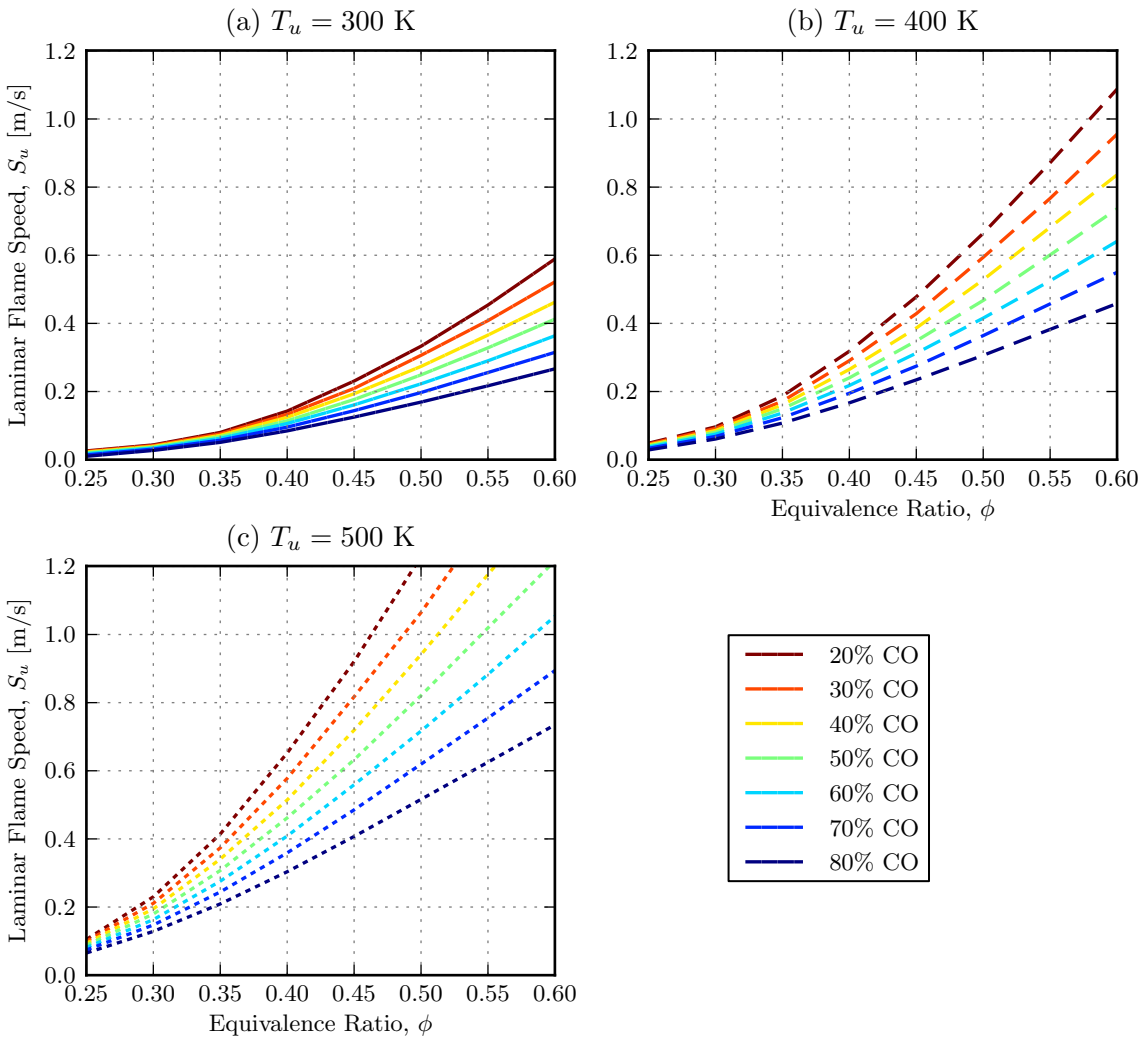

Figure 2.2: Laminar flame speeds for syngas flames.

determined by extrapolating the consumption speed to a strain rate of zero, analogous to the commonly-employed technique for determining laminar burning velocity from experimentally-observed strained flames. For the equivalence ratios considered here, altering the fuel composition results in approximately doubling the burning velocity as the CO:H_2 ratio changes from 80:20 to 20:80. For intermediate compositions, the burning velocity increases essentially linearly with hydrogen concentration in the fuel. The substantial rise in burning velocity with increasing hydrogen concentration occurs despite a slight drop in adiabatic flame temperature, as shown in Figure 2.3.

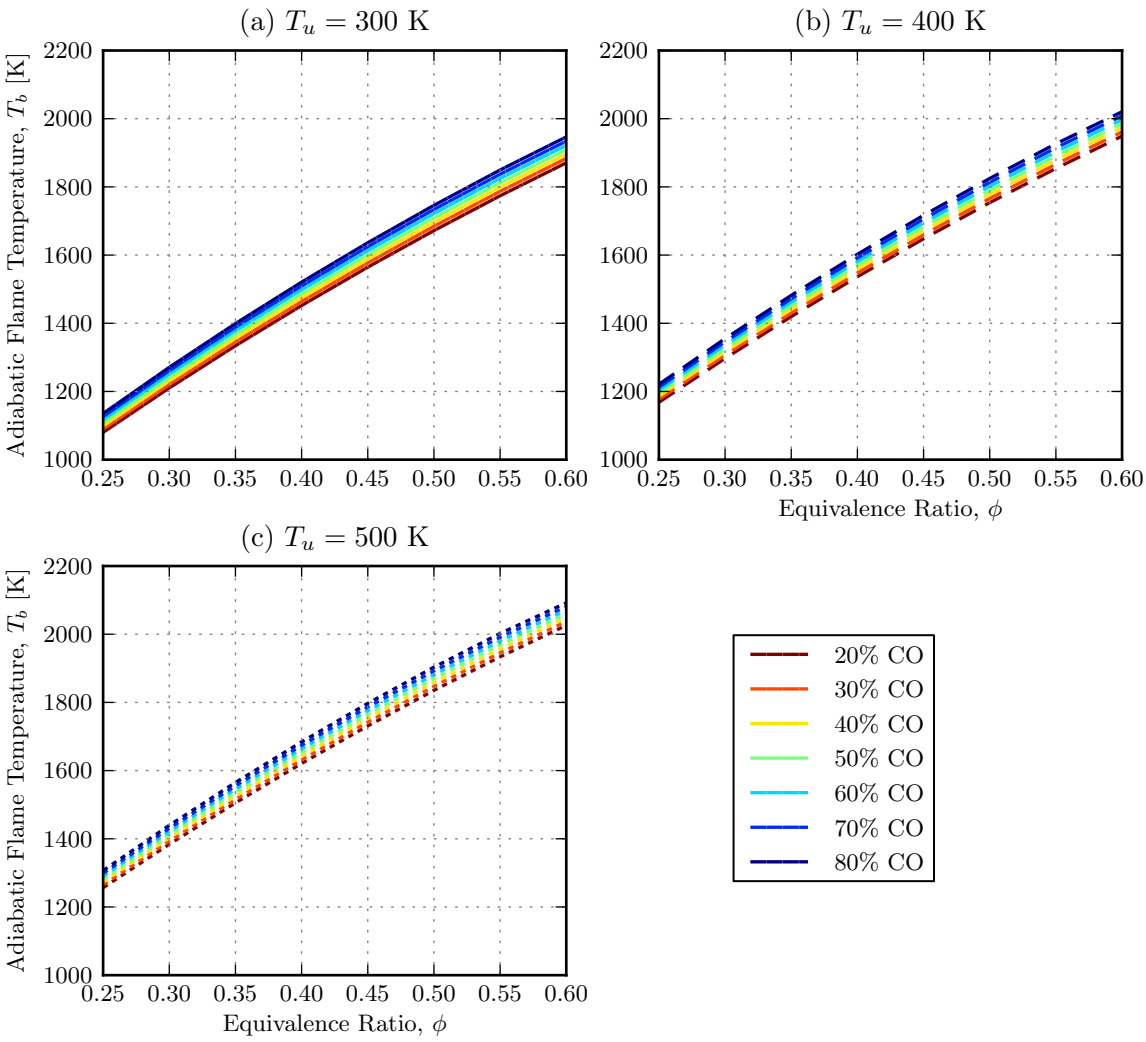

Figure 2.3: Adiabatic flame temperatures for syngas flames.

Figure 2.4 shows the effect of strain rate on flames with equivalence ratio $\phi = 0.40$ at each of the fuel compositions considered. Asymptotic analysis of strained flames predicts that the consumption speed of flames with Lewis numbers less than unity will increase with positive strain, and that the increase will be proportional to the departure of the Lewis number from unity [29]. The results shown in this figure are concordant with the expected trend, with the consumption speed of the highest hydrogen-content (lowest Lewis number) flames having the strongest positive response to increasing strain rate. Preferential diffusion effects associated with Le < 1 flames

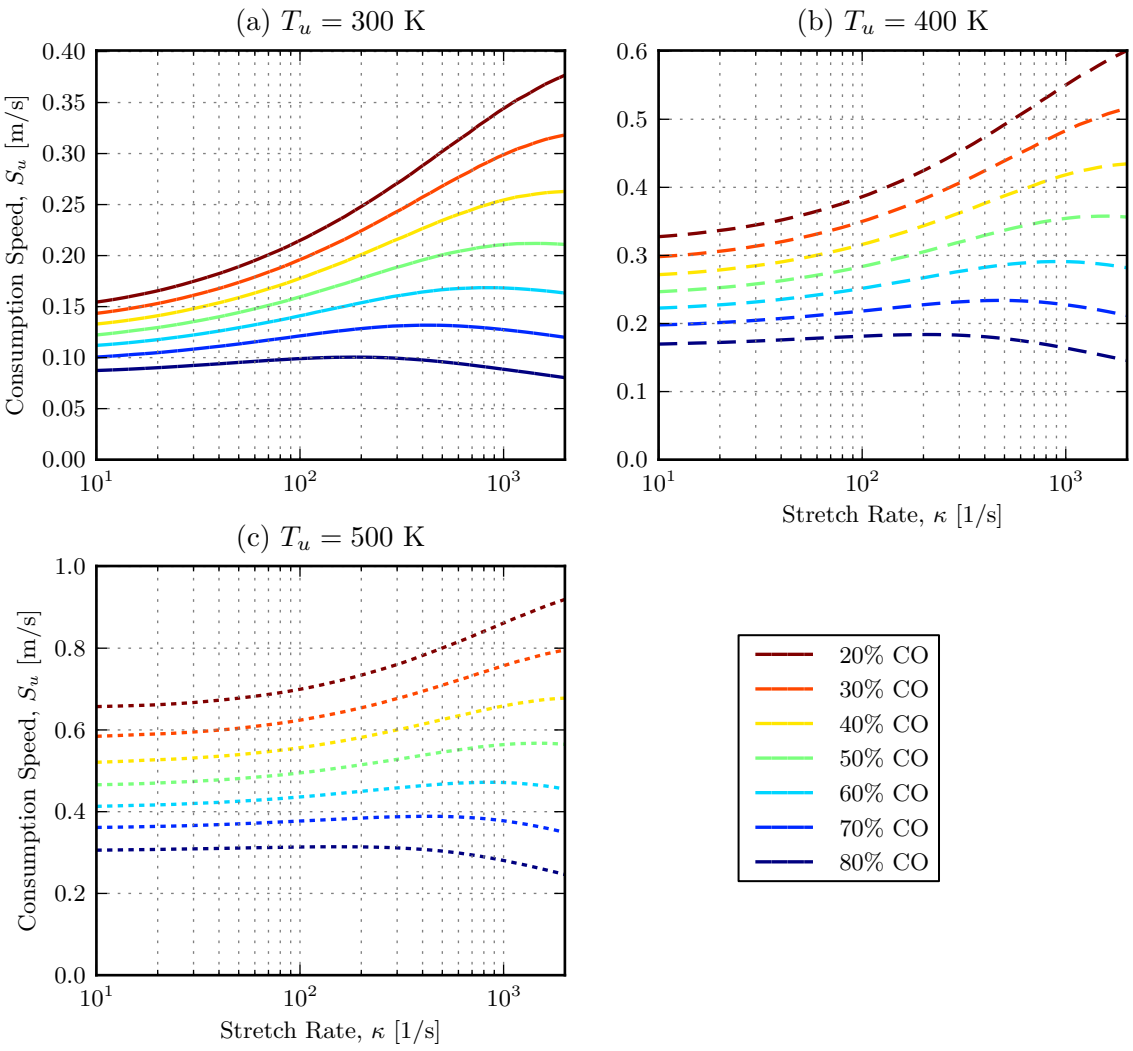

Figure 2.4: Effect of stretch on consumption speed of syngas flames at $\phi = 0.40$.

lead to local flame temperatures which exceed the adiabatic flame temperature, as shown in Figure 2.5.

In Figure 2.6, we plot the consumption speed as a function of equivalence ratio for syngas flames of each composition at a stretch rate of $\kappa = 250$ s^{-1}. When compared with the laminar burning velocities plotted in Figure 2.2, the consumption speeds of flames at the higher equivalence ratios, near $\phi = 0.60$, are nearly unchanged by the strain. Under very lean conditions, the strained hydrogen-rich flames have substantially higher consumption speeds than their unstrained equivalents, while the

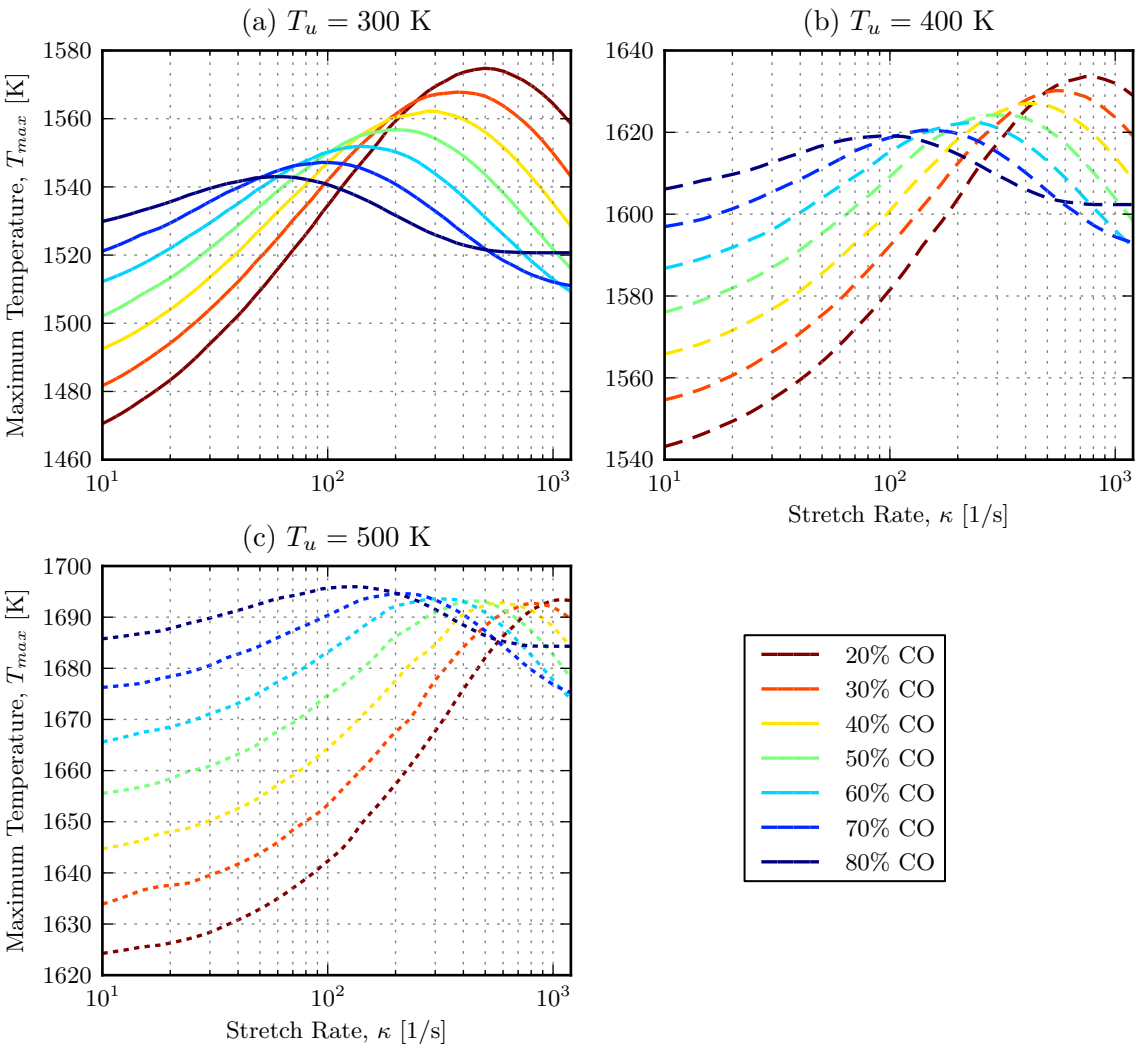

Figure 2.5: Maximum flame temperature as a function of stretch for syngas flames at $\phi = 0.40$.

strained flames with little hydrogen see only marginal increases in consumption speed. The Lewis number dependent response of consumption speed to stretch is greater under ultra-lean conditions than at higher equivalence ratios. One of the peculiar features of strained flames with multicomponent fuels is that the consumption rate of each fuel component is not necessarily proportional to its abundance in the fuel

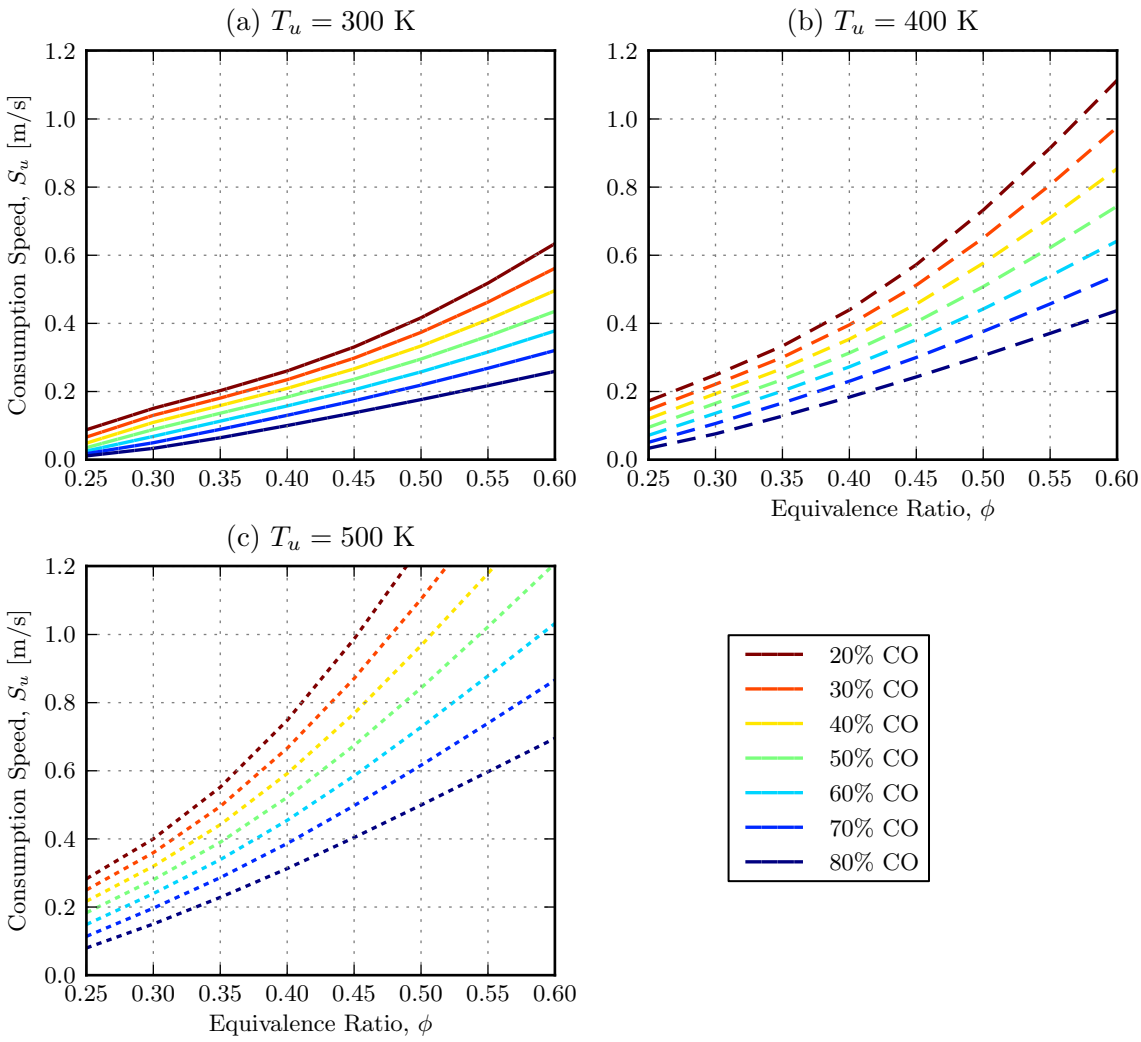

Figure 2.6: Consumption speeds for syngas flames at $\kappa = 250\,\mathrm{s}^{-1}$.

mixture. The consumption ratio ψ_k of species k can be defined as:

$$\psi_k \equiv \frac{\int_{-\infty}^{\infty} \dot{\omega}_k \, dx}{X_{k,f} \sum_{j \in \text{fuel}} \int_{-\infty}^{\infty} \dot{\omega}_j \, dx} \tag{2.5}$$

where $\dot{\omega}_k$ is the molar production of species k and $X_{k,f}$ is the mole fraction of species k in the fuel mixture. When $\psi_k = 1$, species k is being consumed proportionally; when $\psi_k < 1$, less of species k is being consumed. In Figure 2.7, the consumption ratio for CO in syngas flames at various equivalence ratios is shown as a function of strain

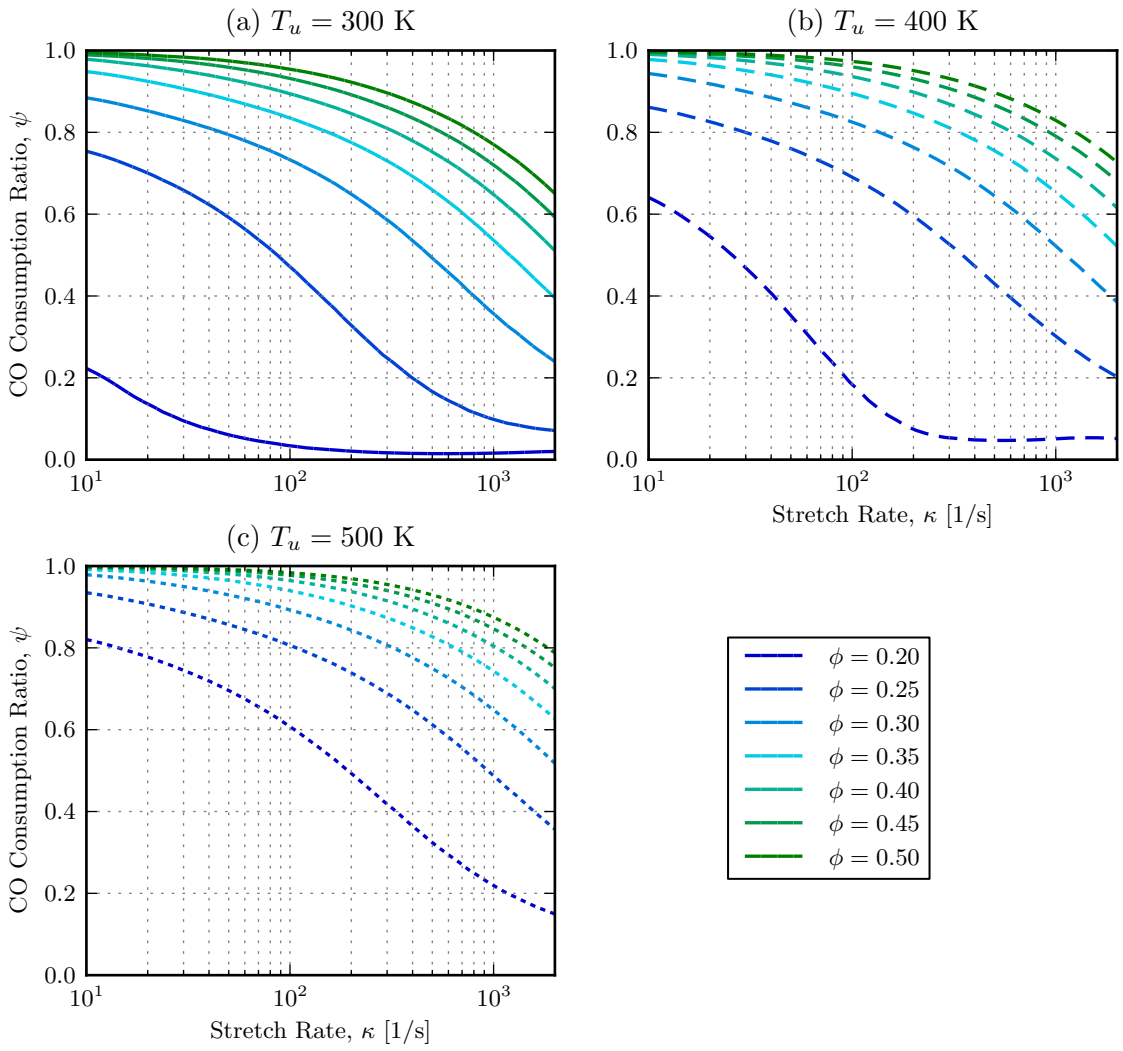

Figure 2.7: Carbon monoxide consumption ratio as a function of stretch for syngas flames with a 40:60 CO:H_2 ratio.

rate and inlet temperature. The consumption ratio is near unity at low strain rates for mixtures that are well above the lean flammability limit. However, introducing strong strain or reducing the equivalence ratio can lead substantial reductions in the consumption of carbon monoxide, even in flames that still have a non-negligible burning velocity.

2.3 Propane–Hydrogen Flames

To understand the effects of stretch on propane–hydrogen flames, we ran a set of numerical simulations covering fuel compositions with C_3H_8:H_2 ratios of 50:50, 70:30 and 100:0 by volume, equivalence ratios ranging from 0.50 to 0.90 in increments of 0.05, inlet temperatures ranging from 300 K to 600 K in increments of 100 K, and strain rates ranging from 10 s^{-1} to 4800 s^{-1}. In all cases, the oxidizer was air and the pressure was atmospheric. The specific fuel mixtures reactant temperatures considered here are chosen to correspond to the experimental conditions used in Chapter 4.

Figure 2.8 shows the laminar flame speeds for propane–hydrogen flames as a function of equivalence ratio for several different inlet temperatures and fuel compositions. As expected, the flame speed increases with equivalence ratio, inlet temperature, and hydrogen concentration. The increase in flame speed is strongest for leaner mixtures, and tapers off as the mixture approaches stoichiometry. Figure 2.9 shows the adiabatic flame temperatures for the same range of equivalence ratios, inlet temperatures, and fuel compositions shown in Figure 2.8. As in the case of syngas, the adiabatic flame temperature is relatively insensitive to fuel composition. However, unlike syngas flames, increasing hydrogen concentration in the fuel produces a slight increase in the flame temperature. As the inlet temperature is increased, the burned gas temperature increases by a smaller amount because the specific heat capacity of the products is higher than that of the reactants.

The consumption speeds of propane–hydrogen mixtures with different compositions and at different inlet temperatures with a fixed equivalence ratio of $\phi = 0.70$ are shown as a function of stretch rate in Figure 2.10. As expected, the flame speeds are higher for the hydrogen-enriched mixtures under all conditions. Unlike syngas flames, however, there is no strain rate for which the flame speed exceeds the laminar flame speed for any fuel composition or inlet temperature. This implies that even for the

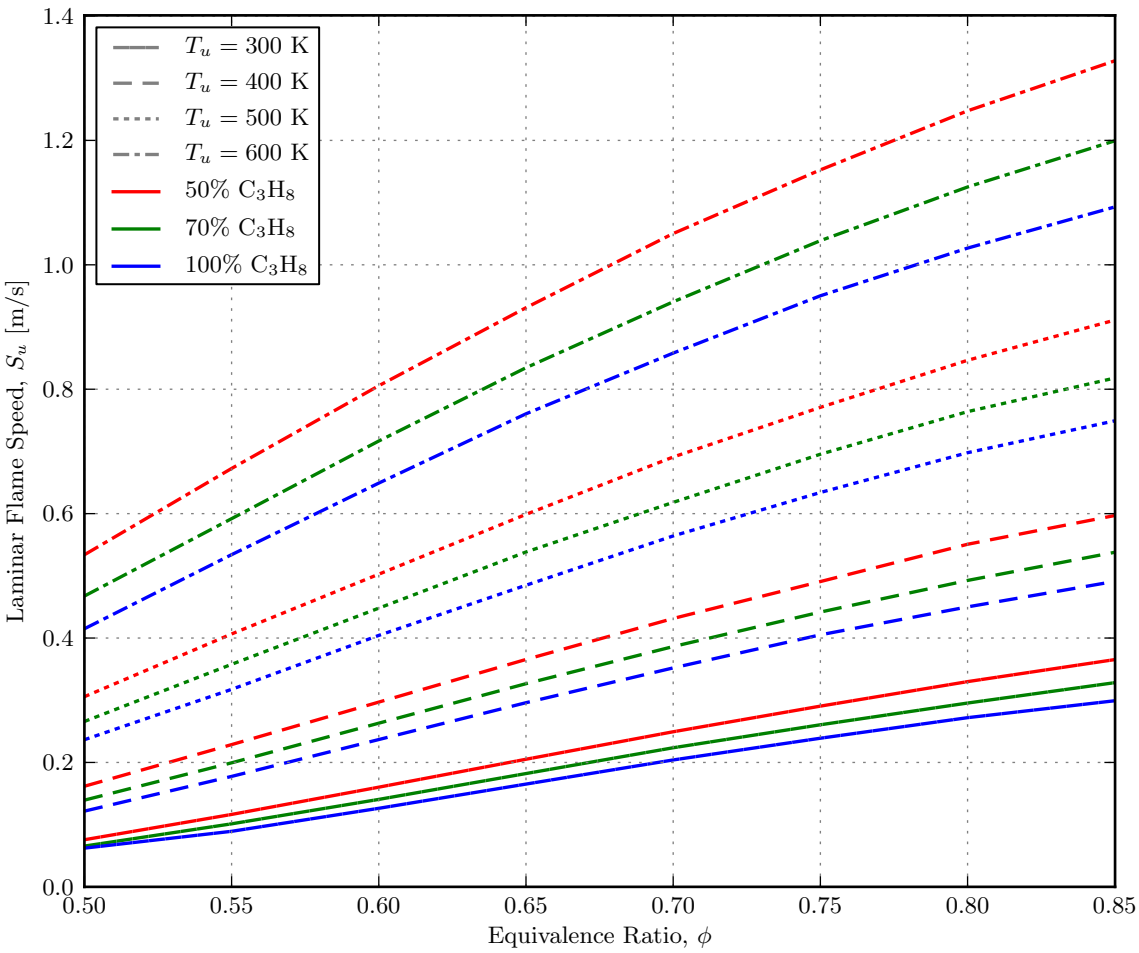

Figure 2.8: Laminar flame speeds for propane–hydrogen fuel mixtures.

fuel mixtures which are 50% hydrogen by volume, the effective Lewis number is still greater than unity. The effects of hydrogen are strongest at high stretch rates, where the flame speeds of the hydrogen-rich flames drop off more slowly with stretch than the flame speeds of the pure propane flames.

Figure 2.11 shows the consumption speeds of propane–hydrogen flames as a function of equivalence ratio for different fuel compositions and inlet temperatures at a fixed stretch rate of $\kappa = 400\,\mathrm{s}^{-1}$. As in the case of syngas flames, the effect of hydrogen addition on flame speed is strongest for lean mixtures. Whereas the laminar flame speeds for fuels with different hydrogen concentrations, shown in Figure 2.8, diverged with increasing equivalence ratio, when the flame is exposed to moderate stretch, the

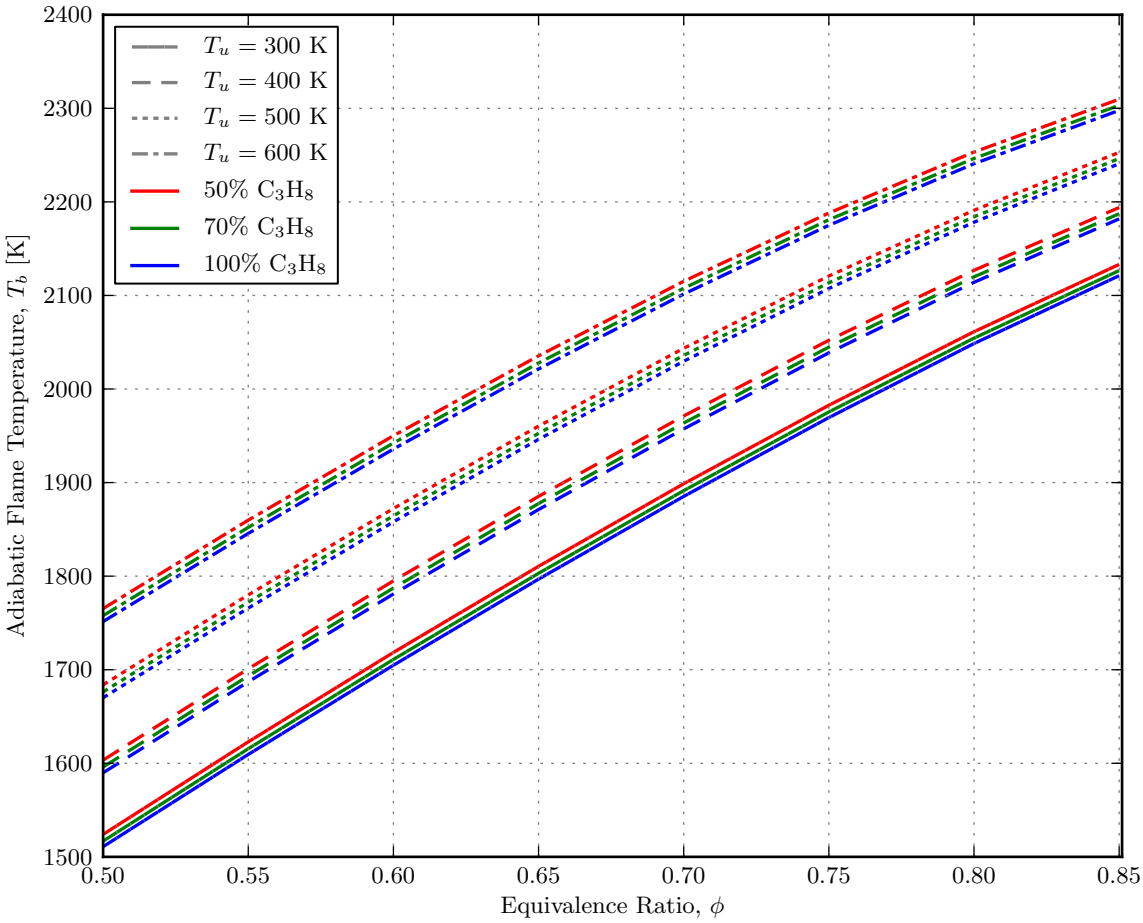

Figure 2.9: Adiabatic flame temperatures for propane–hydrogen fuel mixtures.

impact of hydrogen addition is nearly the same across the range of equivalence ratios examined. The impact of hydrogen addition on the consumption speed of strained flames increases as the equivalence ratio decreases.

2.4 Summary

The laminar strained flame model provides a controlled environment for exploring the impact of flow conditions on flame propagation. Based on simulations of hydrogen-rich flames over a range of equivalence ratios, fuel compositions, inlet temperatures and strain rates, we can identify a number of trends which influence the combustion

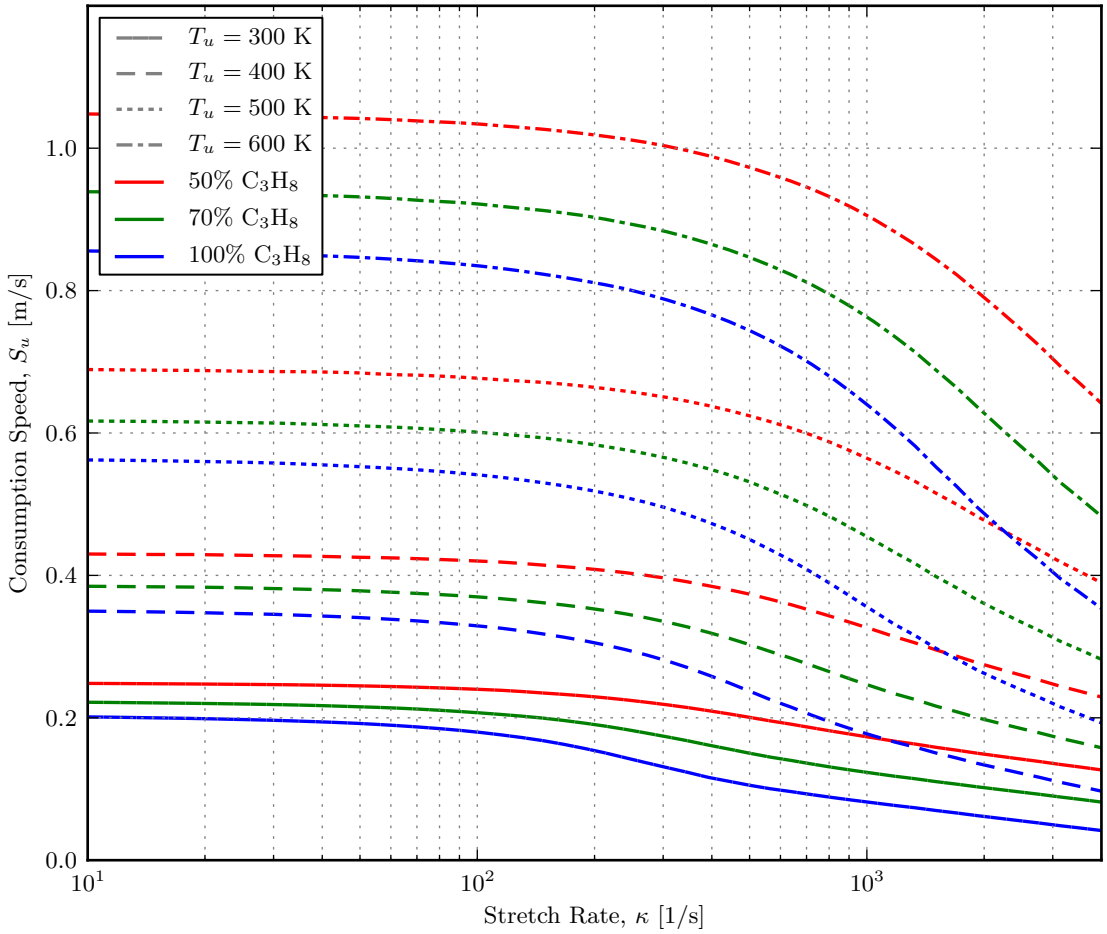

Figure 2.10: Effect of stretch on consumption speed of propane–hydrogen flames at $\phi = 0.70$.

dynamics of the two combustors that are described in the subsequent chapters. Because of the high diffusivity of hydrogen, hydrogen rich flames respond strongly to stretch. For sufficiently high hydrogen concentrations, the flame speed increases with stretch rate, while for lower hydrogen concentrations, the presence of hydrogen mitigates the decrease of flame speed that would otherwise be observed. The influence of hydrogen is greatest in flames near the lean flammability limit. Taken together, these effects introduce a strong degree of coupling between the flame and the flow environment where it is being stabilized.

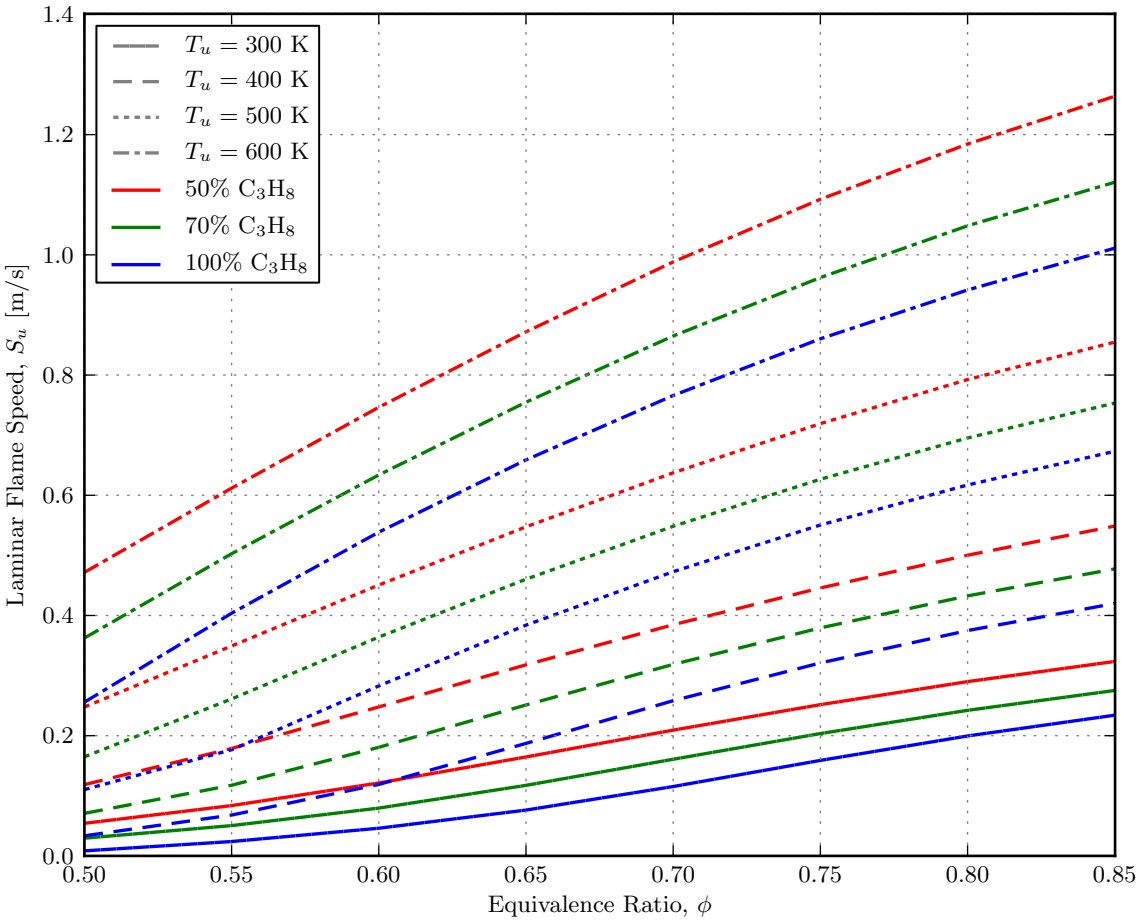

Figure 2.11: Consumption speeds for propane–hydrogen flames at $\kappa = 400\,\mathrm{s}^{-1}$.

Chapter 3

Swirl Combustor

In this chapter, we will explore the combustion dynamics observed in a laboratory scale, atmospheric pressure, lean premixed, axisymmetric swirl-stabilized combustor. Fuels composed of carbon monoxide and hydrogen at varying concentrations were tested over a range of equivalence ratios and at various inlet temperatures. Dynamic pressure and chemiluminescence measurements were taken for each case. High-speed video and stereographic particle imaging velocimetry were used to explore the dynamic interactions between the flame and the flow field of the combustor.

A sequence of stable and unstable operating modes are identified in the combustor, with each mode characterized by a distinct dynamic flame shape and acoustic response which depends on the composition of the reactants and the inlet temperature. The unstable modes are associated with acoustically driven flame–vortex interactions in the inner recirculation zone of the combustor.

A linear model of the combustor's acoustics shows that the onset of combustion instability at a particular frequency can be related to a time delay between the velocity and the exothermic response of the flame that is inversely proportional to the local burning velocity. Analysis shows that the combustor response curves across a range of operating conditions can be collapsed onto a single curve by introducing

an appropriate similarity parameter that captures the flame response to the vortex. This similarity parameter is a function of the strained flame consumption speed at a strain rate defined by the local flow conditions and the density ratio across the flame. The discovery of such a similarity transformation which captures the progression of the combustor operating modes across variations in several inlet parameters confirms the role of turbulent combustion dynamics in driving thermoacoustic instabilities.

3.1 Experimental Setup

The swirl-stabilized combustor is shown schematically in Figure 3.1. Premixed fuel and air enter the combustor test section through a choke plate. The combustor section upstream of the flame consists of a cylindrical stainless steel inlet pipe of 38 mm diameter. An axial swirler with eight hydrocoptic marzelvanes creates a swirling flow with an estimated swirl number of 0.7. 10 cm downstream of the swirler (54 cm downstream of the choke plate), the flow expands suddenly into a 76 mm diameter, 40 cm long quartz tube where the flame is anchored. At the exit of the quartz tube, the flow enters a stainless steel pipe of the same diameter, followed 50 cm further downstream by a corrugated stainless steel exhaust duct which directs the flow into the laboratory exhaust trench. The cross-sectional area of the exhaust trench is in excess of 1 m^2. The overall length of the combustor, from the choke plate to the end of the exhaust, is 4.4 m.

The main air flow is supplied by an Atlas Copco GA 30 FF air compressor capable of delivering up to 110 g/s air at 883 kPa. The air flow rate is measured using a Sierra Instruments 780S Flat-Trak flow meter. Fuel is supplied by a pair of Sierra Instruments C100M Smart-Trak digital mass flow controllers capable of delivering arbitrary hydrogen–carbon monoxide or hydrogen–propane mixtures with flow rates up to 0.3 g/s for hydrogen, 4.2 g/s for CO, and 2.3 g/s for C_3H_8. The uncertainty

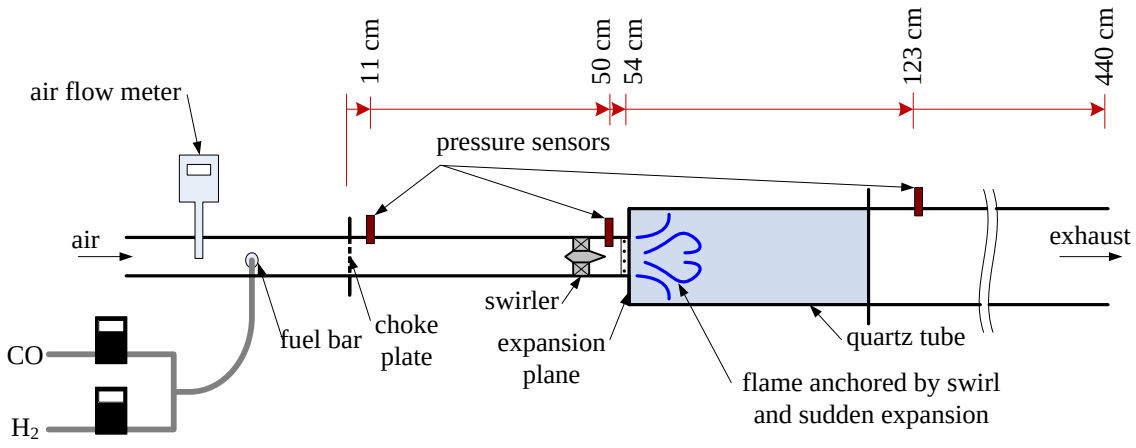

Figure 3.1: Schematic of the swirl-stabilized combustor.

in the flow rates is ±1% of full scale. The fuel and air are mixed upstream of the choke plate to eliminate acoustically-driven equivalence ratio oscillations. The air is preheated to temperatures up to 600 K using an Osram Sylvania 18 kW inline resistive electric heater. The temperature of the inlet mixture is measured using a type K thermocouple mounted 18 cm upstream of the sudden expansion, and regulated using an adaptive neural network with an optical sensor system and digital outputs.

Pressure measurements are taken 11 cm and 123 cm downstream of the choke plate using Kulite MIC-093 high-intensity microphones mounted in semi-infinite line configurations [15]. Pressure measurements 54 cm downstream of the choke plate are taken using a flush-mounted, water-cooled Kistler 7061B pressure sensor.

High-speed, spatially resolved chemiluminescence measurements of the flame at speeds up to 2000 Hz are taken using a NAC GX-1 high-speed CMOS camera with a Nikon 50 mm $f/1.8$ lens. The camera has a resolution of 1280×1024 pixels and a monochrome bit depth of 12 bits per pixel. Spatially-integrated chemiluminescence measurements are taken using a Hamamatsu H930602 photomultiplier tube (PMT).

Analog signals, including those from the pressure sensors, main air flow meter, and PMT, are sampled using a National Instruments PCIe-6259 data acquisition card. A custom Matlab code controls the experiment and manages data collection from the

various instruments. The Matlab Data Acquisition Toolbox is used to interface with the data acquisition card. The majority of the data post-processing is done in Python using a number of open source libraries for scientific computing, including NumPy [4, 41], a library providing high-performance multi-dimensional arrays and core linear algebra functionality; SciPy [26], a library which provides optimization and equation solving capabilities; Matplotlib [24], a plotting library which was used to generate most of the figures in this thesis; PIL [34], the Python imaging library, is used to read and process the chemiluminescence images; h5py [9], an interface to the HDF5 data format which is used to store the processed data; and IPython [42], an enhanced interactive Python shell.

Measurements of the velocity field are taken using a high-speed stereographic particle imaging velocimetry (PIV) system. Two high-speed NAC GX-1 CMOS cameras are mounted above the combustor, recording images at 1 to 2 kHz. A 50 W Nd:YLF laser operating in twin-pulse mode creates a light sheet less than 1 mm thick across the diameter of the combustor. The cameras are focused on the region extending downstream from the expansion plane. Bypass air, taken from the inlet pipe immediately downstream of the choke plate, is routed through a cyclone-type seeder. Seeding particles consisting of 0.9 to 2.2 μm Al_2O_3 particles are introduced into the main air flow upstream of the swirler. The PIV measurements are processed using the LaVision DaVis 7.2 software.

3.2 Operating Modes

To determine the stability map of the swirl-stabilized combustor, we conducted a series of experiments where the inlet conditions were varied while dynamic pressure and chemiluminescence measurements were recorded. We varied the syngas composition from 20% CO and 80% hydrogen to 80% CO and 20% hydrogen by volume, in

Table 3.1: Operating modes of the swirl-stabilized combustor.

Mode	Frequency	OASPL
I	–	< 135 dB
IIa	10–40 Hz	145–155 dB
IIb	30–40 Hz	> 160 dB
IIc	–	140–145 dB
IIIa	100–120 Hz	> 165 dB
IIIb	160–180 Hz	> 165 dB
IIIc	230–250 Hz	> 165 dB

increments of 20%, and varied the inlet temperature from 300 K to 500 K in increments of 100 K. For each syngas composition and temperature, we varied the equivalence ratio of the fuel-air mixture from near the lean blowoff limit up to a value approaching the flashback limit.

The Reynolds number, based on the combustor inlet diameter of 38 mm, was held constant at 25,000 for all tests. This corresponds to a mean inlet velocity of 11.3 m/s at 300 K, which increases to 18.1 m/s at 400 K and 26.8 m/s at 500 K. The inlet velocity varies by less than $\pm 5\%$ as a function of fuel composition and equivalence ratio.

As the input parameters vary, we can identify several distinct operating modes of the combustor, characterized by the amplitude and frequency of pressure oscillations in the combustor and by the dynamic flame anchoring configuration. The frequencies and overall sound pressure levels (OASPL) in each operating mode of the swirl-stabilized combustor are shown in Table 3.1. The major mode, indicated by the Roman numeral, represents a particular dynamic flame shape. The characteristics of each dynamic flame shape are discussed in detail in Section 3.3. The minor mode, indicated by a lowercase letter, is used to differentiate flames with similar shapes but distinct acoustic responses. At a fixed inlet temperature and fuel composition, gradually increasing the equivalence ratio causes the combustor to transition from one

mode to the next in the order shown, but not all modes are present for all combinations of fuel composition and inlet temperature.

Mode I consists of a long, tubular flame anchored by the inner recirculation zone. There is no flame in the outer recirculation zone. Flames in this mode are always stable. Mode II consists of a primary flame anchored by the inner recirculation zone, with a secondary flame anchored in the outer recirculation zone. In Modes IIa and IIb, the flame in the outer recirculation zone is periodically extinguished and re-ignited, and there are concomitant oscillations in the intensity of the primary flame. In Mode IIc, there are no oscillations; the flame anchored in the outer recirculation zone is weak, but steady. Mode III consists of a flame which is wrapped around a strongly-oscillating annular jet. The flame shape remains essentially the same even as the frequency of the oscillation shifts.

3.2.1 Pressure Measurements

In this section, we examine the conditions under which the modes defined in the previous section are observed. We begin by considering a series of measurements taken at a fixed fuel composition and inlet temperature where the equivalence ratio was gradually reduced during a single run of the combustor from a relatively high value, where much of the flame was upstream of the sudden expansion, down to the lean blowoff limit. The overall sound pressure level and the frequency of the highest-amplitude pressure oscillation are shown in Figure 3.2 as a function of equivalence ratio for a 40:60 CO:H_2 fuel mixture at $T_u = 300$ K. The pressure measurements shown are taken from the pressure sensor located closest to the choke plate, where the pressure oscillation amplitudes are at their highest. Starting at high equivalence ratios, the flame is unstable in Mode IIIb, with an OASPL of 172 dB and a frequency of 176 Hz. As the equivalence ratio decreases below $\phi = 0.35$, the OASPL decreases to 165 dB and the frequency decreases to 110 Hz as the combustor transitions to Mode

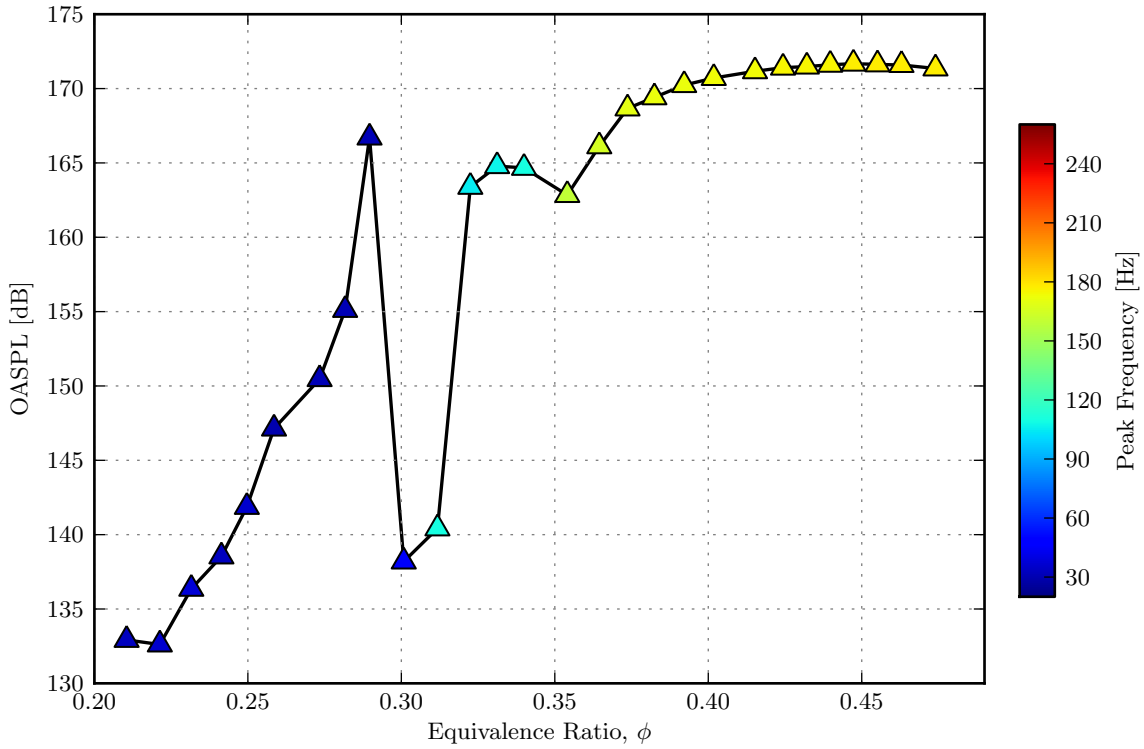

Figure 3.2: Overall sound pressure level and peak frequency as a function of equivalence ratio for a 40:60 CO:H_2 fuel mixture at $T_u = 300$ K.

IIIa. As the equivalence ratio decreases below $\phi = 0.32$, the OASPL drops sharply as the combustor transitions to Mode IIc. The transition to Mode IIb follows shortly thereafter at $\phi = 0.29$, marked by the return of high-amplitude pressure oscillations with an OASPL of 167 dB at a frequency of 32 Hz. Decreasing the equivalence ratio to $\phi = 0.25$ decreases the amplitude and coherence of the pressure oscillations at this frequency, corresponding to Mode IIa. In the region corresponding to Mode I, below $\phi = 0.25$, the pressure oscillations are negligible. The flame blows off below $\phi = 0.21$.

The same general sequence of mode transitions is also observed if the equivalence ratio is increased from the lean blowoff limit. However, the equivalence ratio at which each transition occurs varies, with the transitions generally occurring at higher equivalence ratios when $d\phi/dt$ is positive and lower equivalence ratios when $d\phi/dt$ is negative. The combustor operating mode exhibits hysteresis with respect to changes

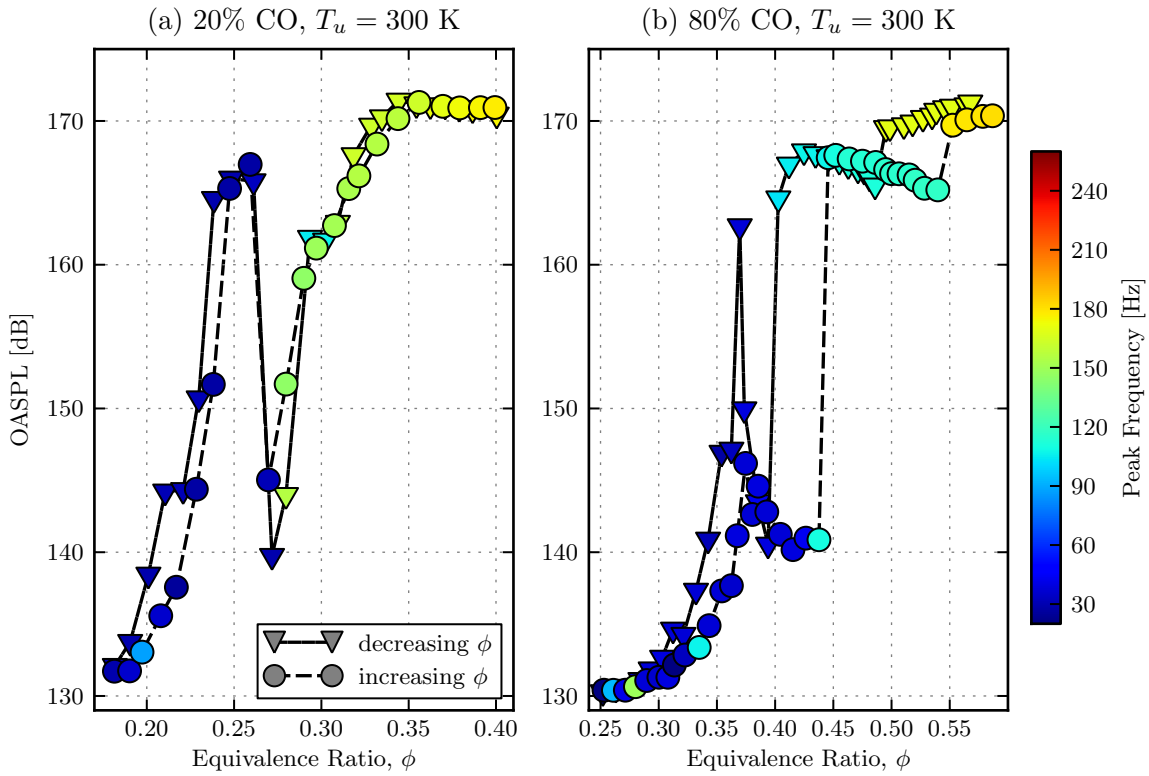

Figure 3.3: Hysteresis in the swirl-stabilized combustor with respect to changes in equivalence ratio for two different fuel compositions.

in the equivalence ratio. In Figure 3.3(a), the OASPL is plotted as a function of equivalence ratio for the cases of increasing and decreasing equivalence ratio for a fuel mixture consisting of 20% CO and 80% H_2 at an inlet temperature of 300 K. Figure 3.3(b) shows the corresponding data for a fuel mixture consisting of 80% CO and 20% H_2 at the same inlet temperature. For the 20% CO fuel mixture, there is no discernible hysteresis effect. However, in the case of the 80% CO mixture, the transitions between Modes IIc and IIIa and between Mode IIIa and IIIb both display strong hysteresis effects, with the equivalence ratio for each transition shifting by approximately $\Delta\phi = 0.05$. The hysteresis effect diminishes at elevated inlet temperatures. Hysteresis appears to be negligible for Mode IIb at all inlet conditions.

Huang and Yang [23] previously identified hysteresis in numerical simulations of a swirl-stabilized combustor where the the transition to instability was accompanied by

a transition in the flame anchoring configuration. They attributed the hysteresis to local heating of the combustor wall in the unstable mode which tends to inhibit the local extinction which would be required to return the flame to the stable configuration. Since the high-CO flames—which are more susceptible to extinction by heat loss—are the ones for which we observe the strongest hysteresis effects, it is plausible that the hysteresis effects in this combustor are also a result of heat transfer interactions in the combustor.

To control for the effects of hysteresis, the results shown from this point forward will be for decreasing equivalence ratio. This represents a pessimal view of the combustor's stability, with measurements reflecting the highest-frequency unstable mode present at a particular combination of fuel composition, inlet temperature, and equivalence ratio.

We now consider the effects of fuel composition and inlet temperature on the combustor's pressure response. The OASPL for equivalence ratio sweeps of fuel mixtures with CO:H_2 ratios of 20:80, 40:60, 60:40, and 80:20 at an inlet temperature of $T_u = 300$ K are shown in Figure 3.4(a). Equivalence ratios for the same set of fuel mixtures at inlet temperatures of $T_u = 400$ K and $T_u = 500$ K are shown in Figures 3.4(b) and 3.4(c), respectively. The dependence of the OASPL on the equivalence ratio is approximately the same for all fuel compositions and inlet temperatures, but the entire response is shifted to higher equivalence ratios as the CO:H_2 ratio increases, and shifted to lower equivalence ratios as the inlet temperature increases. At elevated inlet temperatures and high equivalence ratios, the high-frequency Mode IIIc is observed.

Changes in fuel composition and inlet temperature alter the range of equivalence ratios for which some dynamic modes are observed. The range of equivalence ratios over which Mode IIIa is observed increases with the CO:H_2 ratio and decreases with temperature. At $T_u = 300$ K, Mode IIIa is observed over a range of equivalence

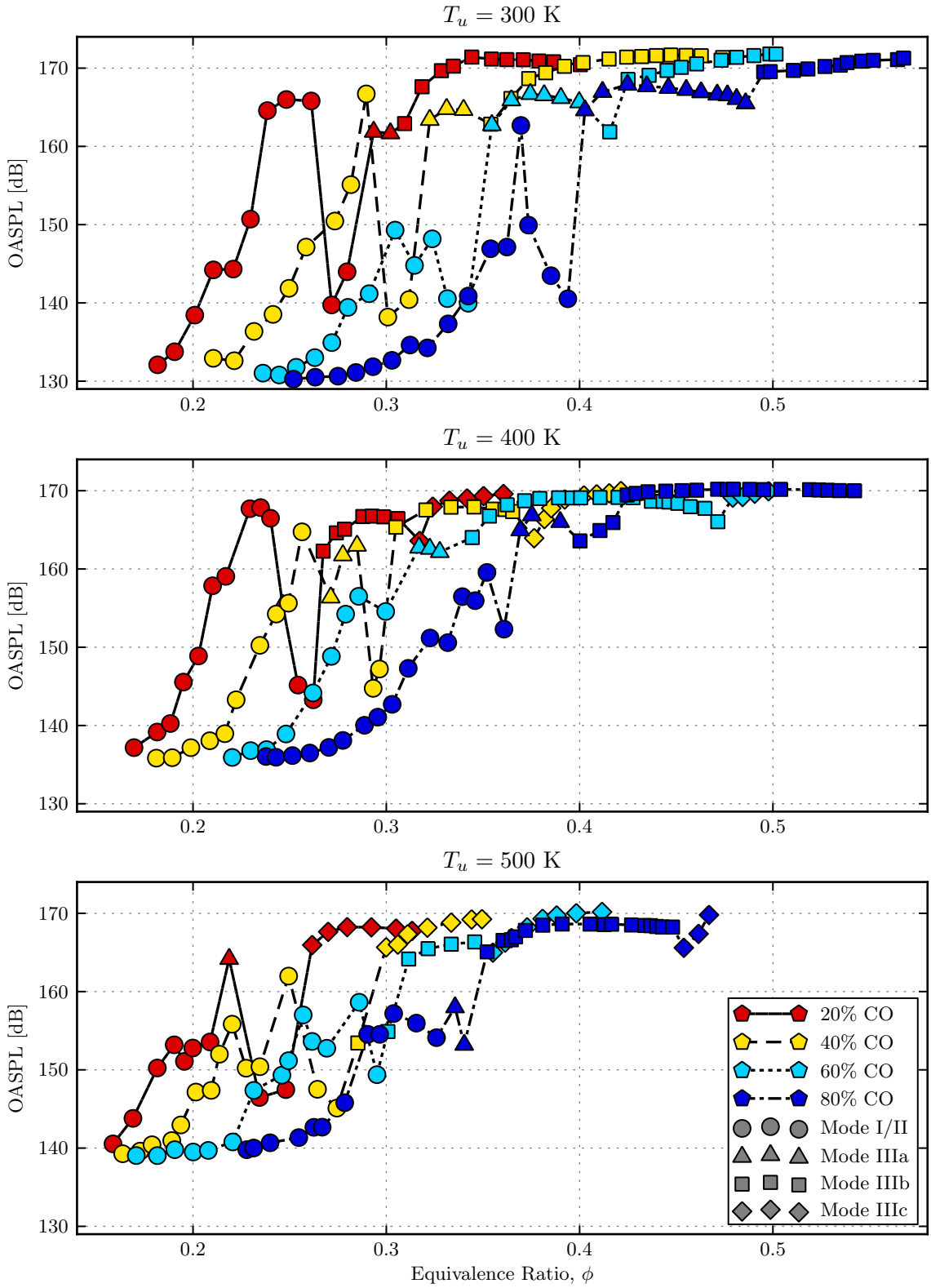

Figure 3.4: OASPL at the choke plate for syngas flames in the swirl-stabilized combustor with different fuel compositions and inlet temperatures as a function of equivalence ratios.

ratios $\Delta\phi = 0.09$ for the 80:20 CO:H_2 fuel mixture, decreasing to $\Delta\phi = 0.02$ for the 20:80 CO:H_2 fuel mixture. As the inlet temperature increases, Mode IIIa is almost entirely occluded by the surrounding modes. A similar trend occurs where Mode IIIc begins to occlude Mode IIIb as well. Thus, the number of sub-modes characterizing the combustor's pressure response in Mode III decreases as the inlet temperature and hydrogen concentration in the fuel increase.

Mode IIb is also strongly affected by changes in fuel composition and inlet temperature. It is observed over the widest range of equivalence ratios for fuel mixtures with high hydrogen content and at low inlet temperatures. Decreasing the hydrogen content in the fuel mixture or increasing the inlet temperature quickly causes Mode IIb to narrow or disappear completely. Mode IIb is highly sensitive to certain changes in the combustor's acoustic boundary conditions. Specifically, Mode IIb tends to be suppressed in favor of Mode IIa when there is a small air gap at either end of the quartz tube.

The most important phenomenon revealed by these response curves is the overarching trend for mode transitions to shift to lower equivalence ratios as the hydrogen concentration in the fuel and the inlet temperature increase. Since equivalence ratio, hydrogen concentration, and inlet temperature are all positively correlated with flame speed, this suggests that the transitions between different modes are governed by the flame speed corresponding to the reactants mixture. Building on this observation, a detailed model relating the flame speed, flame shape, and operating mode is developed in Section 3.6.

3.2.2 Heat Release Rate

In typical lean premixed flames, the visible-spectrum emissions consist of narrow band emissions from CH^* and C_2^* radicals and continuum emissions from CO_2^*. Measurements of CH^* and OH^* emissions are a well-established method for measuring

heat release rate in hydrocarbon flames [21]. However, the kinetic pathways which produce CH^* and OH^* are not active for syngas flames. Thus, the visible emissions of syngas flames consists predominantly of continuum emission from CO_2^*, produced by the following mechanism [18, 47, 49]:

$$CO + O + M \rightarrow CO_2^* + M \tag{3.1}$$

$$CO_2^* + M \rightarrow CO_2 + M \tag{3.2}$$

$$CO_2^* \rightarrow CO_2 + h\nu \tag{3.3}$$

In this mechanism, CO_2^* is formed by reaction with an atomic oxygen radical. CO_2^* is consumed by the chemiluminescent reaction 3.3 and the quenching reaction 3.2. Since CO_2^* formation occurs in a fuel consumption pathway for CO, we expect that at a constant equivalence ratio and fuel composition, the intensity of CO_2^* chemiluminescence is proportional to the local instantaneous heat release rate. Therefore, spatially-resolved visible-spectrum chemiluminescence measurements can be taken to reasonably reflect the location of the flame in the combustor. These flame images are discussed in Section 3.3. For now, we focus on integral measurements of the visible-spectrum emissions from the flame, measured with the photomultiplier tube, which give a measure of the time-varying total heat release rate.

In Figure 3.5, we show the amplitude of oscillations in the chemiluminescence intensity as measured by the photomultiplier tube, normalized by their mean value. If $I(t)$ is the chemiluminescence intensity, then the amplitude of the normalized chemiluminescence intensity oscillations can be defined as

$$I^* \equiv \frac{\text{stdev}(I(t))}{\text{mean}(I(t))} \tag{3.4}$$

The amplitude of the chemiluminescence intensity oscillations increases dramatically

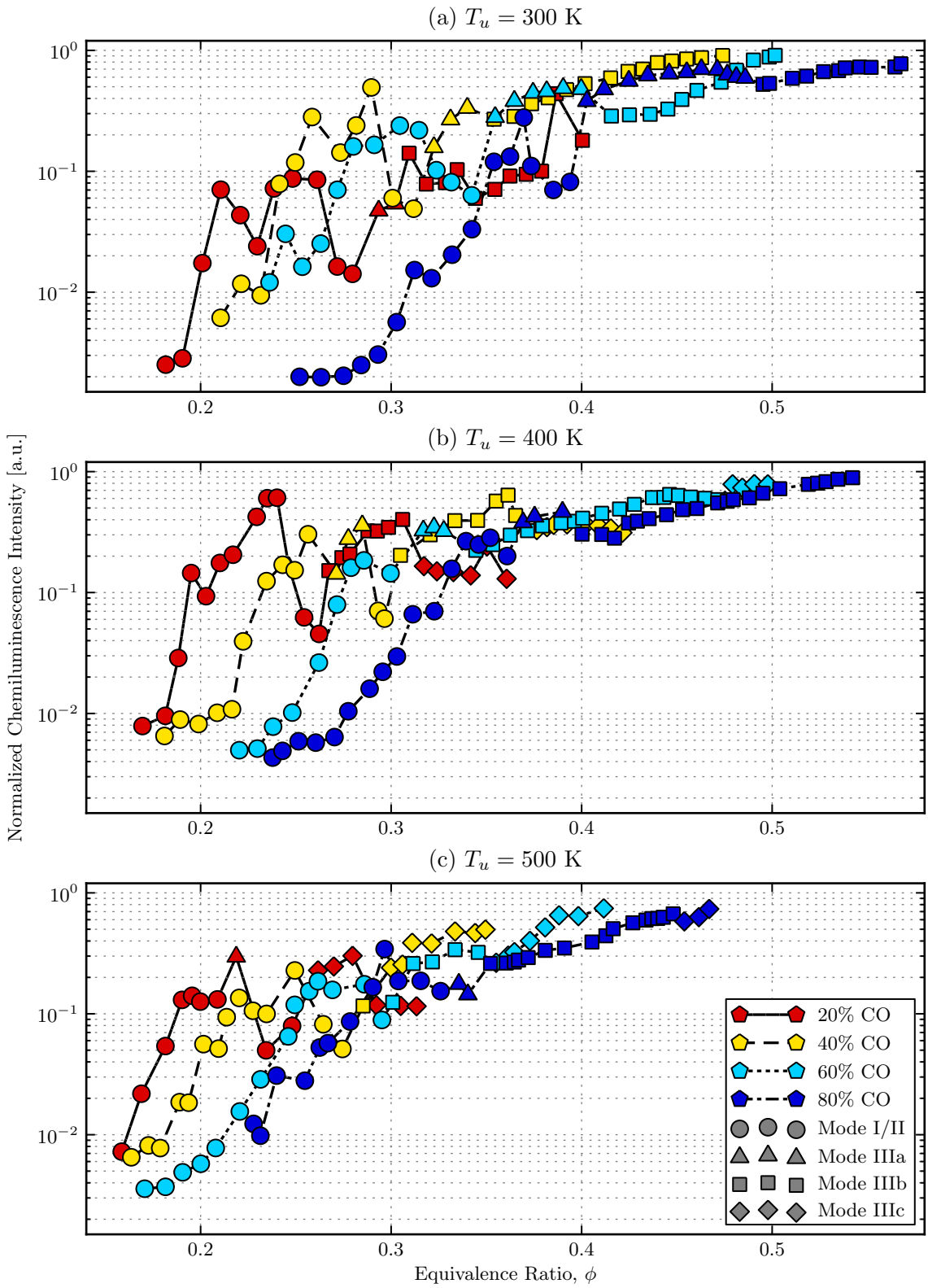

Figure 3.5: Normalized chemiluminescence intensity oscillation amplitude as a function of equivalence ratio for different syngas compositions and inlet temperatures.

as the concentration of CO in the fuel is increased, as well as increasing with the equivalence ratio, so the normalization is necessary in order to consider it an acceptable surrogate for the heat release rate.

Many of the same trends identified in the OASPL are visible here as well, although the transitions between modes are not as starkly defined. The local minimum in OASPL associated with Mode IIc is visible in I^*, but the degree of amplitude reduction compared to neighboring modes is much smaller. Likewise, the value of I^* in Mode IIa is relatively high, which indicates that this mode has substantial heat release oscillations despite the relatively low pressure oscillations. In Mode III, I^* generally increases with the equivalence ratio, with the amplitude of heat release rate oscillations nearly reaching the mean heat release rate. The increase in I^* in this region occurs despite the fact that the OASPL is roughly constant.

Perhaps the most interesting piece of information which can be extracted from the chemiluminescence measurements is the phase between heat release rate and pressure oscillations, θ_{qp}. From the Rayleigh criterion, we expect that θ_{qp} should be in the interval $-\pi/2 < \theta_{qp} < \pi/2$ in each of the unstable modes. The values of θ_{qp} are calculated in the following manner: Let $p(t)$ and $q(t)$ be the time-varying pressure and chemiluminescence signals, respectively. We take the Fourier transform of each to obtain $\hat{p}(\omega)$ and $\hat{q}(\omega)$. If ω_m is frequency for which $|\hat{p}\,(\omega)|$ is maximized, the phase between heat release rate and pressure at that frequency is

$$\theta_{qp} = \arg\left(\frac{\hat{q}(\omega_m)}{\hat{p}(\omega_m)}\right) \tag{3.5}$$

where $\arg(z)$ is the complex argument of z, such that $\arg\left(re^{\mathrm{i}\theta}\right) = \theta$. The values of θ_{qp} calculated as a function of equivalence ratio for several combinations of inlet temperature and fuel composition are shown in Figure 3.6. Across all inlet temperatures and fuel compositions, we observe the same fundamental behavior.

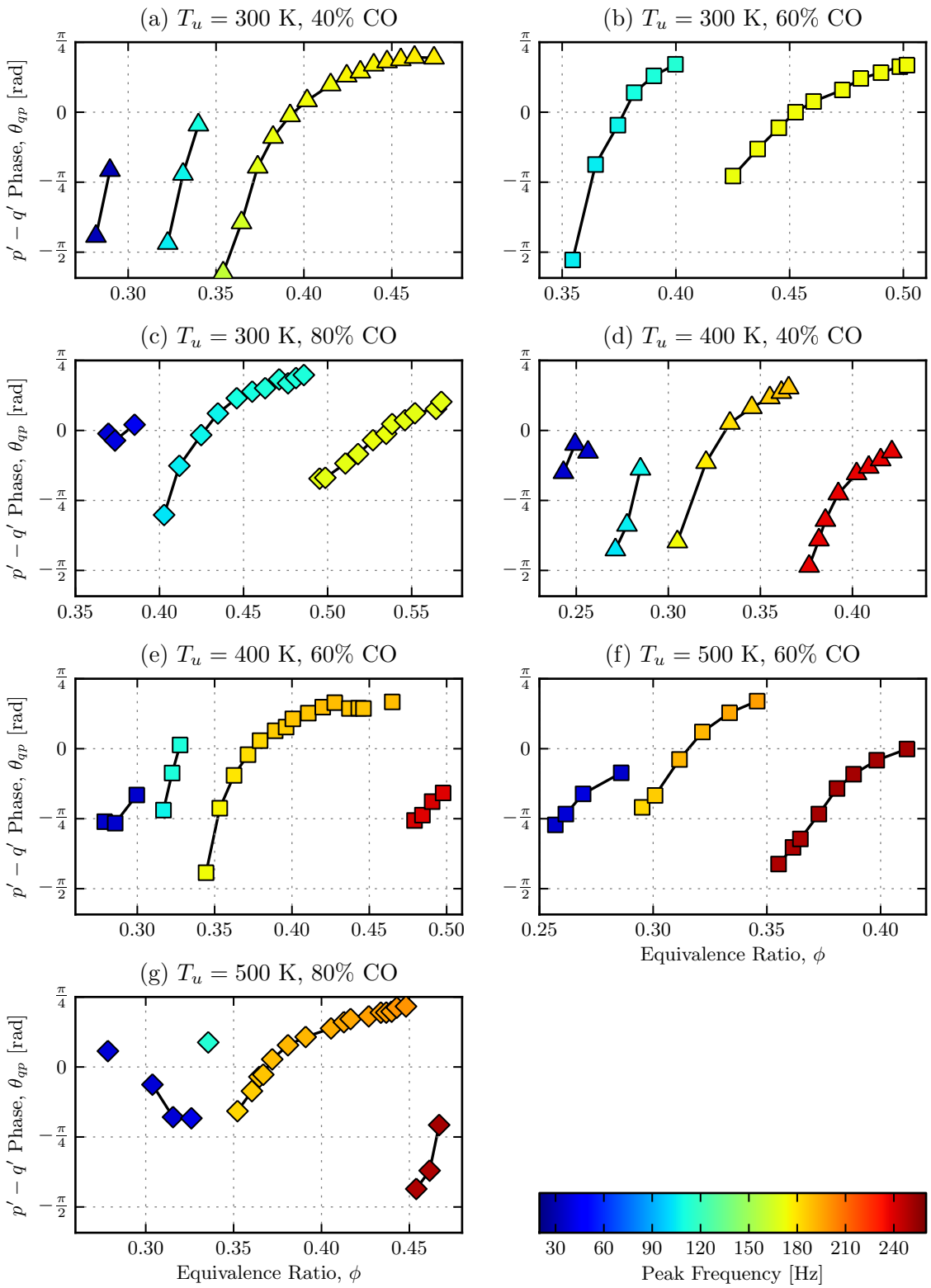

Figure 3.6: Phase between heat release rate and pressure in the swirl-stabilized combustor for selected combinations of inlet temperature and fuel composition.

Starting at the highest equivalence ratio in a particular acoustic mode, the heat release rate generally leads the pressure by an angle $\theta_{qp} \approx \pi/4$. As the equivalence ratio decreases, the heat release rate begins to lag behind the pressure, first gradually and then more rapidly as θ_{qp} approaches $-\pi/2$. When θ_{qp} decreases below $-\pi/2$, heat release rate and pressure oscillations in that mode are no longer unstable, and the combustor transitions to a lower-frequency acoustic mode. This process repeats until the lowest frequency mode of the combustor is reached.

Since the primary effect of decreasing the equivalence ratio while holding other inlet parameters fixed is to decrease the flame speed, the trend of θ_{qp} decreasing with equivalence ratio is consistent with the idea of the phase between heat release rate and pressure being determined by a time delay that is inversely proportional to the flame speed. Before we can explore this idea further, we need first to understand the coupling mechanism between heat release rate and pressure oscillations, and to develop a model which describes the acoustic modes observed in the combustor. We will return to the analysis of the data in Section 3.5.2.

3.3 Flame Chemiluminescence

In this section, we will examine the dynamic flame shapes of syngas flames in the swirl-stabilized combustor in the previously-defined combustor operating modes, with the goal of understanding how the interactions between the flame and the velocity field in the flame-anchoring region give rise to the heat release dynamics which characterize each mode.

Close to the lean blowoff limit, we observe stable flames anchored within the inner recirculation zone downstream of the expansion plane, corresponding to Mode I as defined in Section 3.2. Figure 3.7 shows a sequence of chemiluminescence images recorded for a flame with a 80:20 CO:H_2 ratio at $\phi = 0.34$ and $T_u = 300$ K. Images

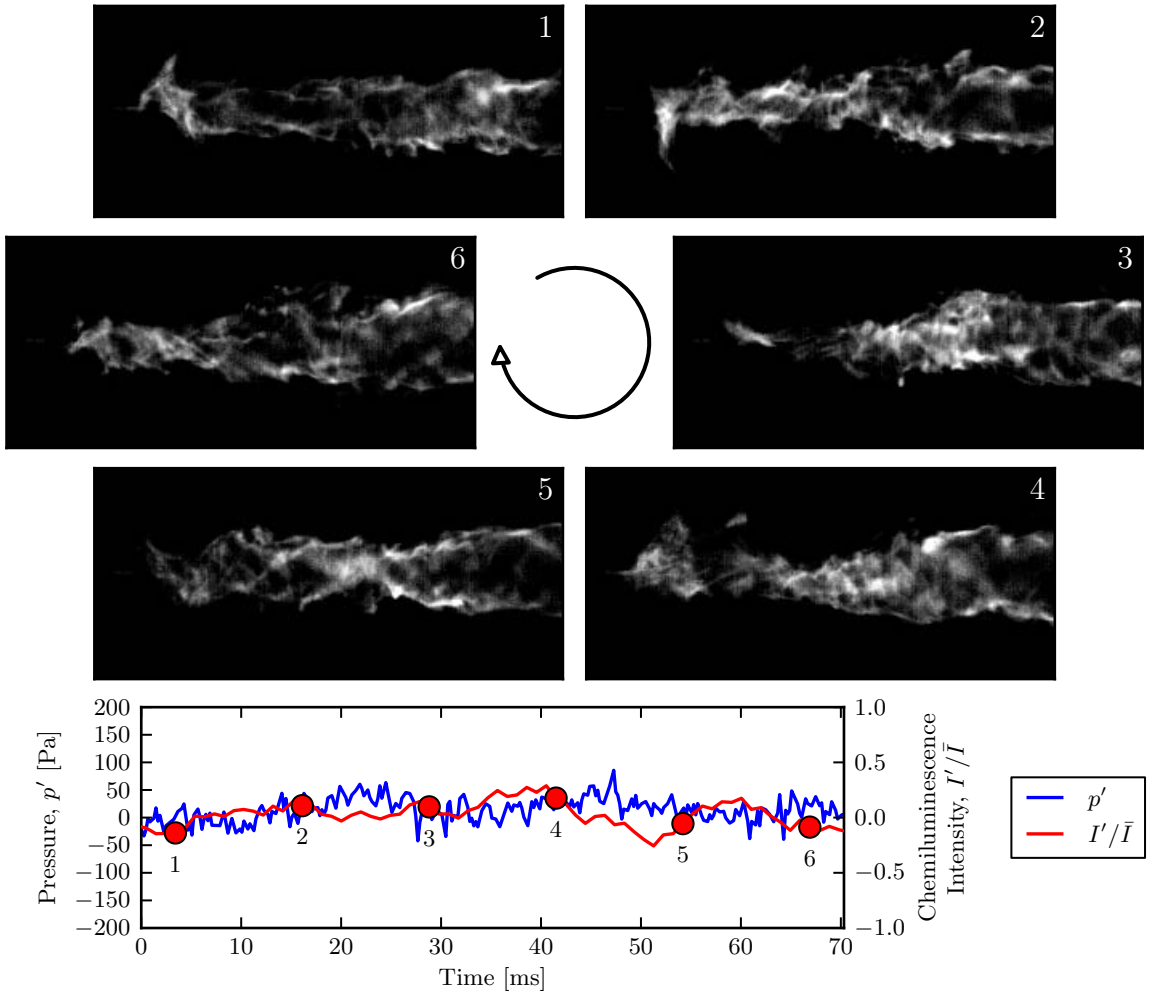

Figure 3.7: Flame chemiluminescence images characteristic of Mode I.

are recorded with an exposure time of 1.0 ms, and are shown at 13.0 ms intervals. Reactants flow along the outer wall of the combustor, and products flow along the centerline of the combustor, with the flame propagating radially outward. The flame extends downstream well beyond the 40 cm long quartz observation section of the combustor, in accordance with the very large flame surface required to consume the mixture. The laminar flame speed for this mixture is 4.6 cm/s, which would require a flame surface area of 0.263 m^2, or 230 times the cross-sectional area of the inlet channel. While the images show that flame surface is impacted by the underlying weak turbulent flow, they also show local dark spots, indicating possible extinction in

many places along the surface, further contributing to the unusually large surface [31]. The flame surface is weakly unsteady at the large scale, and there is evidence of helical modes that propagate downstream. The leading edge of the flame is anchored in the inner recirculation zone, downstream of the sudden expansion. The axial location of the anchoring point fluctuates in time, usually remaining 2–5 cm downstream of the expansion plane. The anchoring point moves downstream as the equivalence ratio is decreased. Similar flame shapes under very lean conditions have been observed by Fritsche et al. [16]. While there are non-negligible heat release rate oscillations associated with this flame structure, pressure oscillations (also shown in Figure 3.7) are weak, and there is no coherent coupling between the two.

As the equivalence ratio increases, there is a distinct change in the overall flame shape associated with the leading edge of the flame anchoring on the swirler centerbody upstream of the sudden expansion. A sequence of images for a typical flame of this type, Mode IIa, is shown in Figure 3.8 for a fuel mixture with a 60:40 CO:H_2 ratio at $\phi = 0.37$ and $T_u = 400$ K. Flame images are shown every 6.5 ms, with an exposure time for each image of 0.5 ms. This flame is substantially more compact than the one observed in Mode I. At these inlet conditions, the laminar flame speed for this flame of $S_u = 16.9$ cm/s corresponds to a total flame area of 0.121 m^2, or 107 times the cross-sectional area of the inlet channel. This flame exhibits a low frequency, low amplitude oscillation with a frequency of ˜25 Hz. Visually, this mode is characterized by periodic pulsations in the flame's chemiluminescent intensity. A flame anchored by the outer recirculation zone is established and extinguished in concert with the overall intensity oscillations. The brightness of the expanding flame reaches a maximum near the pressure peak of the cycle, indicating synchronization between the heat release rate and the pressure oscillations. The flame anchoring zone exhibits signs of periodic vortex shedding at the sudden expansion section. The shedding is mostly confined within the inner recirculation zone. It is clear from the

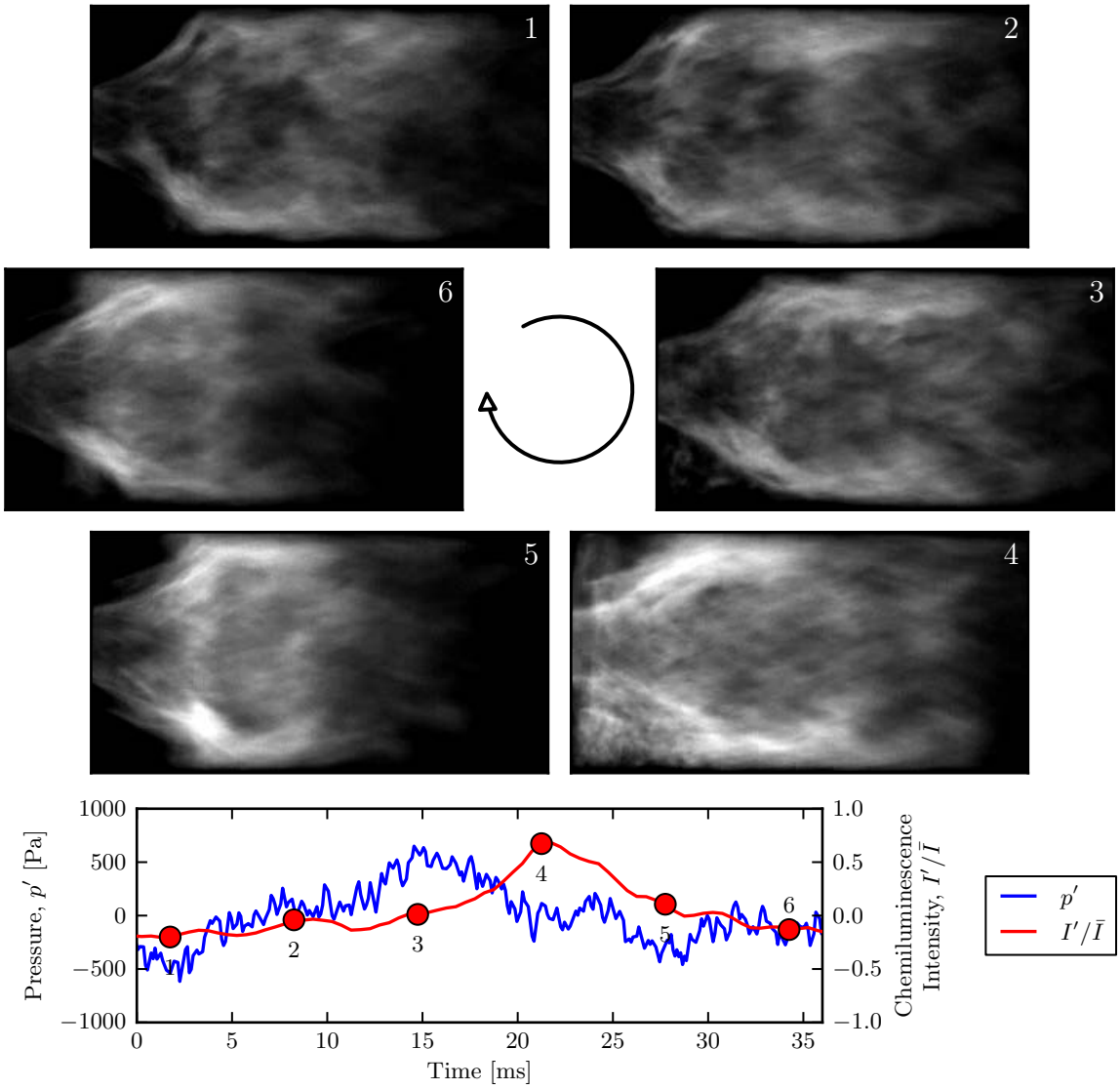

Figure 3.8: Flame chemiluminescence images for a typical cycle in Mode IIa.

flame structure that the vortex shedding in this case is essentially symmetric. Low frequency oscillation in the wake zone of the sudden expansion in a swirling flow have been observed in numerous experiments and numerical simulations [45, 46].

At slightly higher equivalence ratios than those for which Mode IIa is observed, we sometimes see a mode with a very similar flame structure, but with much stronger coupling between the flame and the acoustic field. A sequence of images for a typical flame of this type, Mode IIb, is shown in Figure 3.9 for a fuel mixture with a 20:80 $CO:H_2$ ratio at $\phi = 0.26$ and $T_u = 300$ K. Overall, the flame structure

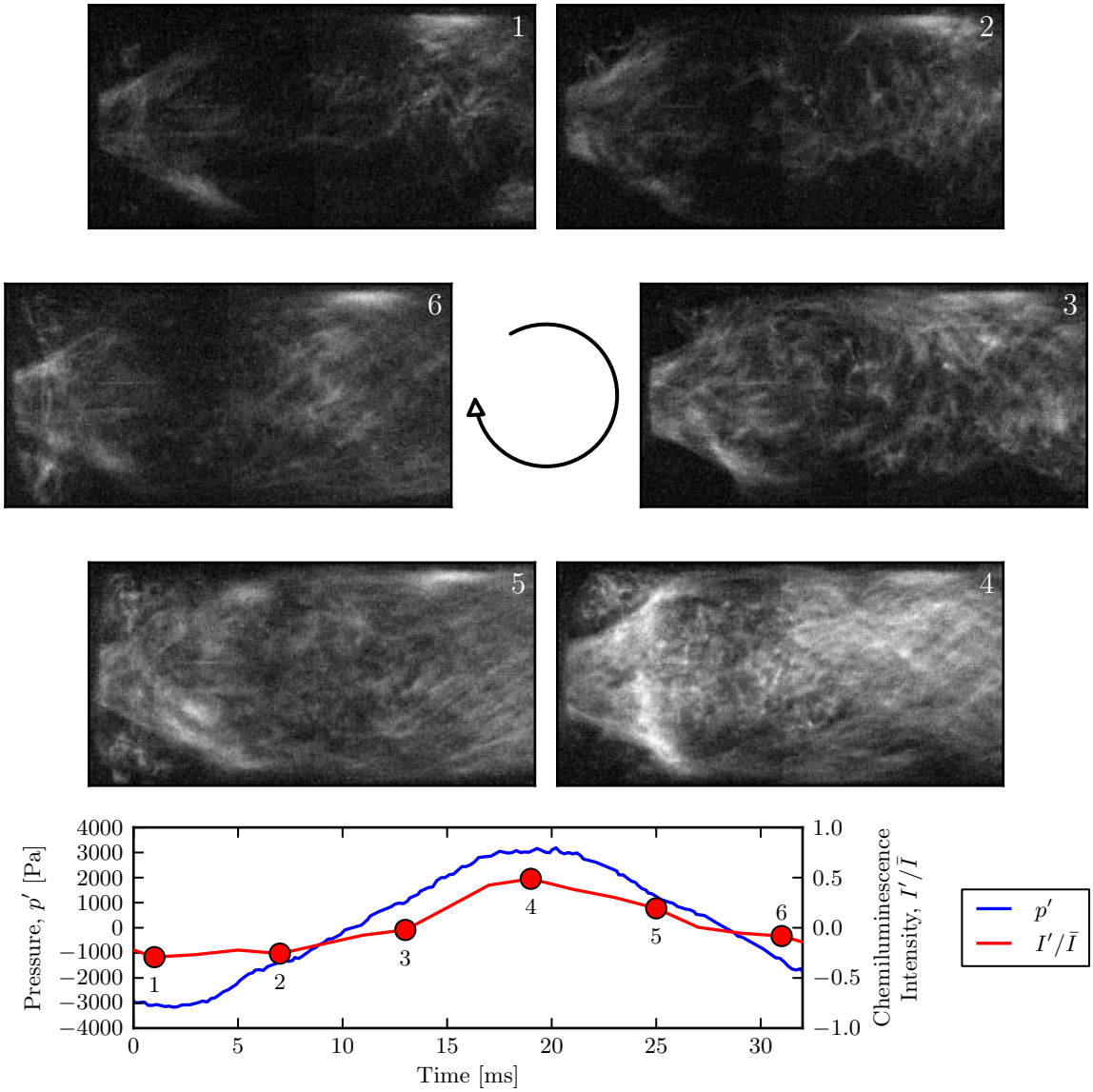

Figure 3.9: Flame chemiluminescence images for a typical cycle in Mode IIb.

in this mode is quite similar to that observed in Mode IIa. The flame expands outward downstream of the sudden expansion, with a region of particularly high chemiluminescence intensity near the location where the flame reaches the outer wall of the combustor. Downstream of this point, the flame front breaks up into many small-scale structures. In this mode, the periodic oscillations in the flame's intensity appear to occur simultaneously throughout the entire burning zone. Compared to Mode IIa, the amplitude of the flame intensity oscillation in this mode is comparable,

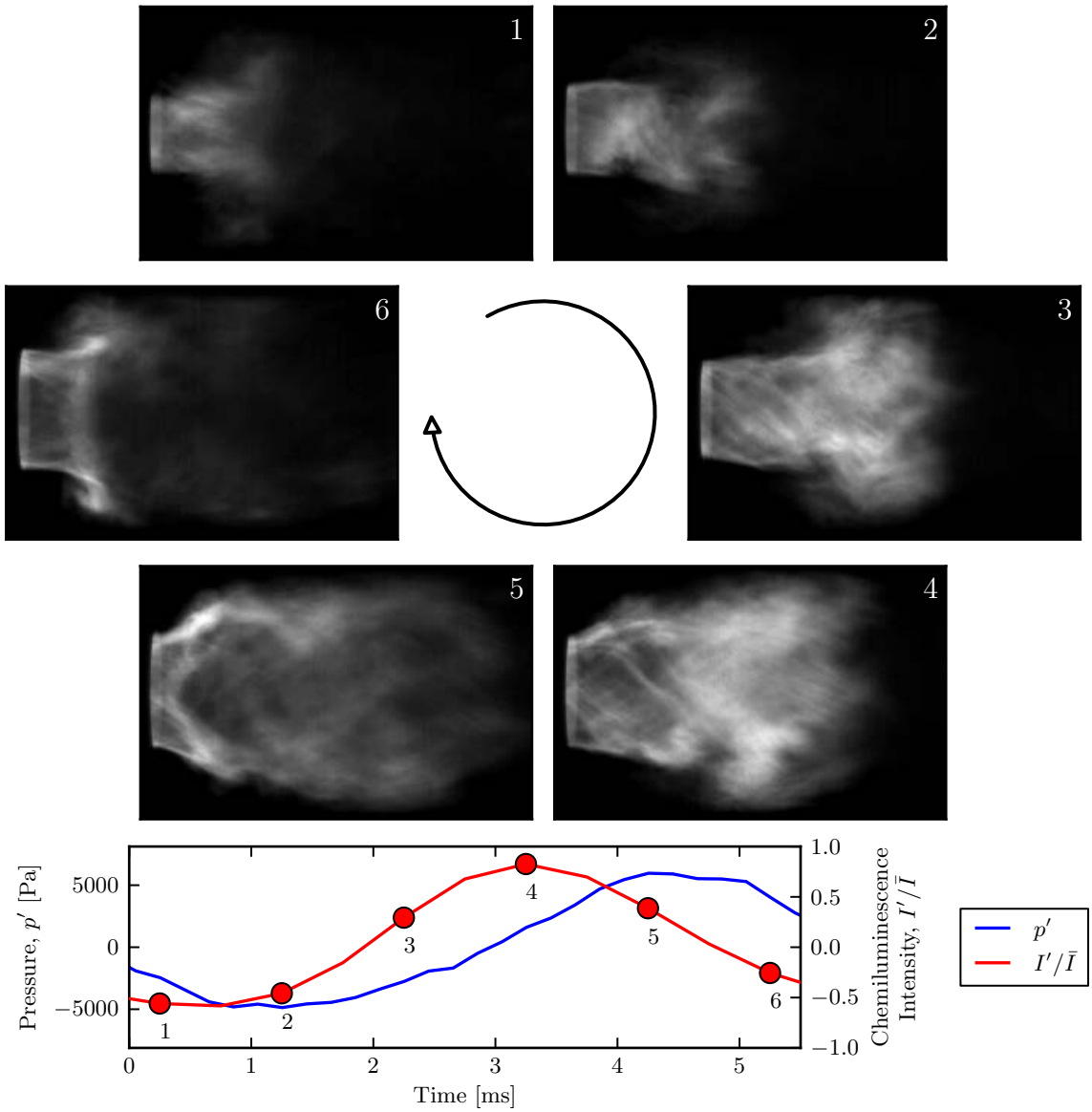

Figure 3.10: Flame chemiluminescence images for a typical cycle in Mode IIIb.

but the amplitude of the pressure oscillation is higher by nearly an order of magnitude.

At high equivalence ratios, the flame structure begins to oscillate strongly at a frequency coupled with the acoustic field of the combustor. This operating mode is designated as Mode III. Figure 3.10 shows a sequence of images for a typical flame in Mode IIIb, for a flame with a 60:40 CO:H_2 ratio at $\phi = 0.44$ and $T_u = 300$ K. Images with an exposure time of 0.5 ms are shown at intervals of 1.0 ms. The frequency of flame and acoustic oscillations is 167 Hz. Compared to the flame shapes observed in

Mode I and Mode II, this flame is much more compact, extending at most four inlet diameters downstream of the expansion plane. At these inlet conditions, the laminar flame speed is $S_u = 15.0$ cm/s, which would require a total flame surface area of 0.084 m^2, or 74 times the cross-sectional area of the combustor inlet. Clearly, there must be substantial small-scale wrinkling of the flame structure to produce this much surface area in such a compact flame. The strong unsteady vortex shedding in the inner recirculation zone formed by the swirling flow results in a strongly oscillating flame interacting with the vortex. In each cycle, a vortex is shed from the recirculation zone and then convected downstream. As the vortex grows and travels downstream, the flame grows axially while seeming to be convoluted around the vortex, producing a mushroom-shaped structure. The vortex collapses, leading to a brief period of intense burning. The cycle repeats as the next vortex is shed. The pressure trace and the corresponding images show that the brightest images, corresponding to the maximum burn rate, immediately precede the pressure peak.

At sufficiently high equivalence ratios, for certain combinations of inlet temperature and fuel composition, we observe an increase in the frequency of flame oscillations, corresponding to the transition to Mode IIIc. Figure 3.11 shows a sequence of images for a typical flame in Mode IIIc, with a 60:40 CO:H_2 ratio at $\phi = 0.36$ and $T_u = 500$ K. Images with an exposure time of 0.5 ms are shown at intervals of 0.5 ms. The frequency of flame and acoustic oscillations is 240 Hz. At these inlet conditions, the laminar flame speed is $S_u = 30.2$ cm/s, which would require a total flame surface area of 0.099 m^2, or 87 times the cross-sectional area of the combustor inlet. Despite the change in operating conditions and the change in the frequency of acoustic oscillations, this flame structure is quite similar to that observed in Mode IIIb. The large increase in flame speed compared to the flame shown in Figure 3.9 is mostly offset by the increase in the mean flow velocity at elevated inlet temperatures.

In this section, we have seen that the operating modes of the swirl combustor

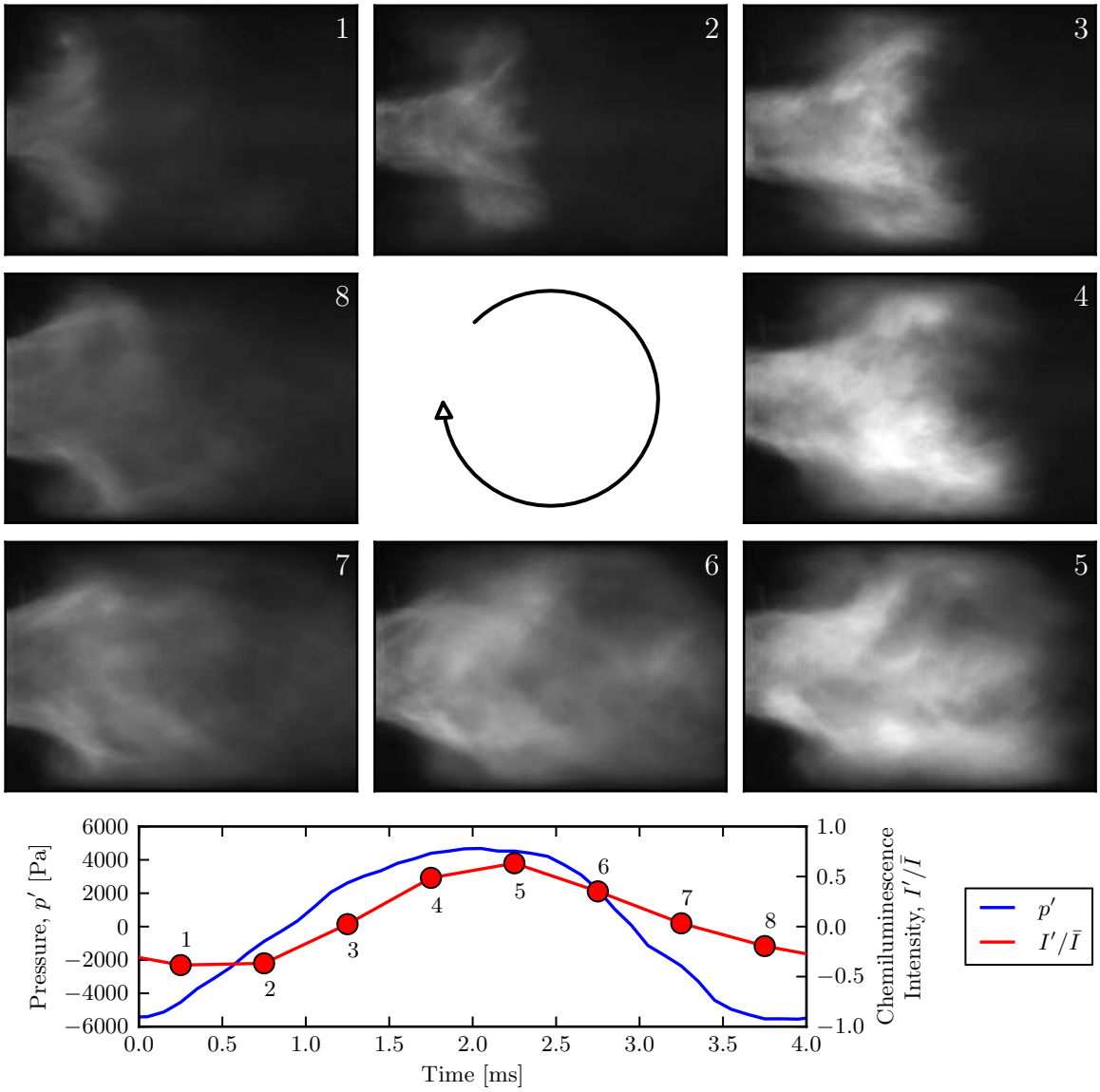

Figure 3.11: Flame chemiluminescence images for a typical cycle in Mode IIIc.

are associated with the dynamic flame shape. The flame shape is determined by the interaction between the flame speed and the velocity field in the flame anchoring region. For very lean mixtures with low flame speeds and large flame areas, the flame extends far downstream of the sudden expansion, and its propagation is uncoupled from the vortex dynamics at the expansion plane. At intermediate equivalence ratios, the local burning rate begins to oscillate in conjunction with the acoustically-coupled velocity field, but the overall flame shape remains relatively static. At high equivalence

ratios, compact flames anchored close to the sudden expansion are strongly coupled with acoustically-driven vortex shedding. In the next section, we will explore the coupling between the flame and the flow which characterizes the unstable operating modes.

3.4 Particle Imaging Velocimetry

In order to understand the interactions between the flame and the fluid dynamics which give rise the the combustion dynamics and fluctuations in flame structure described in the previous section, we employed a high-speed particle imaging velocimetry (PIV) system to measure the time-varying velocity field in the combustor. In this section, we will use results obtained from the PIV measurements to examine the dynamics of unstable flames in Mode II and Mode III.

The viewing area for the PIV measurements is the 76×76 mm area immediately downstream of the expansion plane, generating 800×800 pixel images of the seeding particles. These images are processed using a multi-pass approach, with the final pass using a 16×16 pixel window with 50% overlap. This produces a velocity field with a resolution of 100×100, corresponding to a spatial resolution of 0.76 mm.

To understand the interactions between the flame and the flow field, we need to know not only the time-varying velocity field in the combustor, but the correspondence between the velocity field and flame location at each point in time as well. Since simultaneous acquisition of PIV and chemiluminescence measurements is not possible in the present experimental setup, we use a phase-averaging procedure to integrate results from chemiluminescence and PIV measurements taken from separate experiments with the same combustor operating parameters. We use the pressure measurements recorded with each experiment as the reference source for calculating the phase. At the time instant corresponding to each chemiluminescence image or velocity field, a

best-fit sine wave for the pressure signal is calculated for a time interval spanning two periods of the instability frequency, and from this, the phase corresponding to that chemiluminescence image or velocity field is computed. The phase range from 0 to 2π is divided evenly into a number of intervals (usually 40), and the average of the images and velocity fields with phase in each interval is taken. This process produces a sequence of velocity fields and corresponding chemiluminescence images which span a cycle of the unstable combustion process.

As shown in Section 3.3, the flame shapes present in Mode II and Mode III are essentially axisymmetric. The images captured by the camera are integrated line-of-sight measurements of the chemiluminescent intensity. We can recover the underlying radial distribution of intensity by performing an appropriate tomographic reconstruction. In this case, we use the three-point discrete Abel deconvolution, as described by Dasch [11], using the modified and corrected formulas provided by Villarreal and Varghese [56].

Figure 3.12 shows a sequence of eight phase-averaged velocity fields corresponding to Mode IIb. The color indicates the magnitude of the axial velocity, with blue indicating flow in the forward direction, and red indicating flow in the reverse direction. The black arrows are streamlines which show the instantaneous direction of the local velocity. The corresponding series of deconvolved chemiluminescence images is shown in Figure 3.13, along with a plot showing the pressure integrated chemiluminescence intensity and mean inlet velocity over the course of the cycle.

There are three major features which generally characterize the flow: a strong annular jet issuing from the expansion plane at an angle to the axis of the combustor and aligning with the axis of the combustor as it reaches the outer wall; a large inner recirculation zone (IRZ) along the center of the combustor, extending upstream of the expansion plane and downstream of PIV interrogation region; and a small, toroidal outer recirculation zone (ORZ) between the jet and the expansion plane. The flame

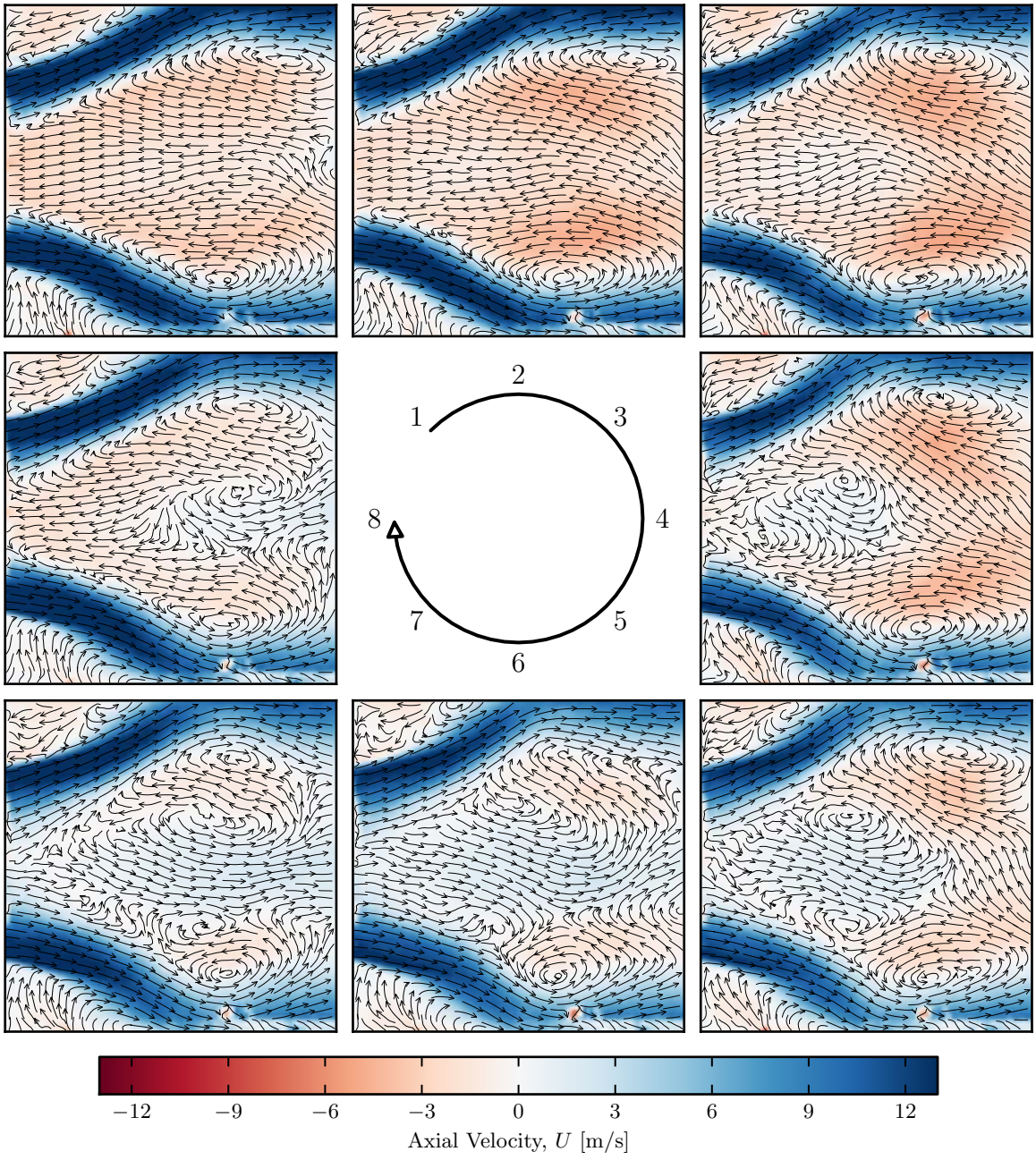

Figure 3.12: Phase-averaged axial velocity and streamlines in Mode IIb. The frequency of the instability is 36 Hz and the OASPL is 158 dB.

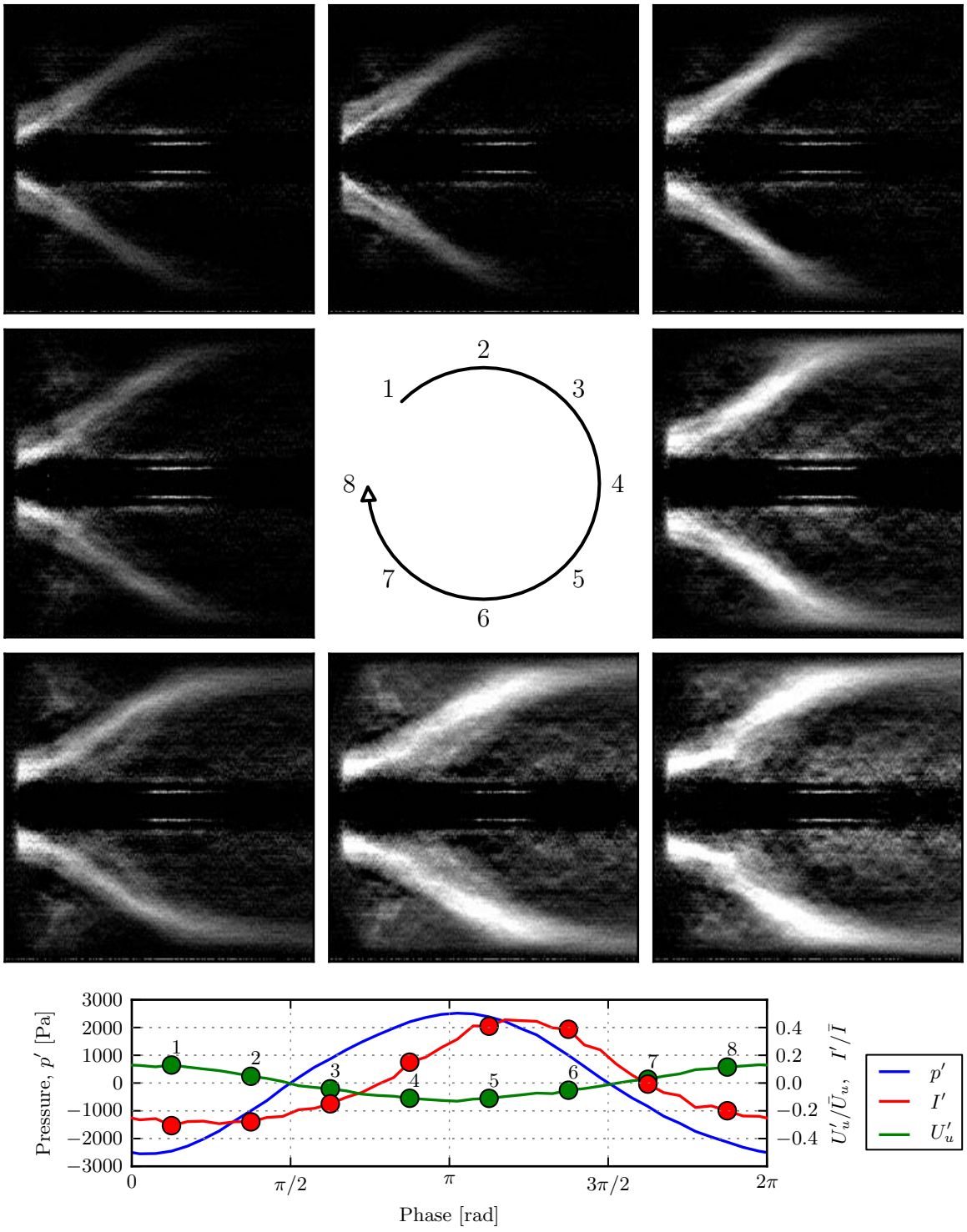

Figure 3.13: Phase-averaged, Abel-deconvolved chemiluminescence images in Mode IIb. Pressure, integral chemiluminescence intensity, and inlet velocity as a function of phase.

consists of a conical portion with the tip beginning just upstream of the sudden expansion and the base at the outer radius of the combustor followed by a cylindrical portion along the outer wall of the combustor. The cylindrical portion extends far downstream of the PIV measurement region. By comparing Figures 3.12 and 3.13, we can see that the flame is stabilized in the shear layer which separates the annular jet composed of fresh reactants from the inner recirculation zone containing the hot products.

Over the course of an unsteady cycle, the overall flame is relatively static. However, the total heat release rate indicated by the chemiluminescence intensity varies substantially, as does the instantaneous locus of heat release. We can follow the cycle as indicated in Figures 3.12 and 3.13, starting with time 1 where the heat release rate is at a minimum. At this instant, the pressure is near its minimum, the velocity of the jet emanating from the inlet channel is near its maximum, and the reverse flow in the central recirculation zone is uniformly strong. The heat release is concentrated at the tip of the conical section of the flame. As time advances, the flame grows in strength and the region of strong burning extends downstream (3–5). As the flame grows, the pressure increases, the strength of the jet decreases, and a region of forward flow forms along the centerline of the combustor. As this region of forward flow grows, it divides and weakens the IRZ. This process reduces the steep velocity gradient between the jet and the inner recirculation zone, increasing the extent of the low-velocity region in which the flame is stabilized, which in turn promotes expansion of the flame area and increased heat release rate. As the flame consumes the the available reactants, the heat release rate decreases, the strong inner recirculation zone re-forms, and the cycle starts anew.

Figure 3.14 shows a sequence of eight phase-averaged velocity fields corresponding to Mode IIIa. The corresponding series of deconvolved chemiluminescence images is shown in Figure 3.15, along with a plot showing the pressure integrated chemi-

luminescence intensity and mean inlet velocity over the course of the cycle. For these experiments, a fuel mixture consisting of 80% CO and 20% H_2 was used at an equivalence ratio of $\phi = 0.43$, an inlet temperature of $T_u = 300$ K, and a Reynolds number of 19,000.

In contrast to Mode IIb, here we observe large temporal variations in the structure of both the flame and the velocity field. At the beginning of the cycle (1), the flame is short and cylindrical, extending approximately one inlet diameter downstream of the expansion plane. The flame is confined to the shear layer between an annular jet of reactants emanating from the inlet channel and a small central recirculation zone. Downstream of this structure, the flow field is essentially uniform. As time progresses (2–3), both the jet of reactants and the inner recirculation zone grow axially, and the jet begins to angle away from the axis of the combustor. The flame length grows along with the shear layer between the jet and the IRZ, causing the total heat release rate to grow as well. After a time (4–5), the jet reaches its maximum extent and begins to weaken. The flame propagates radially outward through the weakened jet, consuming the reactants introduced by the jet (5–6). As the flame reaches the wall of the combustor, this pocket of reactants is exhausted, and that section of the flame is extinguished (7). Simultaneously, a new velocity surge from the expansion plane initiates the next cycle. The pressure and heat release rate are in phase throughout, which transfers energy to the acoustic field and reinforces the velocity oscillations necessary to sustain the cycle.

3.5 Thermoacoustic Instability Prediction

3.5.1 Combustor Acoustics

The acoustics of the swirl-stabilized combustor are modeled by solving the linear one-dimensional wave equation while neglecting viscous effects, using the method

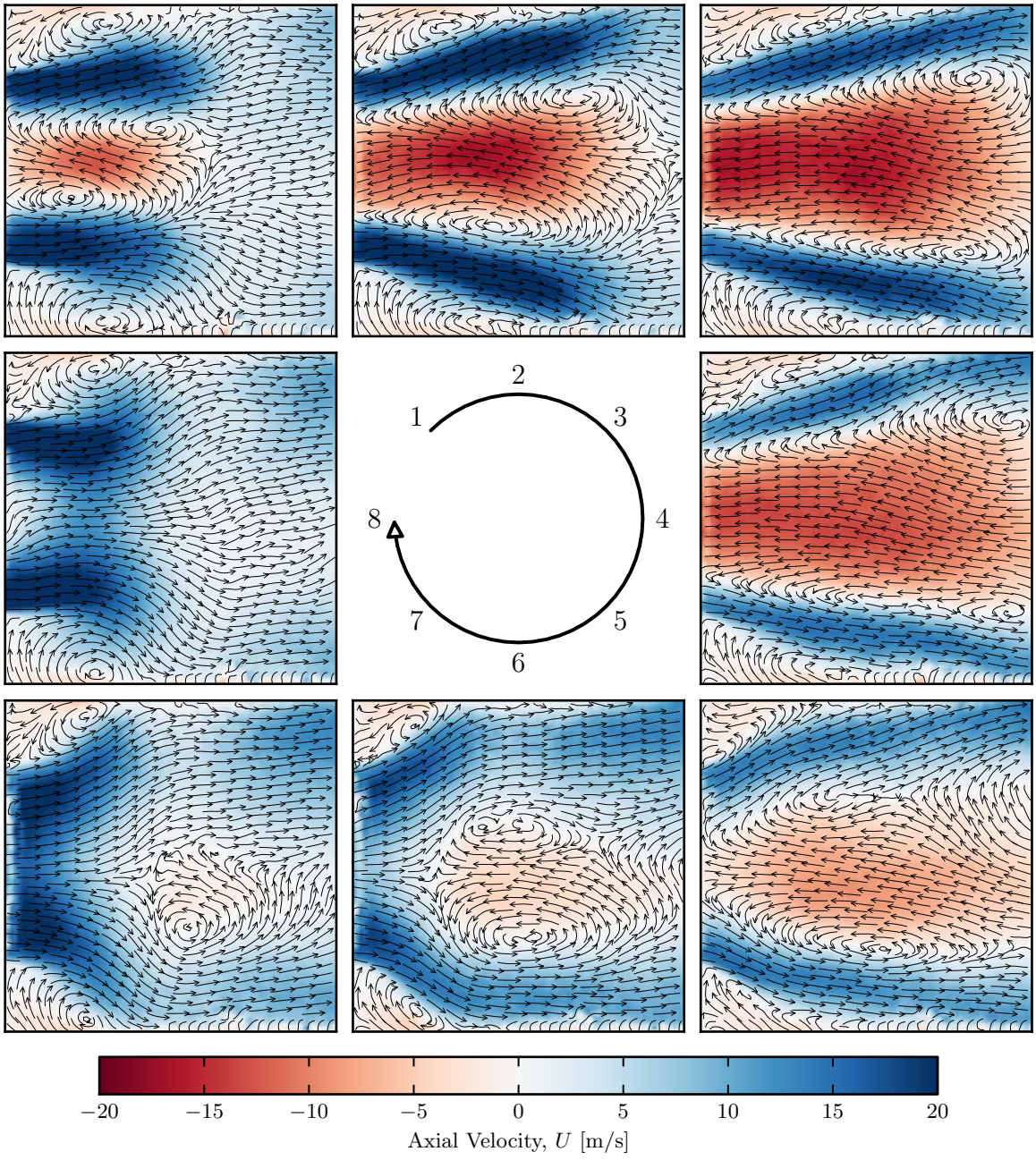

Figure 3.14: Phase-averaged axial velocity and streamlines in Mode IIIa. The frequency of the instability is 93 Hz and the OASPL is 161 dB.

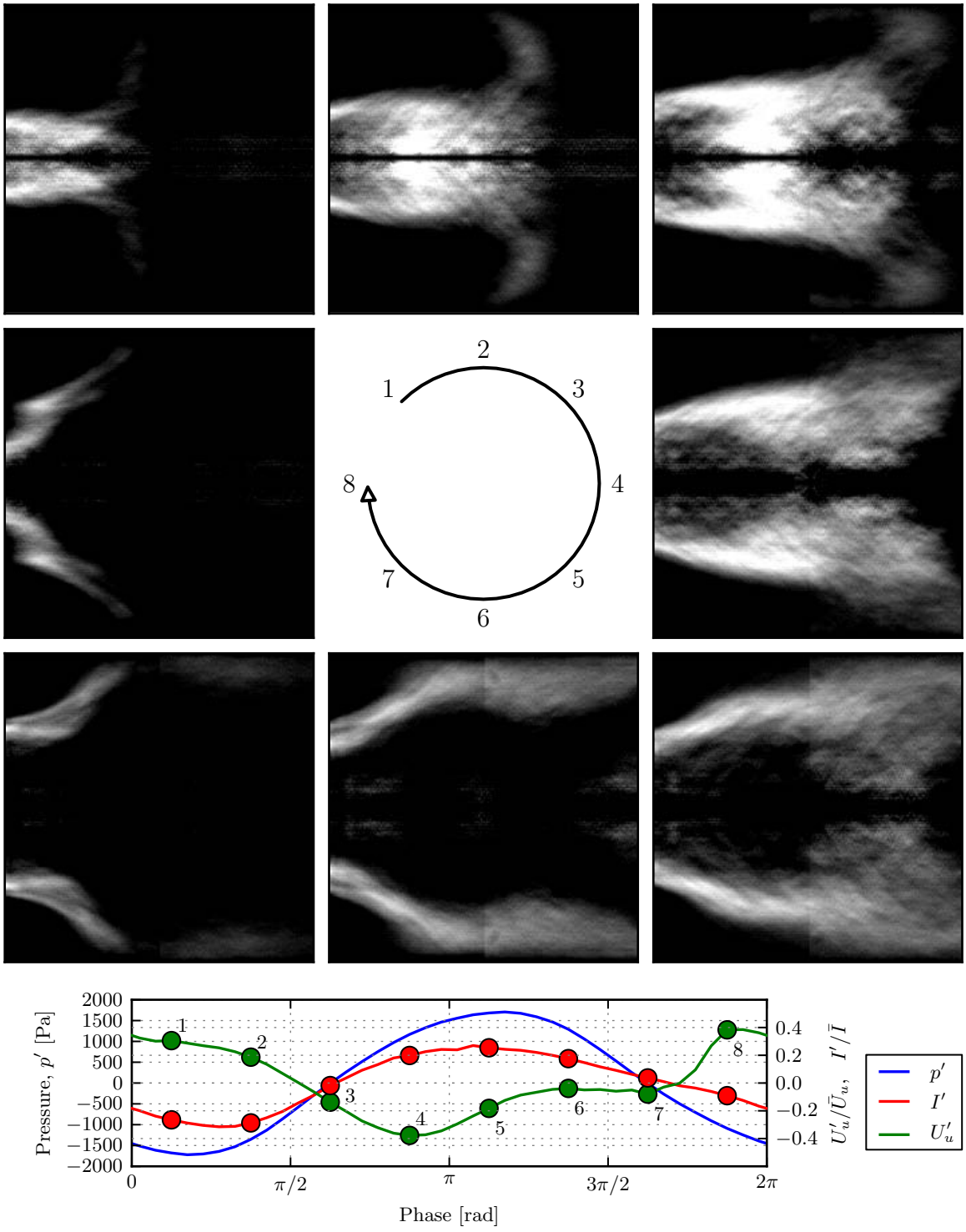

Figure 3.15: Phase-averaged, Abel-deconvolved chemiluminescence images in Mode IIIa. Pressure, integral chemiluminescence intensity, and inlet velocity as a function of phase.

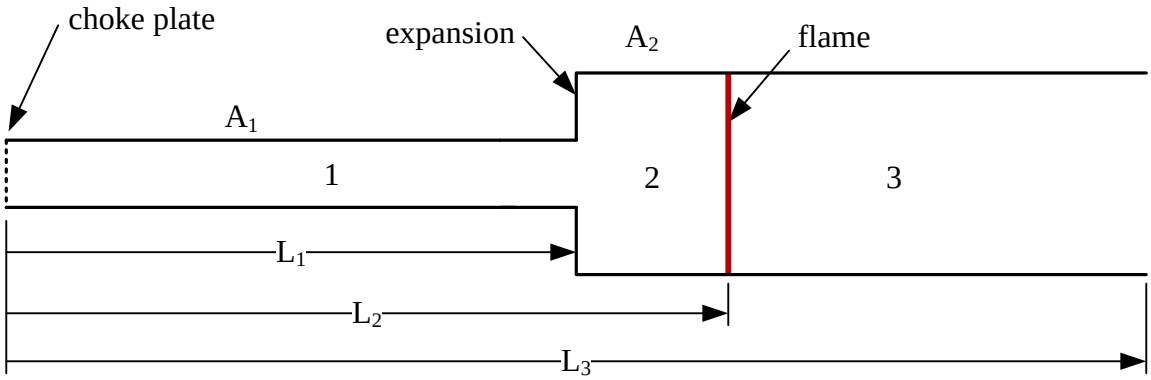

Figure 3.16: Simplified swirl combustor geometry used for acoustic modeling.

described by Dowling and Stow [14]. The one-dimensional pressure and velocity fields in the combustor can each be decomposed into their mean value plus a perturbation about that mean:

$$p(x,t) = \bar{p}(x) + p'(x,t) \tag{3.6}$$

$$u(x,t) = \bar{u}(x) + u'(x,t) \tag{3.7}$$

The Mach number of the flow in the swirl-stabilized combustor is very low (< 0.06), so the effect of mean flow may be neglected. Figure 3.16 shows a simplified schematic of the swirl-stabilized combustor, which shows the combustor divided into three different regions. The first section is the inlet channel upstream of the sudden expansion; the second section is between the sudden expansion and the combustion zone, which is assumed to be concentrated at a plane; the third section is the hot exhaust channel. For simplicity, we assume that the flame is located at a constant axial location downstream of the expansion. Within each region, the pressure satisfies the one-dimensional, homogeneous wave equation:

$$\frac{1}{\bar{c}^2}\frac{\partial^2 p'}{\partial t^2} - \frac{\partial^2 p'}{\partial x^2} = 0 \tag{3.8}$$

where $\bar{c}(x)$ is the mean local speed of sound. Applying conservation of momentum shows that the velocity perturbation $u'(x,t)$ satisfies:

$$\frac{\partial u'}{\partial t} = -\frac{1}{\bar{\rho}}\frac{\partial p'}{\partial x} \tag{3.9}$$

where $\bar{\rho}(x)$ is the mean local density. The general solution of Equation 3.8 is:

$$p'(x,t) = f(t - x/\bar{c}) + g(t + x/\bar{c}) \tag{3.10}$$

and the corresponding form of the velocity perturbation is:

$$u'(x,t) = \frac{1}{\bar{\rho}\bar{c}}\left[f(t - x/\bar{c}) - g(t + x/\bar{c})\right] \tag{3.11}$$

where f and g are arbitrary functions of a single variable. We now restrict f and g to functions of the form:

$$f(z) = \mathrm{Re}\left[\hat{f}e^{\mathrm{i}\omega z}\right] \tag{3.12}$$

$$g(z) = \mathrm{Re}\left[\hat{g}e^{\mathrm{i}\omega z}\right] \tag{3.13}$$

where the circumflex denotes a complex amplitude. The pressure and velocity perturbations may then be written as:

$$p'(x,t) = \mathrm{Re}\left[\hat{p}(x)e^{\mathrm{i}\omega t}\right] \tag{3.14}$$

$$u'(x,t) = \mathrm{Re}\left[\hat{u}(x)e^{\mathrm{i}\omega t}\right] \tag{3.15}$$

where $\hat{p}(x)$ and $\hat{u}(x)$ are defined as:

$$\hat{p}(x) = \hat{f}e^{-\mathrm{i}\omega x/\bar{c}} + \hat{g}e^{\mathrm{i}\omega x/\bar{c}} \tag{3.16}$$

$$\hat{u}(x) = \frac{1}{\bar{\rho}\bar{c}}\left[\hat{f}e^{-\mathrm{i}\omega x/\bar{c}} - \hat{g}e^{\mathrm{i}\omega x/\bar{c}}\right] \tag{3.17}$$

In each section of the combustor, Equations 3.16 and 3.17 give the pressure and velocity mode shapes. The resonant frequency ω and the constants $\hat{f}$ and $\hat{g}$ in each section follow from the application of continuity and conservation of momentum conditions at the boundary of each region of the combustor. At the inlet, the flow is choked, requiring:

$$\hat{u}_1(0) = 0 \tag{3.18}$$

Conservation of momentum at the sudden expansion, $x = L_1$, requires that the pressure perturbation be continuous:

$$\hat{p}_2(L_1) = \hat{p}_1(L_1) \tag{3.19}$$

From mass conservation, the velocity oscillations follow:

$$\hat{u}_1(L_1)A_1 = \hat{u}_2(L_1)A_2 \tag{3.20}$$

Between sections 2 and 3, we need to include the effect of heat addition at the location of the flame. The heat release rate oscillations are assumed to be linearly related to the pressure oscillations at the flame location with a phase lag:

$$Q'(t) = \Lambda e^{-\mathrm{i}\theta_{pq}} p'(L_2, t) \tag{3.21}$$

where $Q'(t)$ is the perturbation to the heat release rate per flame area. The heat release rate and pressure oscillations are out of phase by an angle θ_{pq}. From conservation of mass, the velocity jump condition across the flame is:

$$u_3'(L_2, t) = u_2'(L_2, t) + \frac{\gamma_u - 1}{\bar{\rho}_u \bar{c}_u^2} Q'(t) \tag{3.22}$$

where γ_u is the specific heat ratio in the reactants, $\bar{\rho}_u$ is the average density in the

reactants, and $\bar{c}_u$ is the average speed of sound in the reactants. Using Equation 3.21, Equation 3.22 becomes:

$$u_3'(L_2,t) = u_2'(L_2,t) + \frac{\gamma_u - 1}{\bar{\rho}_u \bar{c}_u^2} \Lambda e^{\mathrm{i}\theta_{pq}} p'(L_2,t) \tag{3.23}$$

Defining the normalized heat release parameter:

$$\beta \equiv (\gamma_u - 1)\Lambda / \bar{c}_u \tag{3.24}$$

we obtain the velocity jump condition across the flame as:

$$\hat{u}_3(L_f) = \hat{u}_2(L_f) + \frac{\beta e^{-\mathrm{i}\theta_{pq}}}{\bar{\rho}_u \bar{c}_u} \hat{p}_2(L_f) \tag{3.25}$$

The pressure oscillations across the flame is approximately continuous, giving:

$$\hat{p}_3(L_2) = \hat{p}_2(L_2) \tag{3.26}$$

The combustor exit is open to the atmosphere, thus:

$$\hat{p}_3(L_3) = 0 \tag{3.27}$$

Equations 3.18–3.20 and 3.25–3.27 are a system of six nonlinear equations in seven unknowns (ω, $\hat{f}_1$, $\hat{f}_2$, $\hat{f}_3$, $\hat{g}_1$, $\hat{g}_2$, and $\hat{g}_3$). Because we are only concerned with finding the mode shape, we may take $\hat{f}_1 = 1$ without loss of generality to obtain a set of six equations in six unknowns. Since these equations are linear in all variables except ω, the system can be reduced to a single nonlinear equation in ω, which can then be solved numerically.

The physical properties needed for these calculations are calculated for mixtures corresponding to the experimental conditions using Cantera [20]. The values of ω are

then calculated as a function of θ_{pq} and β. Except for the case when $\beta = 0$, the values of ω are complex; the frequency of the corresponding acoustic mode is $\mathrm{Re}(\omega)$, and the growth rate of the mode is $-\mathrm{Im}(\omega)$. For all cases where $|\theta_{pq}| < \frac{\pi}{2}$, the growth is positive, as expected from the Rayleigh criterion.

We can estimate the value of β using the PMT measurements discussed in Section 3.2.2. From Equations 3.21 and 3.24, we can show that:

$$\beta = \frac{\gamma_u - 1}{\bar{c}_u} \frac{Q'(t)}{p'(L_2, t)} \tag{3.28}$$

If we assume that the PMT signal $I(t)$ is directly proportional to heat release rate, then we can calculate β as:

$$\beta = \frac{\gamma_u - 1}{\bar{c}_u} \frac{\overline{Q}}{\overline{I(t)}} \frac{\mathrm{stdev}(I(t))}{\mathrm{stdev}(p'(L_2, t))} \tag{3.29}$$

where $\overline{Q}$ is the average heat release rate per unit area, calculated from the heating value and mass flow rates of the fuel components. The values of β calculated by this method for several combinations of fuel composition and inlet temperature are plotted as a function of equivalence ratio in Figure 3.17. At higher equivalence ratios, corresponding to operation in Mode III, the value of β tends to be between 1.0 and 3.0, increasing gradually with equivalence ratio. For those conditions corresponding to Mode IIb—near $\phi = 0.29$ at $T_u = 300$ K, 40% CO and $\phi = 0.37$ at $T_u = 300$ K, 80% CO—the value of β is approximately 0.6. In the stable operating modes (Mode I and Mode IIc), the value of β determined from these measurements is not physically meaningful, being determined primarily by the background flow noise in the combustor.

Figure 3.18 shows the first five resonant frequencies as a function of β and θ_{pq} for conditions corresponding to a syngas flame with a 60:40 CO:H_2 ratio at an equivalence ratio of 0.30 and an inlet temperature of 300 K. The temperature of the products is

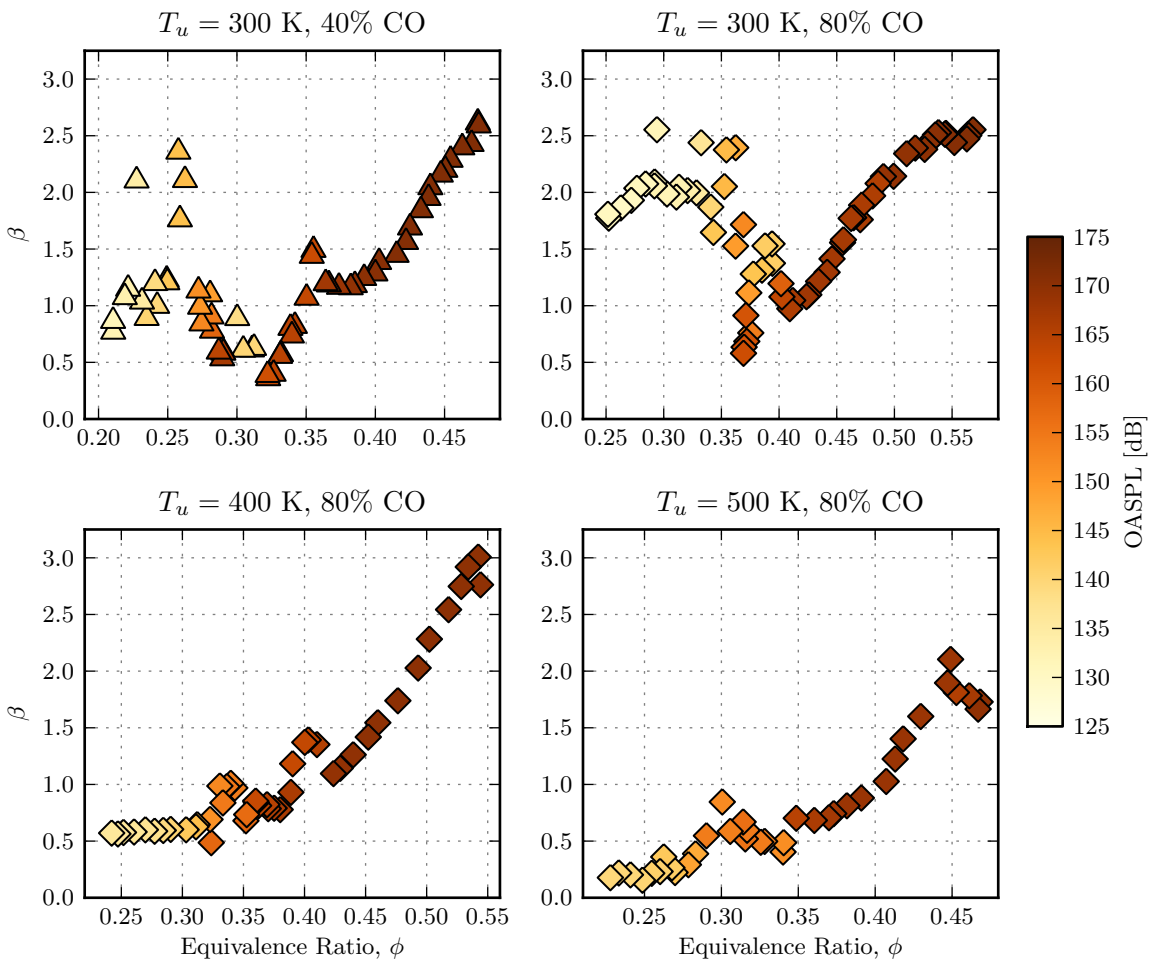

Figure 3.17: Heat release–pressure coupling magnitude measurements in the swirl combustor.

1251 K. The speed of sound is 355 m/s in the reactants and 680 m/s in the products. The density of the reactants is 1.12 kg/m^3 and the density of the products is 0.285 kg/m^3. The flame is assumed to be located 6 cm downstream of the sudden expansion.

For each acoustic mode, the resonant frequency has a fairly complex dependence on β and θ_{pq}. For the case where $\theta_{pq} = 0$, the frequency is nearly independent of β up to the critical value of $\beta_c \approx 2.25$, after which there is a rapid transition to a lower frequency, followed by insensitivity to β for all higher values of β. For values of $\beta < \beta_c$, the resonant frequency decreases with θ_{pq}. For $\beta > \beta_c$, there is a redistribution of the resonant frequencies. The family of modes at different

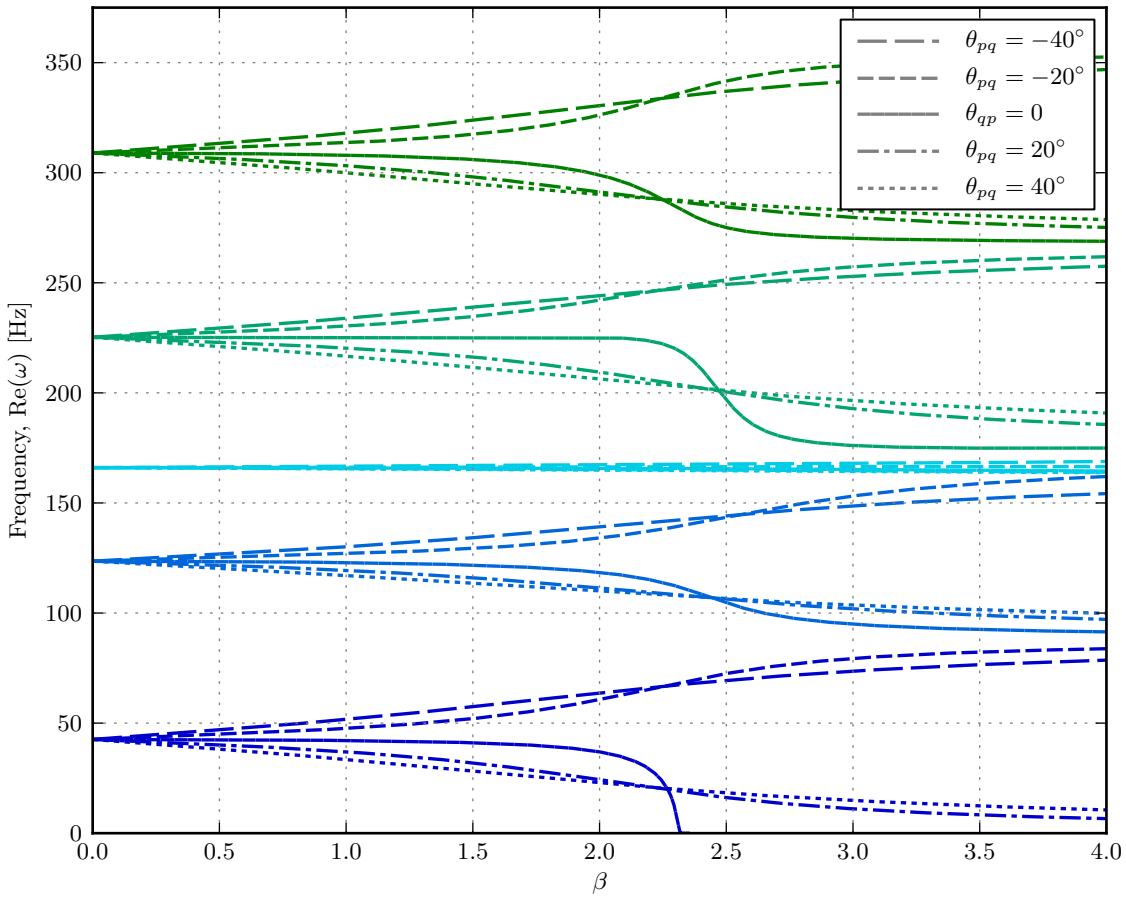

Figure 3.18: First five resonant frequencies as a function of the magnitude of the coupling between heat release rate and pressure with different phase angles between heat release rate and pressure.

values of θ_{pq} which originate from the same point at $\beta = 0$ split up, and the modes corresponding to $\theta_{pq} < 0$ regroup with the modes corresponding to $\theta_{pq} > 0$ from the next higher fundamental mode. In Figure 3.19, the pressure and velocity mode shapes for the first two acoustic modes are shown for $\theta_{pq} = -40°$, $0°$, and $40°$. β is equal to 1.0 in the left column and 3.0 in the right column. In each column, the modes are sorted in order of increasing frequency. For $\beta = 1.0$, there are two distinct mode shapes: one for frequencies centered around 40 Hz which resembles a 1/4 wave mode, and one for frequencies centered around 120 Hz which resembles a 3/4 wave mode. When the resonant frequency of the combustor has a finite growth rate, that

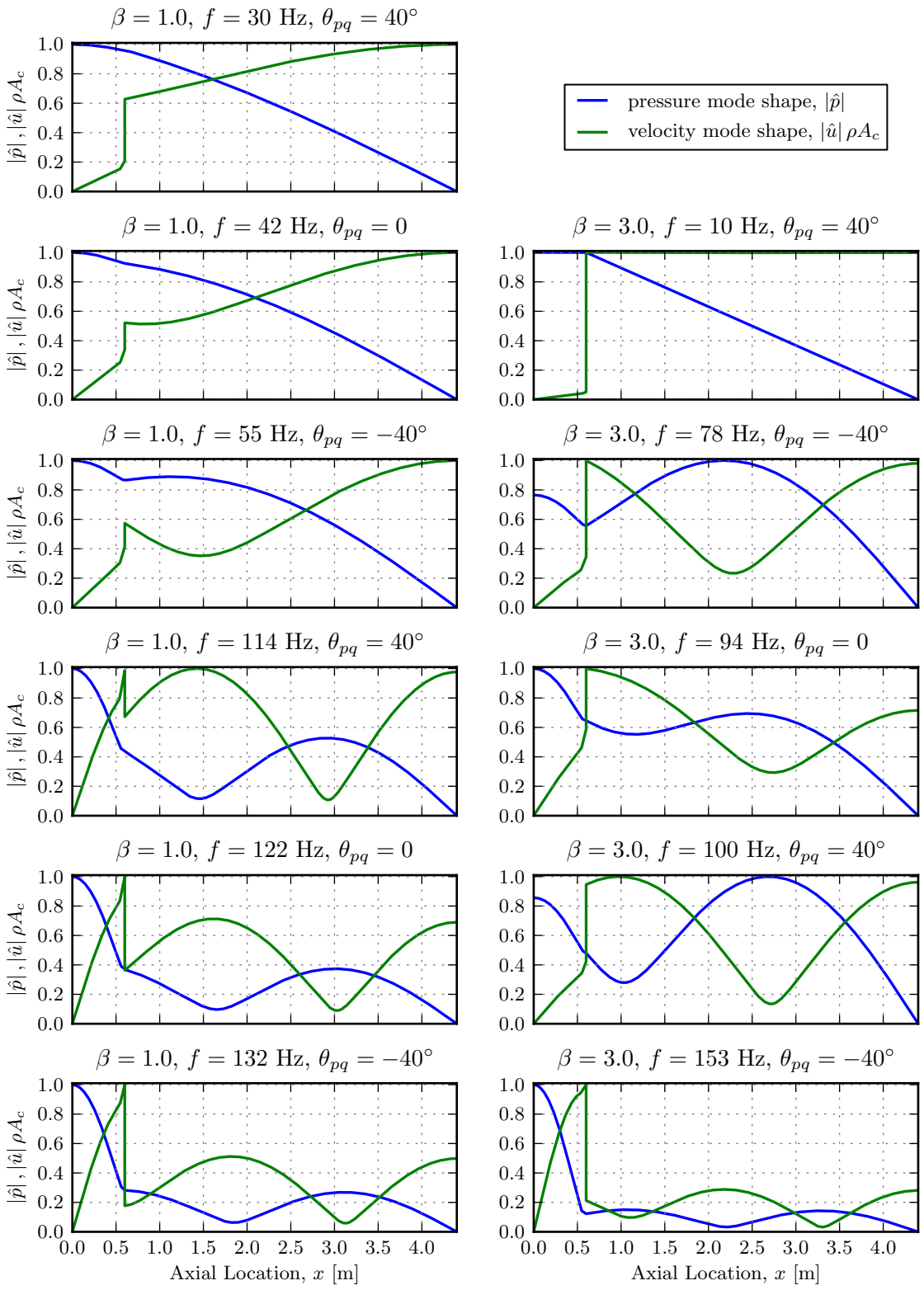

Figure 3.19: Pressure and velocity mode shapes in the swirl combustor.

is, when $\mathrm{Im}(\omega) \neq 0$, the mode shapes do not possess the clear pressure and velocity nodes which are characteristic of simpler acoustic systems. Instead, the pressure and velocity zero-crossings propagate downstream as a function of time, and new zero crossings form at the upstream boundary. As a result, the number of zero crossings varies as a function of time. This behavior of the mode shapes becomes stronger as $|\mathrm{Im}\,(\omega)|$ increases, making it difficult to classify the mode shapes at higher values of β. For $\beta = 3.0$, there are three distinct mode shapes: one for frequencies approaching 0 Hz, one for frequencies centered around 90 Hz, and one for frequencies centered around 160 Hz.

The experimentally-observed acoustic frequencies agree quite well with the calculated frequencies for small values of β. Additionally, the frequency within a given operating mode is relatively constant as θ_{pq} varies, and we do not observe the large changes in frequency expected at higher values of β. This suggests that the values of β calculated from the PMT measurements may be significantly higher than the actual values of β which characterize the combustor.

The phase between p' and u' at the flame location, θ_{pu}, is important to understanding the flame response to acoustic oscillations. The velocity oscillations in the unburned mixture, just upstream of the flame location, are approximately 90° out of phase with the pressure oscillations at the same location. With the modes ordered by increasing frequency, the pressure leads the velocity in modes 1, 2, 5 and 6; the velocity leads the pressure in modes 3 and 4. The magnitude of θ_{pu} increases slightly with β, and is nearly independent of θ_{pq}.

3.5.2 Combustion Time-Delay Model

Based on the heat release rate measurements of Section 3.2.2, we can see that as the equivalence ratio decreases, the heat release rate oscillations tend to lag behind the pressure oscillations. Since a decrease in the equivalence ratio implies a decrease in

the flame speed, this suggests that the interaction between the flame and the acoustics can be expressed in terms of a combustion time-delay which is inversely proportional to flame speed. In this section, we will develop a simple model for relating the flame speed to the phase between heat release rate and pressure.

The phase between pressure and heat release rate θ_{pq} is taken to be the sum of several components:

$$\theta_{pq} = \theta_{pu} + \theta_{ur} + \theta_{rq} \tag{3.30}$$

The phase between pressure and velocity θ_{pu} is determined by the combustor acoustics. Estimates for its value are taken from the acoustic model developed in the previous section. As described in Section 3.4, the growth of the inner recirculation zone is the precursor for the expansion of the flame surface area and the corresponding increase in heat release rate. The velocity and the size of the inner recirculation zone are separated by a phase angle θ_{ur}. Finally, the time it takes for the flame to consume the fresh mixture is inversely proportional to the flame speed:

$$\theta_{rq} = 2\pi f \tau_f = \frac{2\pi f L_c}{S_f} \tag{3.31}$$

where f is the frequency of the instability, τ_f is the flame propagation time constant, L_c is some characteristic length scale, and S_f is the (turbulent) flame speed. We now make two assumptions which restrict the selection of the dominant instability frequency: first, we assume that the flame propagation delay is less than the period of the instability, or $f \leq \tau_f^{-1}$; second, we assume that when there are multiple potentially unstable modes, the combustor preferentially couples with the highest frequency mode.

Using this model, Figure 3.20 shows the phase between heat release rate and pressure at the dominant acoustic mode as a function of the inverse of the flame propagation time constant. Here, θ_{ur} is taken to be 180°. θ_{pu} is taken to be 120°

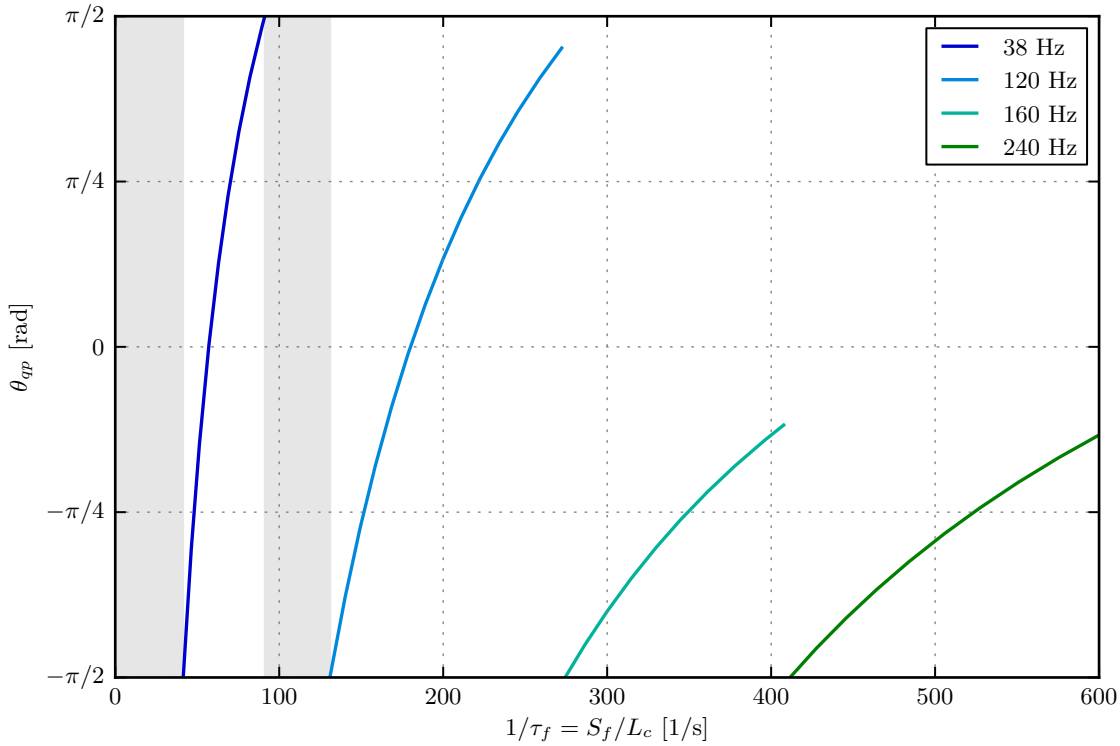

Figure 3.20: Predicted phase between pressure and heat release rate oscillations in the swirl-stabilized combustor as a function of flame speed.

for the 38 Hz and 120 Hz modes, and $-120°$ in the 160 Hz and 240 Hz modes. Starting at high flame speeds, pressure and heat release rate oscillations are in phase in the 240 Hz mode, corresponding to Mode IIIc of the combustor. As the flame speed decreases, the heat release rate oscillations lag further and further behind the pressure oscillations, until they reach $\theta_{qp} = -\pi/2$ at $\tau_f^{-1} = 410\,\mathrm{s}^{-1}$, at which point the instability frequency drops to 160 Hz, corresponding to Mode IIIb of the combustor. Further decreasing the flame speed brings this mode to $\theta_{qp} = -\pi/2$ at $\tau_f^{-1} = 270\,\mathrm{s}^{-1}$, where the flame transitions to the 120 Hz mode, corresponding to Mode IIIa of the combustor. When θ_{qp} reaches $-\pi/2$ in this mode, however, there is no acoustic mode for which the heat release rate oscillations and pressure oscillations are in phase. This stable region between $\tau_f^{-1} = 130\,\mathrm{s}^{-1}$ and $\tau_f^{-1} = 90\,\mathrm{s}^{-1}$ corresponds to Mode IIc of the combustor. When the flame speed decreases sufficiently such that $\tau_f^{-1} < 90\,\mathrm{s}^{-1}$, the

flame is able to couple with the acoustic mode at 38 Hz, corresponding to Mode IIb of the combustor. For $\tau_f^{-1} < 40\,\mathrm{s}^{-1}$, the flame propagates too slowly to couple with any of the acoustic modes, corresponding to the behavior of Mode I of the combustor.

This model demonstrates that the sequence of transitions between operating modes observed in the swirl-stabilized combustor can be predicted by expressing the phase between heat release rate and pressure oscillations in terms of a time delay inversely proportional to the flame speed. The onset of combustion instability and the selection of specific acoustic modes is governed by the interactions between the flame front and the velocity field in which the flame is stabilized. Therefore, we should expect inlet mixtures with different fuel compositions but similar flame speeds to exhibit similar combustion dynamics.

3.6 Strained Flame Modeling

In this section, we will derive the relationships among flame speed, flame shape and stretch in a simple flame holder. Based on the nondimensional scaling implied by this simple model, we use the numerical results described in Chapter 2 to develop a function which collapses the experimental data obtained in the swirl-stabilized combustor over the full range of inlet conditions explored.

3.6.1 Flame Shape, Flame Speed, and Stretch

To understand the relationship between flame shape and flame stretch, consider the flame holder geometry shown in Figure 3.21, which consists of a small bluff body mounted at the center of a circular duct of radius R. If, for the sake of simplicity, we neglect the effects of viscosity and the density jump across the flame ($\rho_u = \rho_b$), then the axial velocity will be U_u everywhere. If we further assume that the flame propagates into the unburned mixture at a constant flame speed of S_f, the flame will

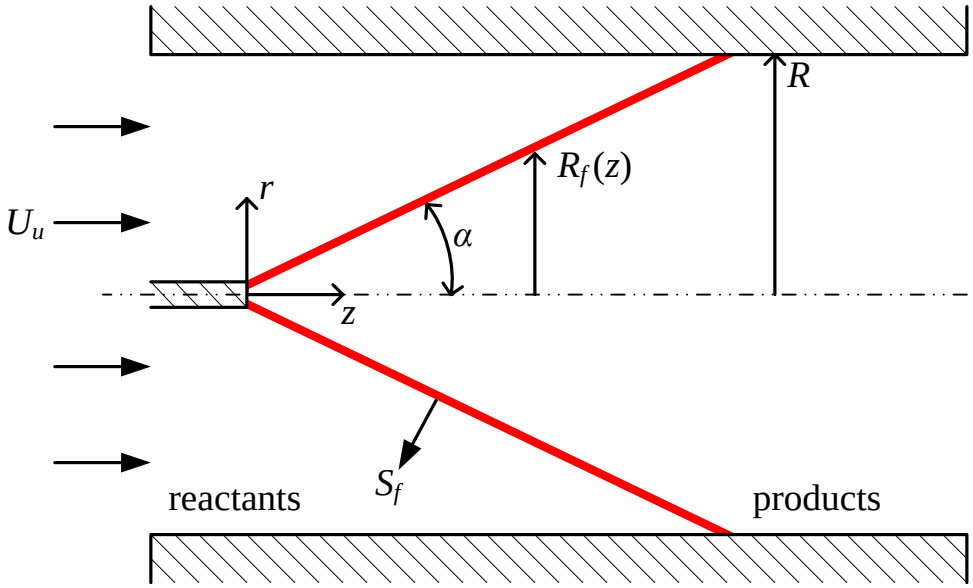

Figure 3.21: Inverted conical flame.

be that of an inverted cone, as shown in Figure 3.21. The opening angle of the cone, α, can be found by equating the mass flux through the duct with the mass flux across the flame surface:

$$\rho_u \pi R^2 U_u = \frac{\pi R^2}{\sin \alpha} S_f \tag{3.32}$$

$$\alpha = \arcsin \frac{S_f}{U_u} \tag{3.33}$$

At a fixed flame speed, an increase in the inlet velocity requires a proportional increase in the flame area, which is achieved by decreasing the opening angle of the flame. The stretch rate, κ, at any point along the flame surface is given by Law [30] as

$$\kappa\,(r) = \frac{U_u \sin 2\alpha}{2r} \tag{3.34}$$

The average strain rate over the entire flame surface, $\bar{\kappa}$, can be found by integration:

$$\bar{\kappa} = \frac{1}{A}\int_A \kappa \, dA \tag{3.35}$$

$$= \frac{\sin\alpha}{\pi R^2}\int_0^R \frac{2\pi r}{\sin\alpha}\kappa\left(r\right)\, dr \tag{3.36}$$

$$\bar{\kappa} = \frac{U_u \sin 2\alpha}{R} \tag{3.37}$$

At this point, we can combine Equations 3.33 and 3.37 and eliminate the flame opening angle to find the relationship between stretch and flame speed:

$$\frac{\bar{\kappa}R}{U_u} = \sin\left(2\arcsin\frac{S_f}{U_u}\right) \tag{3.38}$$

This equation has several important implications. First, it demonstrates that that there is a relationship between stretch and flame speed which is dictated by the shape of the flame and the velocity field in which the flame is anchored. Second, it reveals the appropriate dimensionless form for this relationship: the nondimensionalized stretch rate:

$$\kappa^* \equiv \bar{\kappa}R/U_u \tag{3.39}$$

is a function of the nondimensionalized flame speed:

$$S^* \equiv S_f/U_u \tag{3.40}$$

For a particular fuel mixture, we can find the nondimensional flame speed and stretch rate at which the flame is stabilized by finding the intersection of Equation 3.38 and the flame speed as a function of stretch rate as determined by the numerical simulations of Chapter 2. This is shown in Figure 3.22(a) for $U_u = 0.5\,\mathrm{m/s}$ and $R = 5.0$ mm, using a fuel mixture consisting of 60% carbon monoxide and 40% hydrogen at an equivalence ratio of $\phi = 0.400$ and an inlet temperature of $T_u = 300$ K.

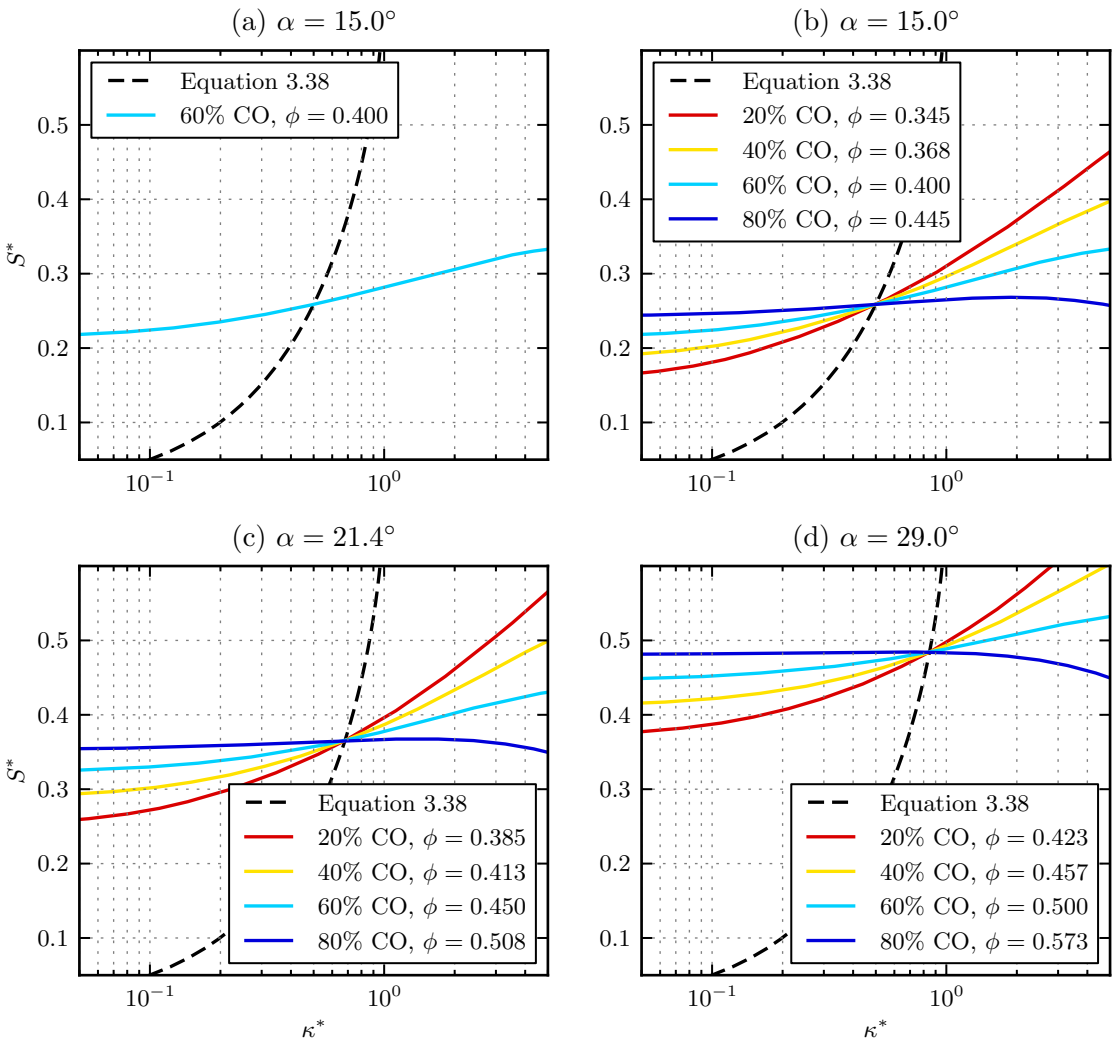

Figure 3.22: Families of conical flames with identical flame shapes.

For these inlet parameters, the flame is stabilized with an opening angle of $\alpha = 15°$, a nondimensionalized flame speed of $S^* = 0.26$, and a nondimensionalized stretch rate of $\kappa^* = 0.50$, corresponding to a flame speed of 0.13 m/s and a stretch rate of 50 s^{-1}. Now consider what happens when we change the fuel composition to a more hydrogen-rich mixture. The flame speed will increase, resulting in a decrease in the cone angle α. If we then decrease the equivalence ratio until the intersection with the curve from Equation 3.38 occurs at the same point as before, we will obtain a second flame with the same flame speed, stretch rate, and flame shape,

but for a different fuel composition and equivalence ratio. More generally, there is a family of operating conditions—combinations of fuel composition, inlet temperature and equivalence ratio—for which the $S^*(\kappa^*)$ curves all intersect at a single point corresponding to a particular combination of flame speed, stretch rate and flame shape, as shown in Figure 3.22(b). For a different flame shape, the characteristic flame shape and stretch rate will change, and so too will the corresponding family of operating conditions, as shown in Figures 3.22(c) and 3.22(d). In this case, as the equivalence ratio increases at a fixed fuel composition, the flame opening angle and the stretch rate increase as well. In the next section, we will use this relationship in reverse in order to identify the flame speed and flame stretch which characterize a family of flames with the same flame shape by finding the intersection of their $S^*(\kappa^*)$ curves.

While the function derived here is only valid for this particular geometry, we can anticipate the existence relationships among flame shape, flame speed, and stretch of the form:

$$\alpha = f\left(S^*\right) = g\left(\kappa^*\right) \tag{3.41}$$

for any flame holder geometry, where α is not necessarily something as simple as the flame opening angle, but is rather a generic surrogate for the flame shape. In reality, the flow field in the vicinity of the flame will be altered by the expansion of the burned gas, affecting the flame shape and the stretch rate along the flame surface. Thus, both of these functions should depend on the density ratio ρ_u/ρ_b:

$$\alpha = f\left(S^*, \frac{\rho_u}{\rho_b}\right) = g\left(\kappa^*, \frac{\rho_u}{\rho_b}\right) \tag{3.42}$$

Finally, it is necessary to recall that the flame speed is a function of both the stretch rate and the properties of the fuel–air mixture: temperature, fuel composition, and equivalence ratio. In order for two flames propagating into mixtures with different

Table 3.2: Transitional equivalence ratio for various fuel compositions at selected mode transitions.

Transition identifier	20% CO	40% CO	60% CO	80% CO
$T_u = 300$ K, Mode IIIa, lower limit	0.286	0.319	0.352	0.401
$T_u = 300$ K, Mode IIIb, $\theta_{pq} = 0$	0.351	0.394	0.453	0.539
$T_u = 400$ K, Mode IIIb, lower limit	0.265	0.299	0.339	0.398
$T_u = 500$ K, Mode IIb, upper limit	0.220	0.250	0.284	0.330

properties to have the same flame shape, they must have the same flame speed at the stretch rate which corresponds to that flame shape. It is through this implicit link between flame speed and stretch rate that we can extract the relationship defined by the functions f and g as shown in Equation 3.42.

3.6.2 Application to Swirl Combustor

In Section 3.3, the the various operating modes of the combustor were shown to be associated with changes in the flame anchoring geometry, and, in the case of the unstable flames, unsteady flame–vortex interactions. Therefore, we can use the operating conditions (inlet temperature, fuel composition and equivalence ratio) at the points of transition to identify sets of conditions which produce identical flame shapes. We can also use measurements of the phase between heat release rate and pressure, discussed in Section 3.2.2, as a surrogate for flame shape by categorizing flames with the same p'–q' phase in a particular mode as having the same flame shape.

For each operating condition corresponding to a particular transition, we compute the flame speed as a function of stretch rate. The resulting curves should intersect at a single point, giving the flame speed and stretch rate which coincide with this flame shape.

The operating conditions for several transitions at different fuel compositions and inlet temperatures are given in Table 3.2. The equivalence ratio at the point of

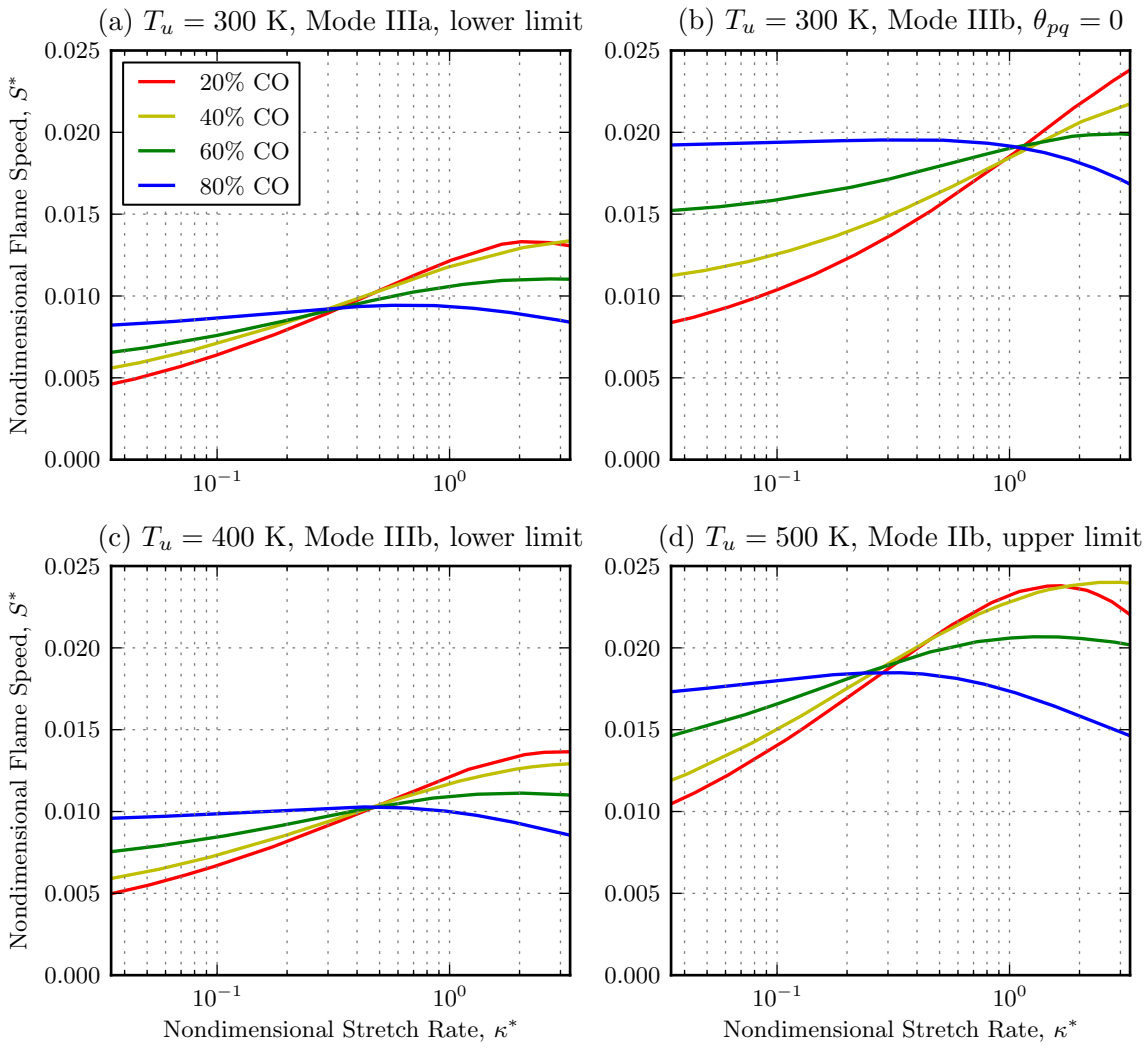

Figure 3.23: Flame consumption speed as a function of stretch rate for mixture corresponding to selected mode transitions.

transition is determined by manually inspecting plots of the OASPL, peak acoustic frequency and phase between heat release rate and pressure. The flame speeds for each of these mixtures is shown as a function of stretch rate in Figure 3.23. When the combustor inlet temperature is 300 K, the curves corresponding to the the low equivalence ratio limit of Mode IIIa (110 Hz instability) intersect at a stretch rate of 80 s^{-1} and a consumption speed of 9.9 cm/s, (Figure 3.23(a)). When the pressure and heat release are exactly in phase in Mode IIIb (160 Hz instability), the curves intersect at a stretch rate of 273 s^{-1} and a consumption speed of 20.9 cm/s

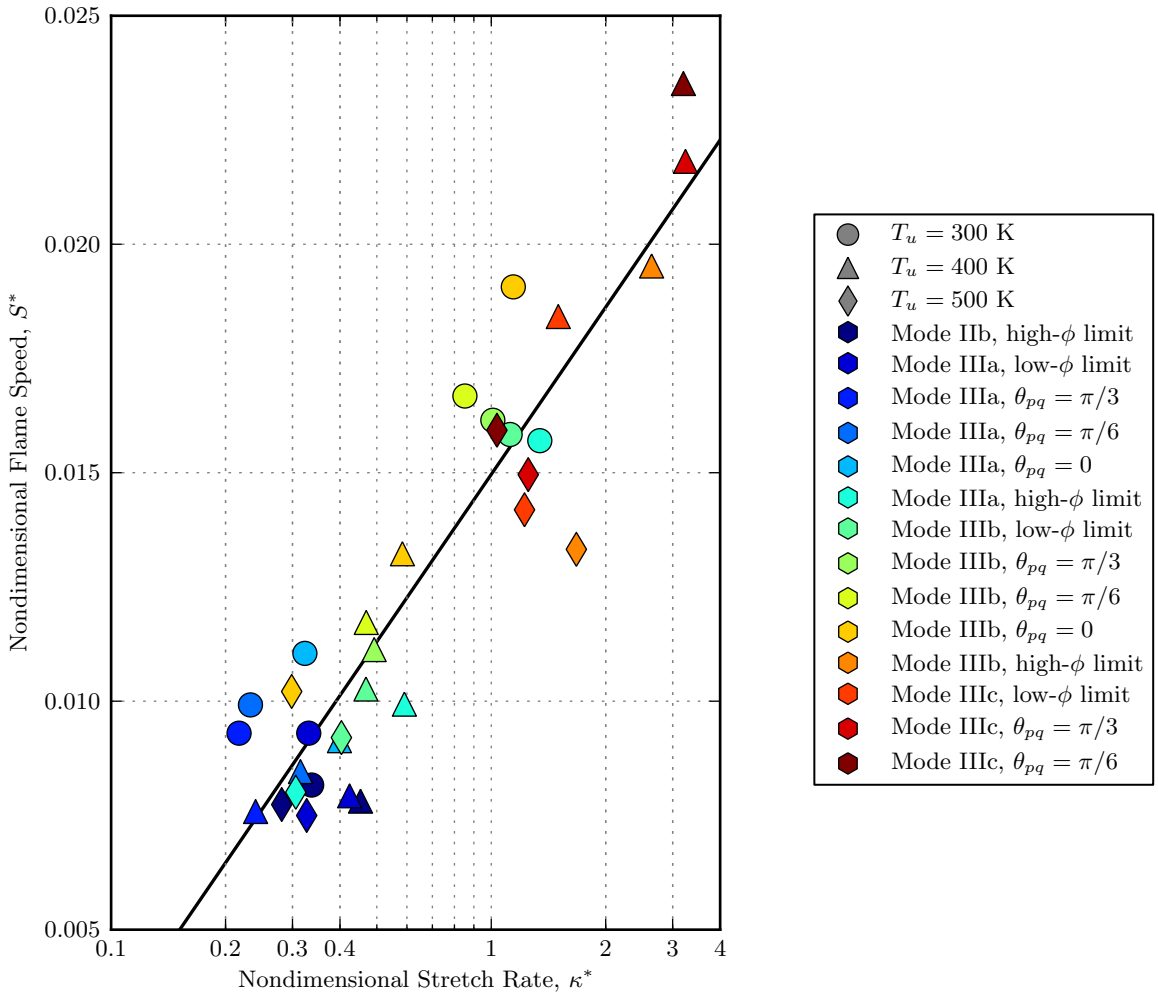

Figure 3.24: Consumption speeds and stretch rates of identifiable operating points in the swirl combustor and the best-fit line for these data.

(Figure 3.23(b)). With a combustor inlet temperature of 400 K, the low equivalence ratio limit of Mode IIIb produces curves intersecting at a stretch rate of 191 s^{-1} and a consumption speed of 18.2 cm/s (Figure 3.23(c)). When the inlet temperature is 500 K, the curves corresponding to the upper equivalence ratio limit of Mode IIb (40 Hz instability) intersect at at stretch rate of 172 s^{-1} and a consumption speed of 20.2 cm/s (Figure 3.23(d)).

For each fuel composition and inlet temperature, transitional operating points are identified corresponding to the upper and lower equivalence ratio limits of Modes IIb,

IIIa, IIIb, and IIIc. Operating points corresponding to pressure–heat release phase angles of 0, $\pi/6$ and $\pi/3$ are identified for Modes IIIa, IIIb, and IIIc. For each operating point, the flame speed and stretch rate intersection is found by minimizing:

$$\frac{\text{stdev}\big(\mathbf{S}(\kappa^*)\big)}{\text{mean}\big(\mathbf{S}(\kappa^*)\big)} \tag{3.43}$$

with respect to κ^*, where $\mathbf{S}$ is the set comprising the flame speeds for each of the cases corresponding to that operating point. Not all of these operating points can be identified for all fuel compositions and inlet temperatures. In total, there are 34 cases where a specific transition could be identified for at least three fuel compositions at a particular inlet temperature. The consumption speeds and stretch rates at each of these transitions are plotted in Figure 3.24. The operating points lie along the curve:

$$S^* = 0.00536 \, \ln\left(19.08 \, \kappa^*\right) \tag{3.44}$$

where the constants have been determined by a least-squares fit of the points. While the data do show a relatively clear relationship between κ^* and S^* that works across the complete parameter space, Figure 3.24 reveals that the correspondence between S^* and the operating mode does not hold for changes in the inlet temperature. For instance, at the points where $\theta_{pq} = 0$ in Mode IIIb, shown in yellow, the value of S^* decreases from 0.0187 to 0.0128 to 0.0098 as the inlet temperature increases from 300 K to 400 K to 500 K. On the other hand, for the high equivalence ratio limit of Mode IIb, shown in dark blue, S^* is practically independent of temperature. The model developed here, then, is a single formula which is applicable at all inlet temperatures and for all fuel compositions, but which does not explain the correspondence of operating modes at different inlet temperatures.

3.6.3 Modifications to Account for Density Ratio

To have a single model which effectively collapses the data over the entire parameter space of fuel compositions, equivalence ratios, and inlet temperatures, we must include the density ratio across the flame in the correlation. In principle, one could use any arbitrary function of two variables for each of the functions f and g defined in Equation 3.42. At present, we will restrict ourselves to functions of the following form:

$$\alpha = f\left(\left(\frac{\rho_u}{\rho_b} + c\right)^q S^*\right) = g\left(\left(\frac{\rho_u}{\rho_b} + b\right)^p \kappa^*\right) \tag{3.45}$$

Note that unlike in the example of Section 3.6.1, α here is a numerical surrogate for the dynamic flame shape, rather than a directly measurable property. Therefore, without loss of generality, we may simply let $f(x) = x$.

An extensive search of the space defined by the undetermined parameters p, q, b, and c reveals that the best fit for the experimental data occurs for $p = q = b = -1$ and $c = 0$. For convenience, we define the density-weighted flame speed:

$$\tilde{S} \equiv \left(\frac{\rho_u}{\rho_b}\right)^{-1} S^* = \left(\frac{\rho_u}{\rho_b}\right)^{-1} \frac{S_c}{U_u} \tag{3.46}$$

and density weighted stretch rate:

$$\tilde{\kappa} \equiv \left(\frac{\rho_u}{\rho_b} - 1\right)^{-1} \kappa^* = \left(\frac{\rho_u}{\rho_b} - 1\right)^{-1} \frac{\kappa R}{U_u} \tag{3.47}$$

We are now looking for a function g that satisfies:

$$\alpha = \tilde{S} = g\left(\tilde{\kappa}\right) \tag{3.48}$$

Figure 3.25 shows the density-weighted flame speed $\tilde{S}$ as a function of the density-weighted stretch rate $\tilde{\kappa}$ for several of the previously identified operating points.

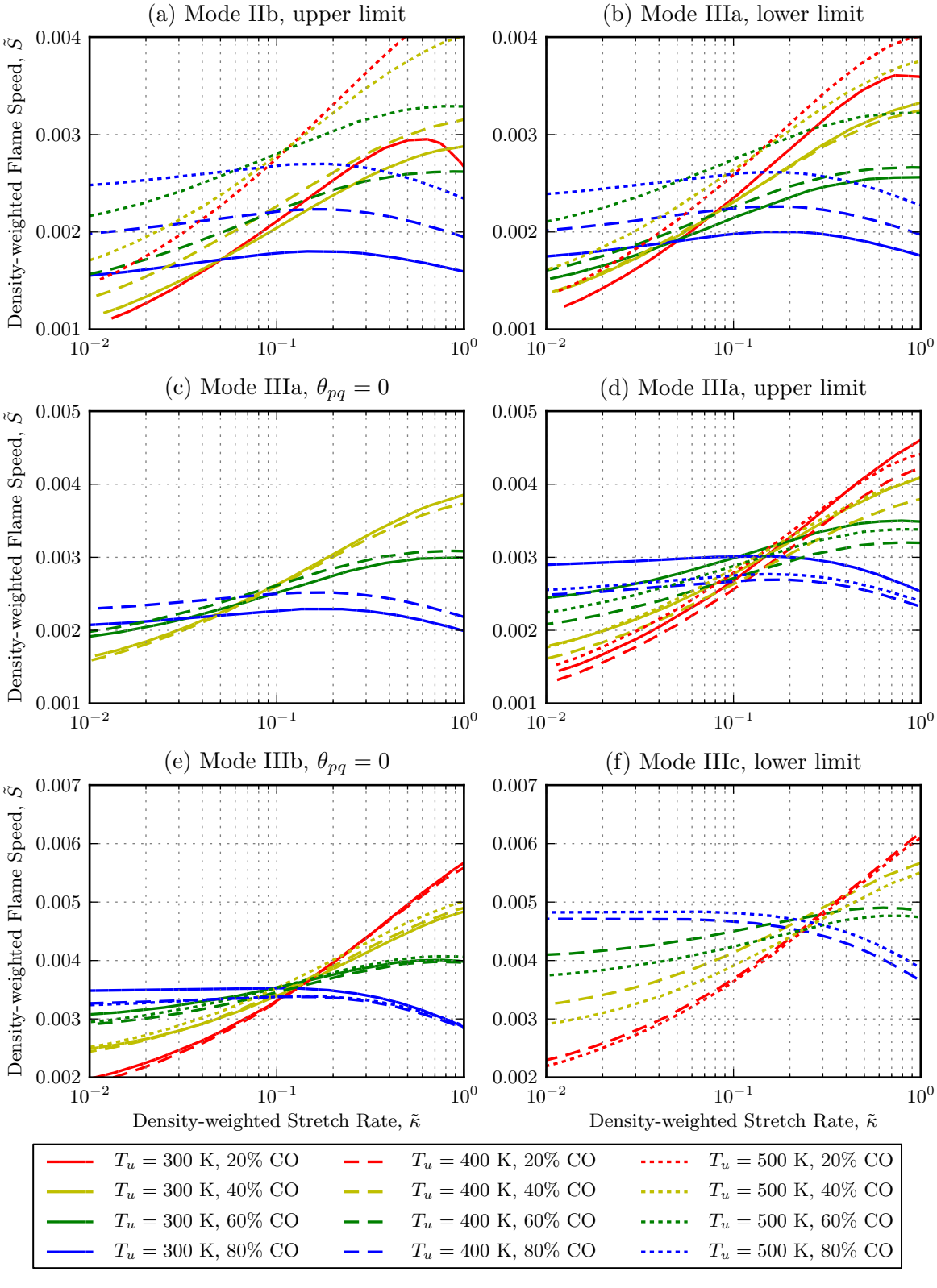

Figure 3.25: Density-weighted flame speed as a function of density-weighted stretch rate for selected operating points in the swirl combustor.

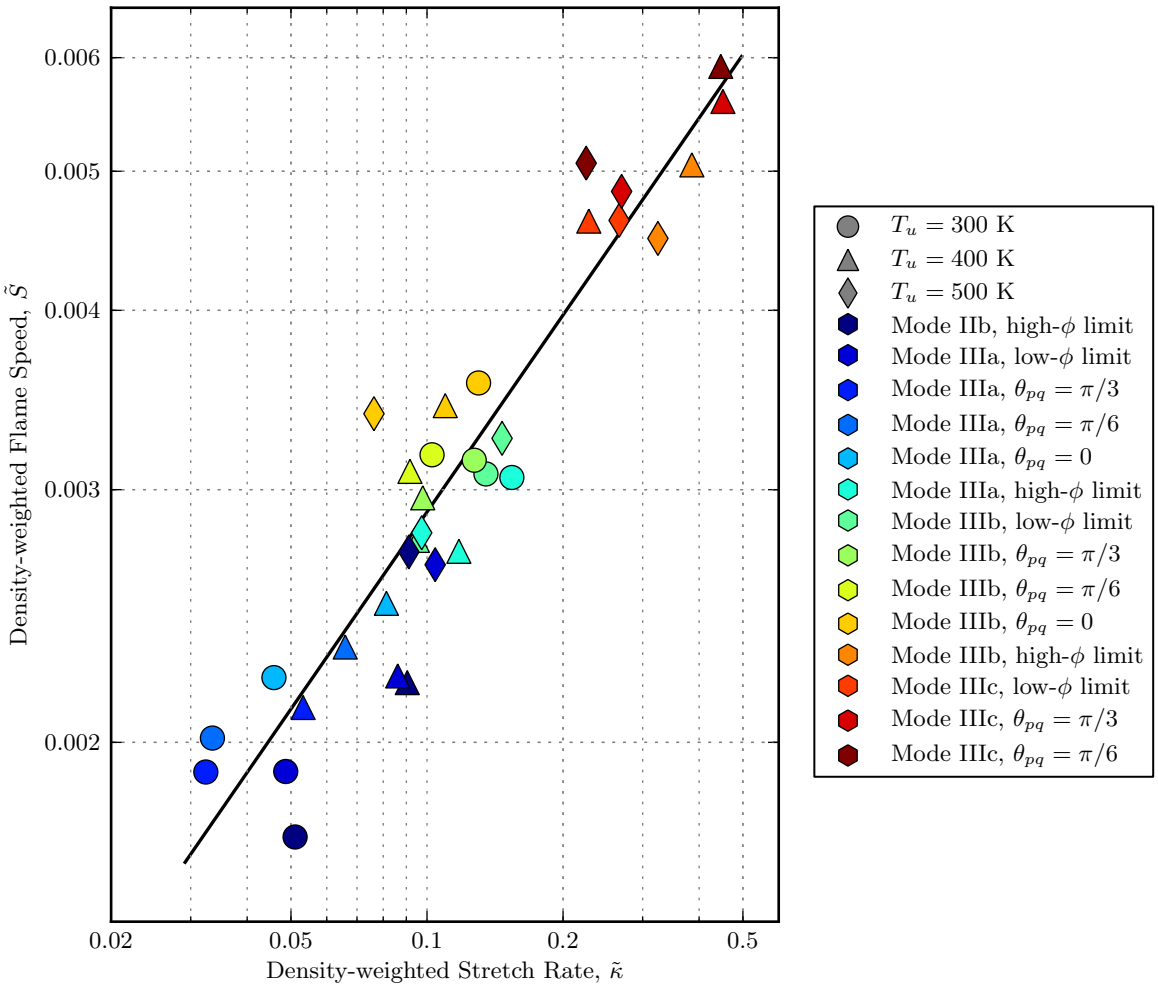

Figure 3.26: Nondimensional density-weighted flame speeds and stretch rates of identifiable operating points in the swirl combustor and the best-fit line for these data.

With the exception of the first two operating points—the upper limit of Mode IIb (Figure 3.25(a)) and the lower limit of Mode IIIa (Figure 3.25(b))—the set of curves corresponding to each transition intersect near a single point. Even in these two cases, the curves corresponding to cases at the same inlet temperature appear to converge at a single point. The density-weighted flame speed and stretch for each operating condition at each inlet temperature, calculated by minimizing the quantity defined in Equation 3.43, are shown in Figure 3.26. In contrast to the results

shown in Figure 3.24, the correspondence among operating points at different inlet temperatures is much better when the effects of the density ratio across the flame have been taken into account. Progressing through the modes in the order defined, both $\tilde{S}$ and $\tilde{\kappa}$ increase essentially monotonically. The operating points appear to follow a power-law relationship. The formula for this relationship, found using a least-squares fit, is:

$$\tilde{S} = 0.00827\,\tilde{\kappa}^{\,0.456} \tag{3.49}$$

The best demonstration of the effectiveness of this fit is seen by applying it to the original experimental data. Instead of plotting the OASPL as a function of equivalence ratio, in Figure 3.27 we plot the data as a function of the density-weighted flame speed computed using Equation 3.49. Here we can see that the experimental data are fit well by the model. The transition from one mode to the next at a particular temperature occurs at essentially the same value of $\tilde{S}$ for each fuel composition. The fit is better for the transitions between the higher-frequency unstable modes (Modes IIIa, IIIb, and IIIc) which all have similar flame dynamics than it is for the low-frequency unstable mode (Mode IIb) where the adjacent modes have significantly different flame shapes and dynamics. In reality, the dependence of flame shape on density ratio and flame speed is certainly more complex than the form assumed here, and those differences will be most pronounced across the sudden changes in flame shape which define some of the observed mode transitions. Nevertheless, the correlation developed here does a remarkably accurate job of capturing the mode transitions across the entire experimental parameter space without introducing a high degree of complexity.

3.7 Summary

In this chapter, we studied the dynamic operating modes present in a laboratory-scale swirl-stabilized combustor when burning mixtures of hydrogen and carbon

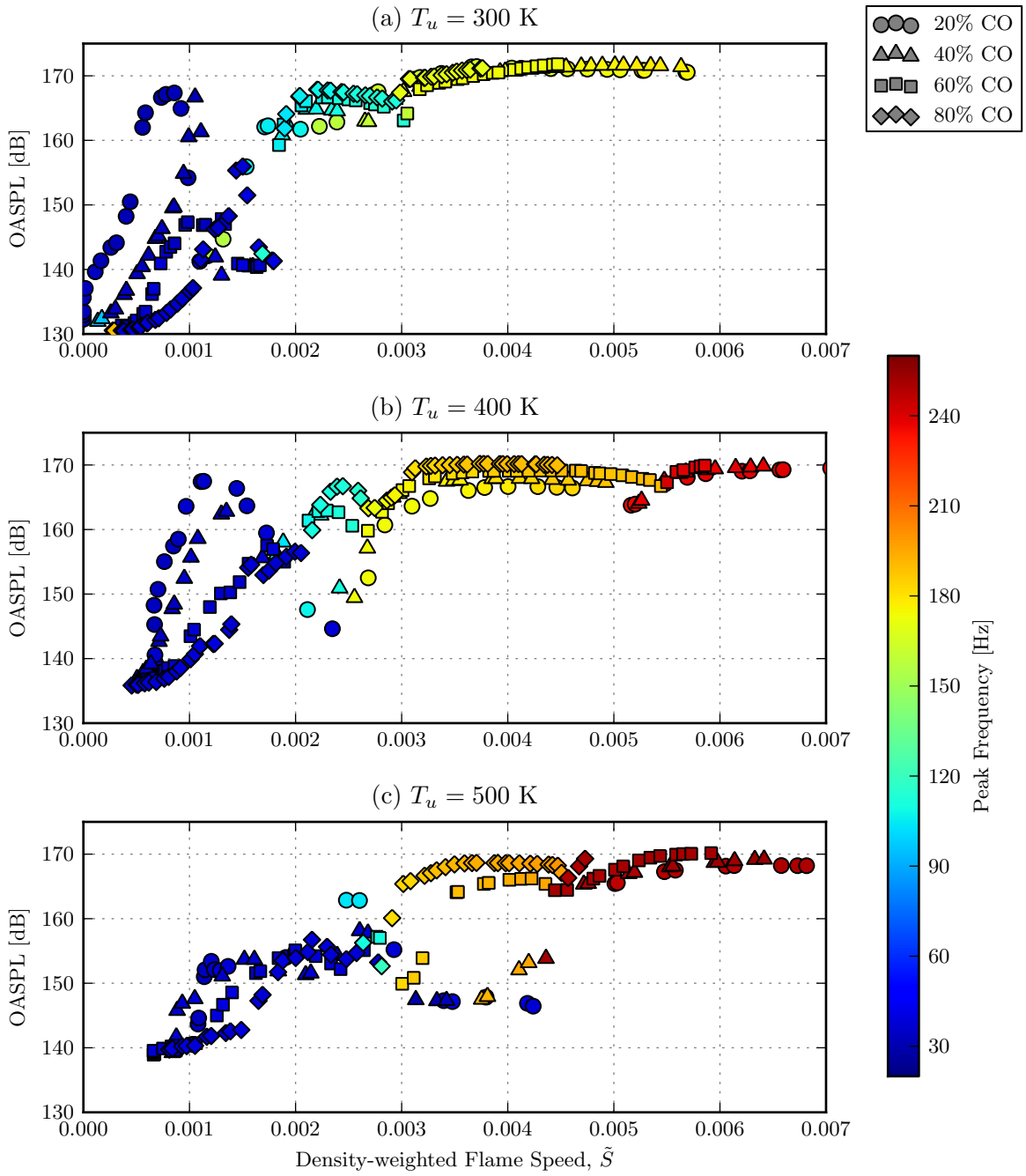

Figure 3.27: Overall sound pressure level as a function of density-weighted flame speed for all fuel compositions, equivalence ratios, and inlet temperatures in the swirl-stabilized combustor.

monoxide over a range of equivalence ratios and inlet temperatures. We saw that there are a number of distinct operating modes which can be distinguished by the amplitude and frequency of the acoustic pressure measured in the combustor. Changes between different operating modes are associated with changes in the structure of the flame, indicating that it is the interaction between the flame and the local flow field which determines the operating mode. Detailed analyses of the flame structure, using high-speed chemiluminescence measurements, and the flow field, using particle imaging velocimetry, are used to explore these interactions. The unstable modes are characterized by cyclic changes in the extent and structure of the inner recirculation zone which encourages the growth of the flame surface area.

We use a one-dimensional thermoacoustic model of the combustor to predict the unstable frequencies of the combustor. By accounting for the time it takes for the flame to propagate into the flow structures generated by the dynamics of the inner recirculation zone oscillations, we show that the dynamic mode selection of the combustor is a function of flame speed. By accounting for the effects of stretch and density ratio on the propagation of the flame, we can construct a similarity transformation which converts the dependence of operating mode on inlet temperature, fuel composition, and equivalence ratio into a dependence on the density-weighted flame speed. This result shows that local transport–chemistry interactions are important in determining overall system dynamics, and confirms the role of turbulent flame propagation in driving thermoacoustic instabilities.

Chapter 4

Step Combustor

In this chapter, we will study the combustion dynamics observed in a planar backward-facing step combustor, which, like the swirl-stabilized combustor discussed in Chapter 3, operates at atmospheric pressure in the lean premixed mode. Fuels consisting of carbon monoxide and hydrogen at various concentrations were tested over a range of equivalence ratios. Additional tests were performed using mixtures of propane and hydrogen at varying concentrations over a range of equivalence ratios and inlet temperatures. Dynamic pressure measurements were taken for each case. High-speed video was used to explore the dynamic interactions between the flame and the flow field of the combustor.

As in the swirl-stabilized combustor, a sequence of stable and unstable operating modes are identified in the combustor, with each mode being characterized by a distinct dynamic flame shape and acoustic response which depends on the composition of the reactants and the inlet temperature. The unstable modes are associated with interactions between the flame and a large wake vortex which is periodically shed from the backward-facing step as a result of acoustically-driven velocity oscillations.

The modeling tools developed to explain the combustion dynamics of the swirl-stabilized combustor are applied to the step combustor to similar effect. The

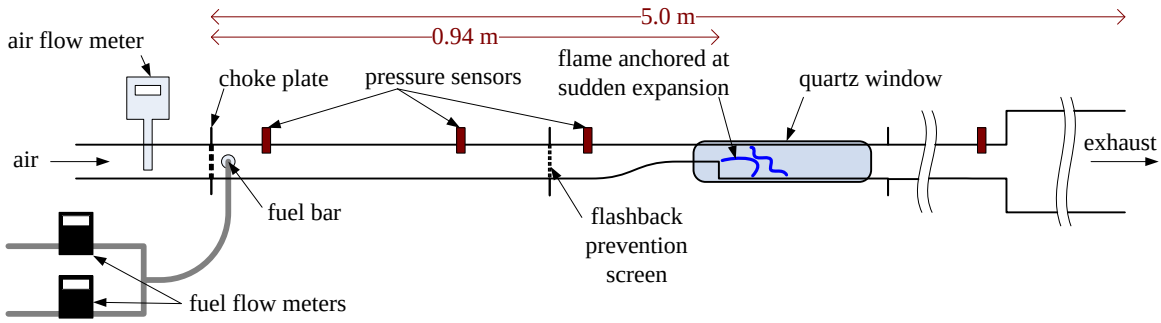

Figure 4.1: Schematic of the backward-facing step combustor.

effectiveness of the model at describing combustion dynamics in combustors with different flame anchoring geometries demonstrates its generality, and underscores the dependence of combustion dynamics on fundamental flame physics.

4.1 Experimental Setup

The backward-facing step combustor, shown schematically in Figure 4.1, consists of a rectangular stainless steel duct with a rectangular cross-section 40 mm high and 160 mm wide. The air inlet to the combustor is choked. 0.5 m downstream from the choke plate, a 0.2 m long ramp contracts the channel height from 40 mm to 20 mm, followed by a 0.2 m long constant-area section followed by a sudden expansion back to 40 mm which serves as the flame anchoring point. The step height is 20 mm, giving an expansion ratio of 2:1. The overall length of the combustor is 5.0 m. A circular exhaust pipe with a diameter of 178 mm comprises the last 3.0 m of the combustor. Quartz viewing windows installed in the vicinity of the step provide optical access. Fuel is injected through several spanwise holes through a manifold located 2 cm downstream of the choke plate. The large distance between the fuel bar and the step creates a substantial convective delay during which equivalence ratio oscillations are damped as a result of turbulent mixing. The fuel and air supply systems, along with the diagnostic instruments, are shared with the swirl-stabilized combustor, and have

Table 4.1: Operating modes of the backward-facing step combustor.

Mode	Frequency	OASPL
I	—	< 135 dB
II	35–40 Hz	135–150 dB
IIIa	35–40 Hz	> 150 dB
IIIb	120–130 Hz	> 150 dB

been described in detail in Section 3.1.

4.2 Operating Modes

To determine the stability map of the backward-facing step combustor, we conducted two series of experiments where the inlet conditions were varied while dynamic pressure were recorded. In the first series of experiments, we varied the fuel composition from 20% CO and 80% hydrogen to 80% CO and 20% hydrogen by volume, in increments of 10%. In the second series of experiments, we used propane–hydrogen fuel mixtures with C_3H_8:H_2 ratios of 50:50, 70:30 and 100:0, and varied the inlet temperature from 300 K to 600 K in increments of 100 K. For each fuel composition and inlet temperature, we varied the equivalence ratio of the fuel–air mixture from near the lean blowoff limit up to a value approaching the flashback limit.

The Reynolds number, based on the step height of 20 mm, was held constant at 6,500 for all tests. This corresponds to a mean inlet velocity of 5.2 m/s at 300 K, which increases to 8.5 m/s at 400 K, 12.5 m/s at 500 K and 16.9 m/s at 600 K. The inlet velocity varies by less than $\pm 10\%$ as a function of fuel composition and equivalence ratio.

As the input parameters vary, we can identify several distinct operating modes of the combustor, characterized by the amplitude and frequency of pressure oscillations

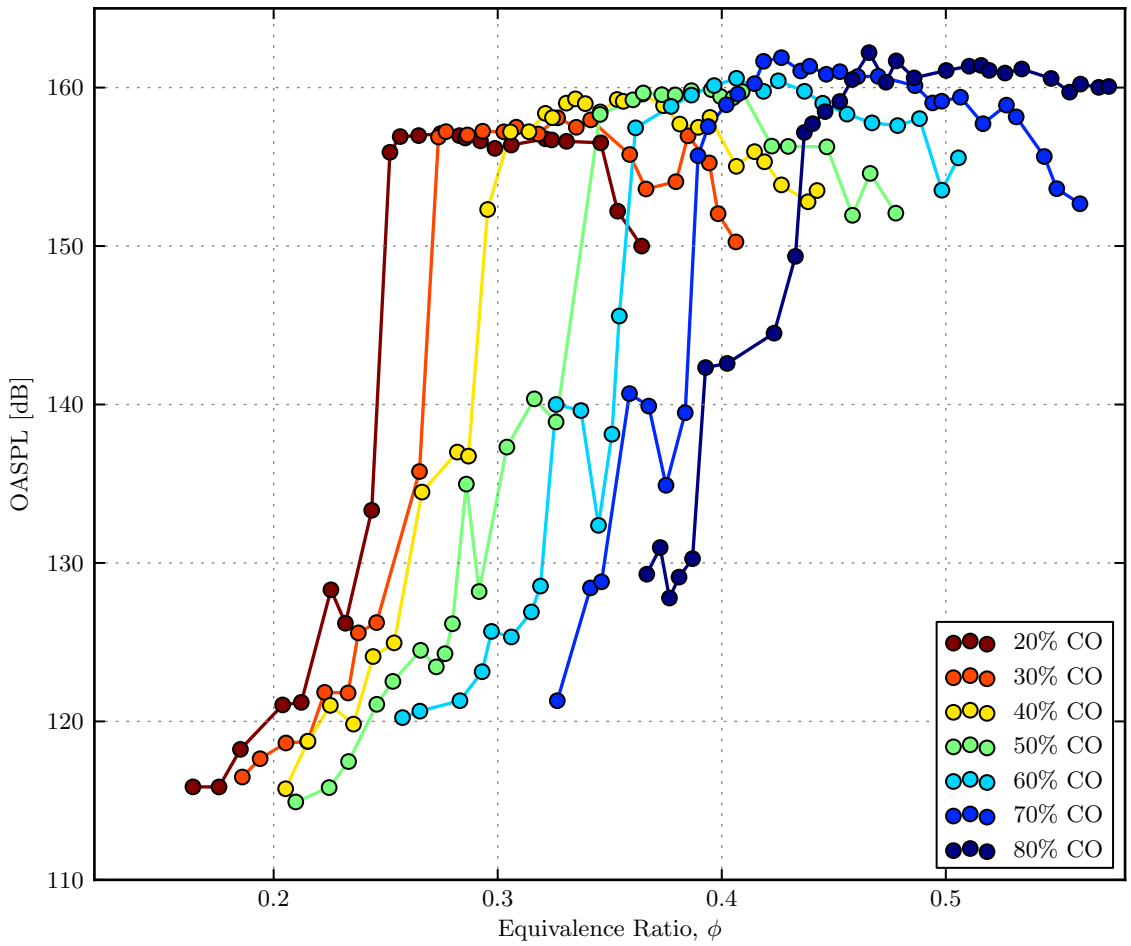

Figure 4.2: Overall sound pressure level as a function of equivalence ratio for a range of carbon monoxide–hydrogen mixtures.

in the combustor and by the dynamic flame anchoring configuration. The frequencies and overall sound pressure levels (OASPL) in each operating mode of the swirl-stabilized combustor are shown in Table 4.1. The major mode, indicated by the Roman numeral, represents a particular dynamic flame shape. The characteristics of each dynamic flame shape are discussed in detail in Section 4.3. The minor mode, indicated by a lowercase letter, is used to differentiate flames with similar shapes but distinct acoustic responses. At a fixed inlet temperature and fuel composition, gradually increasing the equivalence ratio causes the combustor to transition from one mode to the next in the order shown.

In Figure 4.2, we show the overall sound pressure level as a function of equivalence ratio for various carbon monoxide–hydrogen fuel mixtures. For each fuel composition, a similar set of behaviors is observed. At equivalence ratios near the lean flammability limit, the flame is stable (Mode I) with an overall sound pressure level of about 120 dB. As the equivalence ratio is increased beyond a certain threshold, the combustor transitions to a quasi-stable operating condition (Mode II) with a typical sound pressure level of 135 dB. While the flame remains attached to the step, it experiences strong fluctuations, as can be seen in the chemiluminescence images in Section 4.3. The quasi-stable transition is marked by the knee in the curve almost half-way between the stable and unstable regimes. In some cases, the quasi-stable region is narrow enough that it is only represented by a single data point. The pressure oscillation amplitude in the quasi-stable region decreases as the amount of hydrogen in the fuel is increased. Further increasing the equivalence ratio pushes the combustor into the unstable region with high amplitude pressure oscillations of around 160 dB. In these cases, the flame detaches from the step during part of each cycle. At higher equivalence ratios still, the flame anchors upstream of the sudden expansion on the flashback prevention screen. As the amount of hydrogen in the fuel increases, the flammability limits and stability transitions shift to lower equivalence ratios. This shift appears to be a result of the increase in flame speed with increasing hydrogen content. The extended lean flammability limit of hydrogen expands the stable operating region.

In Figure 4.3, we show the OASPL as a function of equivalence ratio for propane hydrogen mixtures of different compositions over a range of inlet temperatures. At an inlet temperature of 300 K, the acoustic response for propane–hydrogen mixtures is similar to that of the syngas mixtures shown in Figure 4.2, with perhaps an even more clear separation between the stable (Mode I) and quasi-stable (Mode II) conditions. As the inlet temperature is increased, the response curves for all fuel compositions

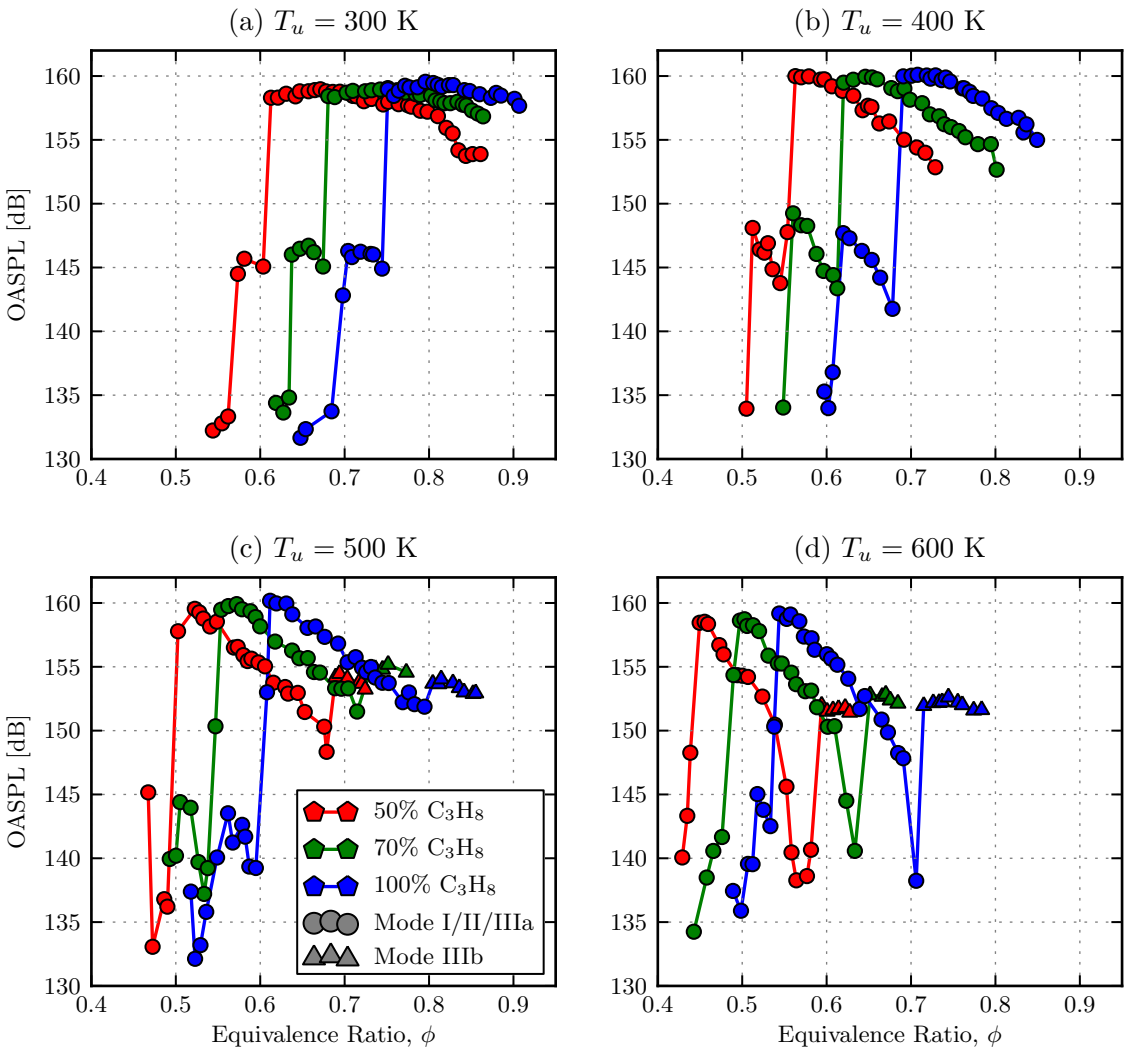

Figure 4.3: Overall sound pressure level as a function of equivalence ratio for a range of propane–hydrogen mixtures and inlet temperatures.

shift to lower equivalence ratios, consistent with the increase in flame speed. The OASPL in Mode IIIa begins to decrease with increasing equivalence ratio, with the slope increasing at higher inlet temperatures. Once the inlet temperature reaches 500 K, we see a jump in the OASPL at high equivalence ratios, which marks the onset of the high-frequency unstable mode, Mode IIIb.

4.3 Flame Chemiluminescence

In this section, we will examine the dynamic flame shapes of syngas flames in the backward-facing step combustor in each of the previously-defined combustor operating modes, with the goal of understanding how the interactions between the flame and the velocity field in the flame-anchoring region give rise to the heat release dynamics which characterize each mode.

In Figure 4.4, a sequence of chemiluminescence images for a stable flame (Mode I) are shown. The inlet conditions for this case were an 80:20 CO:H_2 fuel mixture at an equivalence ratio of 0.38 and and an inlet temperature of 300 K. In this mode, small vortices are shed from the step at a frequency which is not coupled with an acoustic mode of the combustor. The heat release rate and pressure are essentially uncoupled. The burning zone highlights a typical shear layer structure often observed in stable combustion between two streams, with shedding and downstream pairing of eddies [19, 51].

A typical cycle of the quasi-stable case, Mode II, is shown in Figure 4.5 for a fuel mixture consisting of 80% carbon monoxide and 20% hydrogen at an equivalence ratio of 0.42 and an inlet temperature of 300 K. The cycle is characterized by periodic shedding of a wake vortex from the step. A vortex is formed at the edge of the step when the flow acceleration is at its maximum, and the vortex formed in the previous cycle separates from the step (1). The new vortex grows, trapping a pocket of reactants between it and the previous vortex, while both vortices are convected downstream. This pocket of reactants is gradually consumed during the first half of the subsequent cycle. The heat release rate and pressure oscillations in this mode are approximately 90° out of phase—the margin of instability—and thus the amplitude of the pressure oscillations is relatively low at approximately 200 Pa.

Moreover, the vortex formed in the previous cycle continues to convect downstream. The burning of the pocket between the advancing vortices occurs gradually

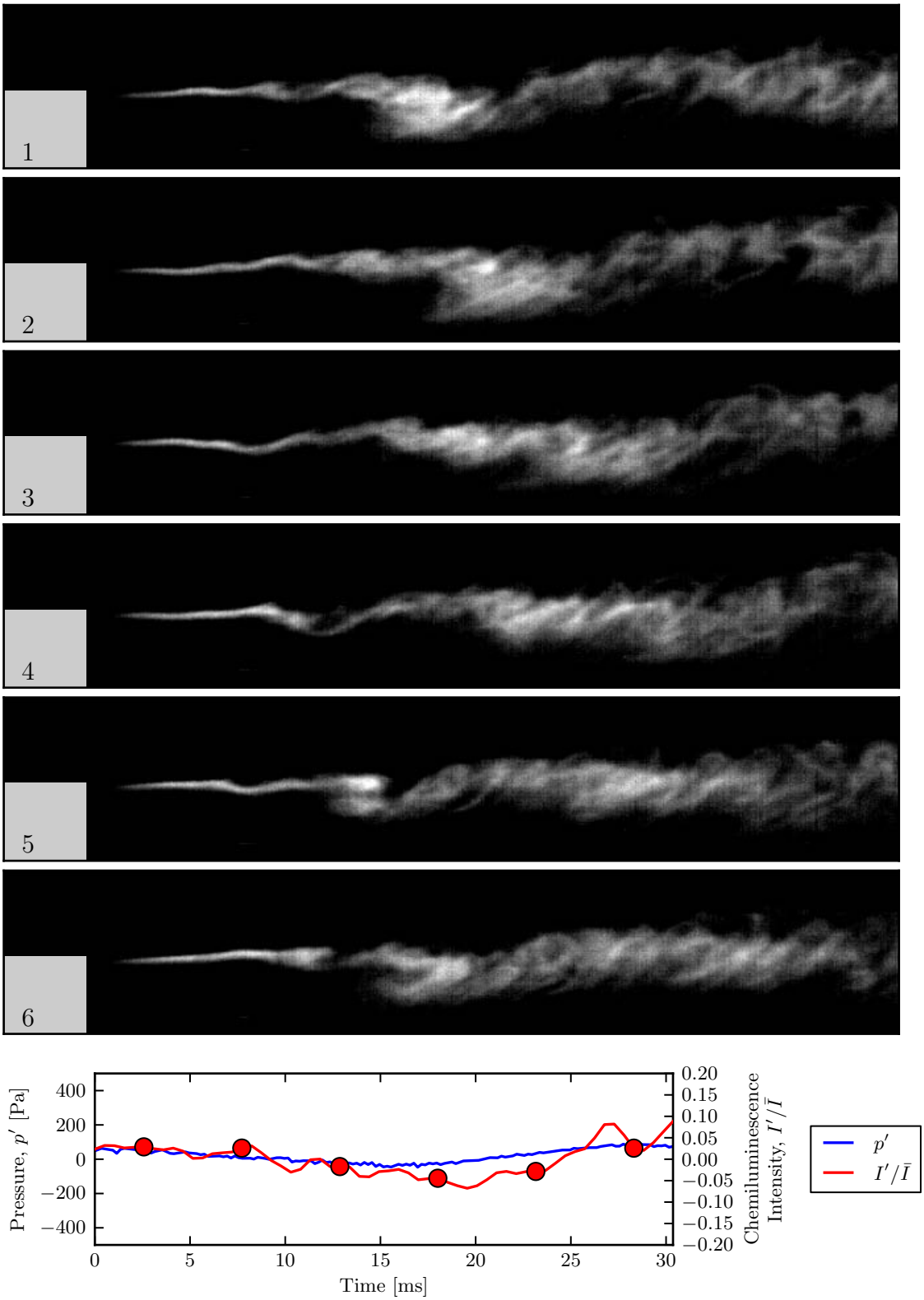

Figure 4.4: Flame chemiluminescence image sequence typical of Mode I.

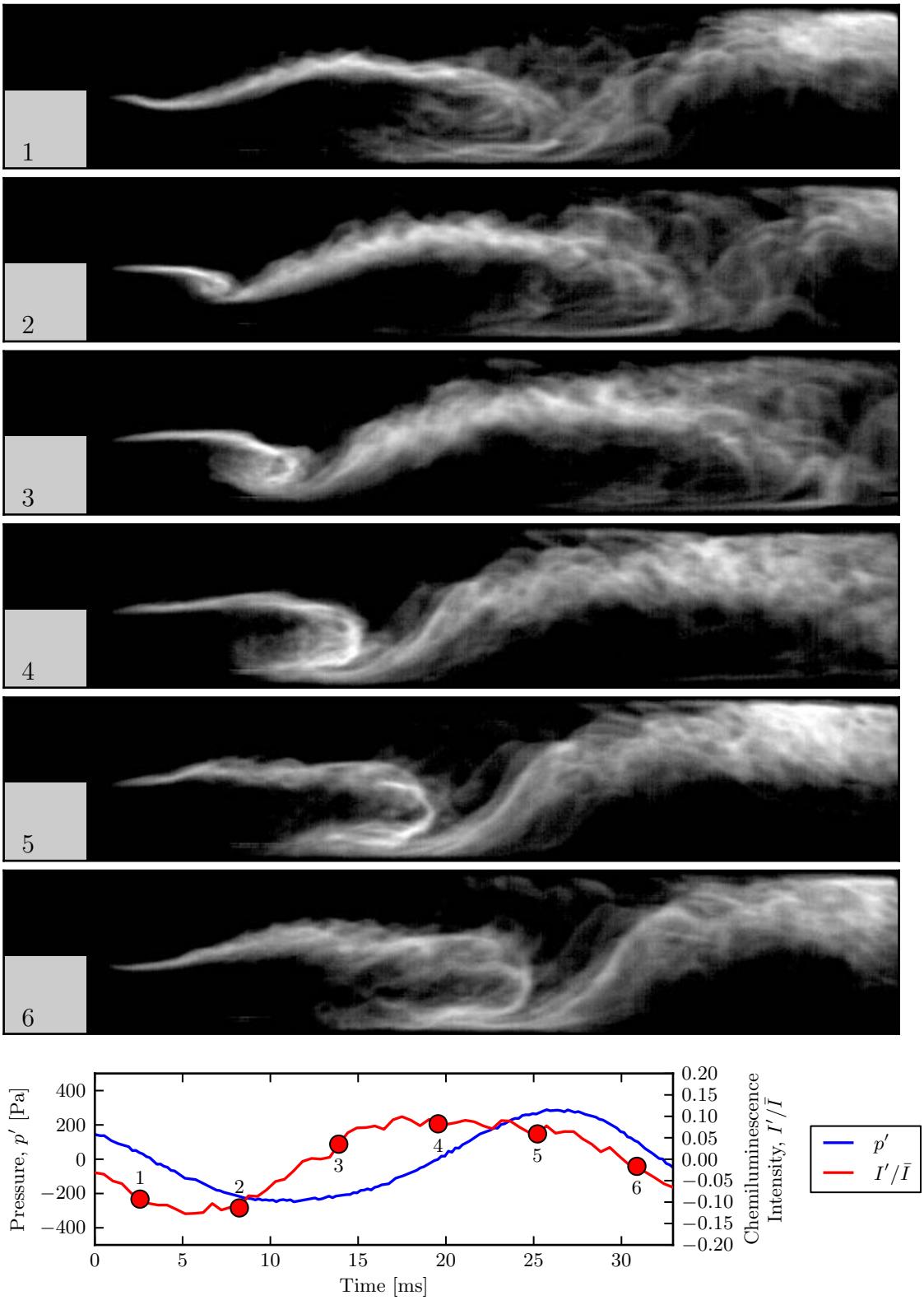

Figure 4.5: Flame chemiluminescence images for a typical cycle in Mode II.

and produces weak heat release rate fluctuations. The delay in burning the pocket affects the phase between heat release rate oscillations and pressure oscillations.

A sequence of images corresponding to a cycle of the unstable mode, Mode IIIa, is shown in Figure 4.6 for a fuel mixture composed of 80% carbon monoxide and 20% hydrogen at an equivalence ratio of 0.44 and an inlet temperature of 300 K. In this mode, a vortex is again shed from the recirculation zone downstream of the step (1). As in the quasi-stable case, the vortex grows, forming a pocket of unburned reactants between itself and the flame that formed at the end of the previous cycle (2–3). The high amplitude of the velocity oscillations—in excess of the mean flow velocity—force the leading edge of the flame upstream of the step during part of the cycle (3–4). Compared to the quasi-stable case, the vortex is larger and its size is limited by the upper wall of the combustor. The pocket is consumed rapidly, causing the heat release rate to reach a maximum (4–5). Recirculation caused by a secondary vortex formed on the top wall of the combustor enhances the burning of the pocket. The presence of the secondary recirculation zone along the upper wall, downstream of the step was previously identified numerically and experimentally in non-reacting flows at similar Reynolds numbers [3, 28]. As the pressure drops from its maximum value, the heat release rate drops rapidly and a new vortex forms at the step (6) and the cycle repeats. The positive feedback between this unsteady heat release rate and the pressure feeds the instability of the combustor, leading to pressure oscillations with an amplitude in excess of 2000 Pa.

In Figure 4.7, we show a sequence of images for a typical cycle of the high-frequency unstable mode, Mode IIIb, for a fuel mixture consisting of 100% propane at an equivalence ratio of 0.78 and an inlet temperature of 600 K. The frequency of the instability in this case is 132 Hz, corresponding to the 5/4-wave mode of the combustor. The evolution of the flame structure is similar to that observed in Mode IIIa. The higher frequency promotes a more compact vortex structure, although

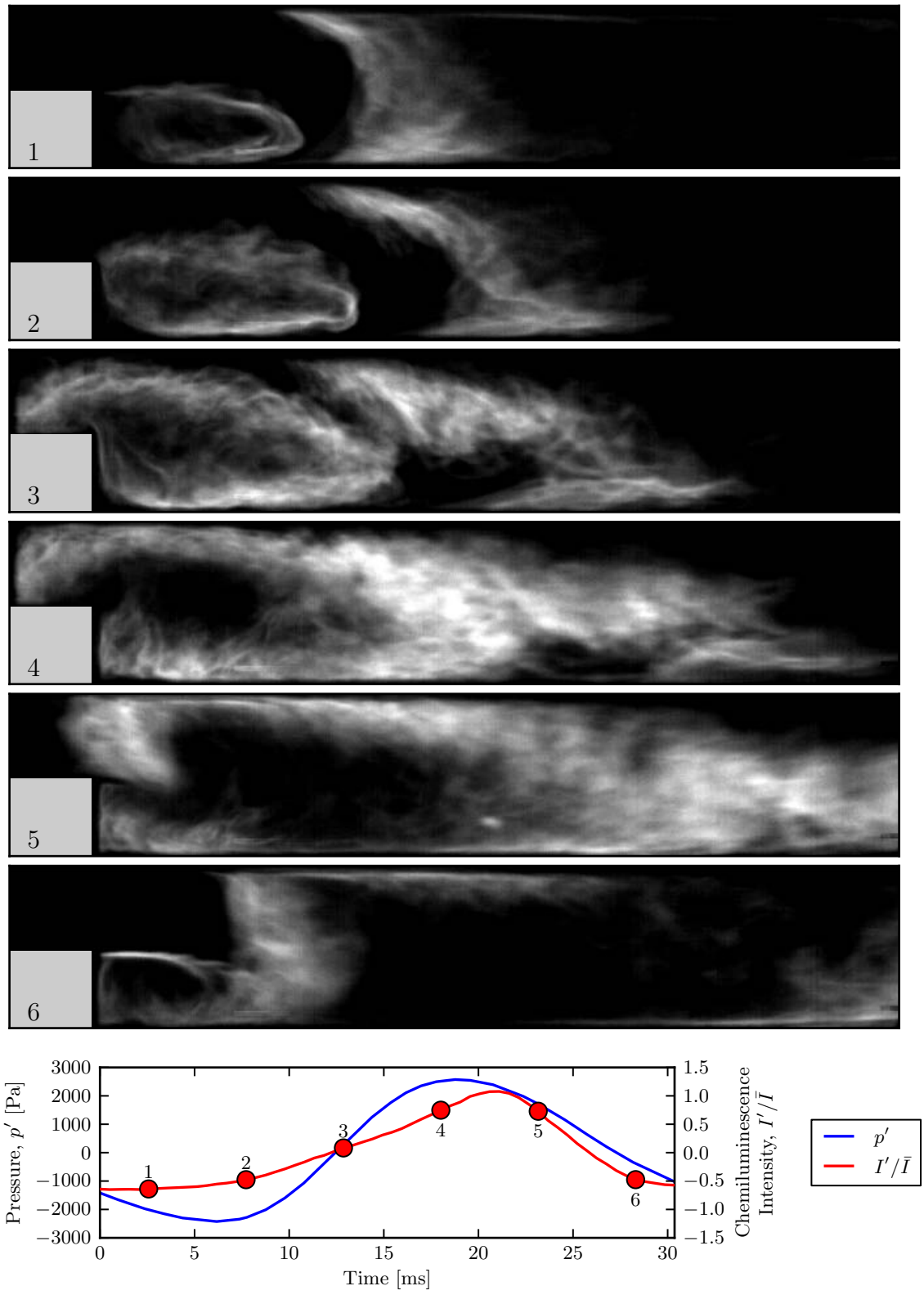

Figure 4.6: Flame chemiluminescence images for a typical cycle in Mode IIIa.

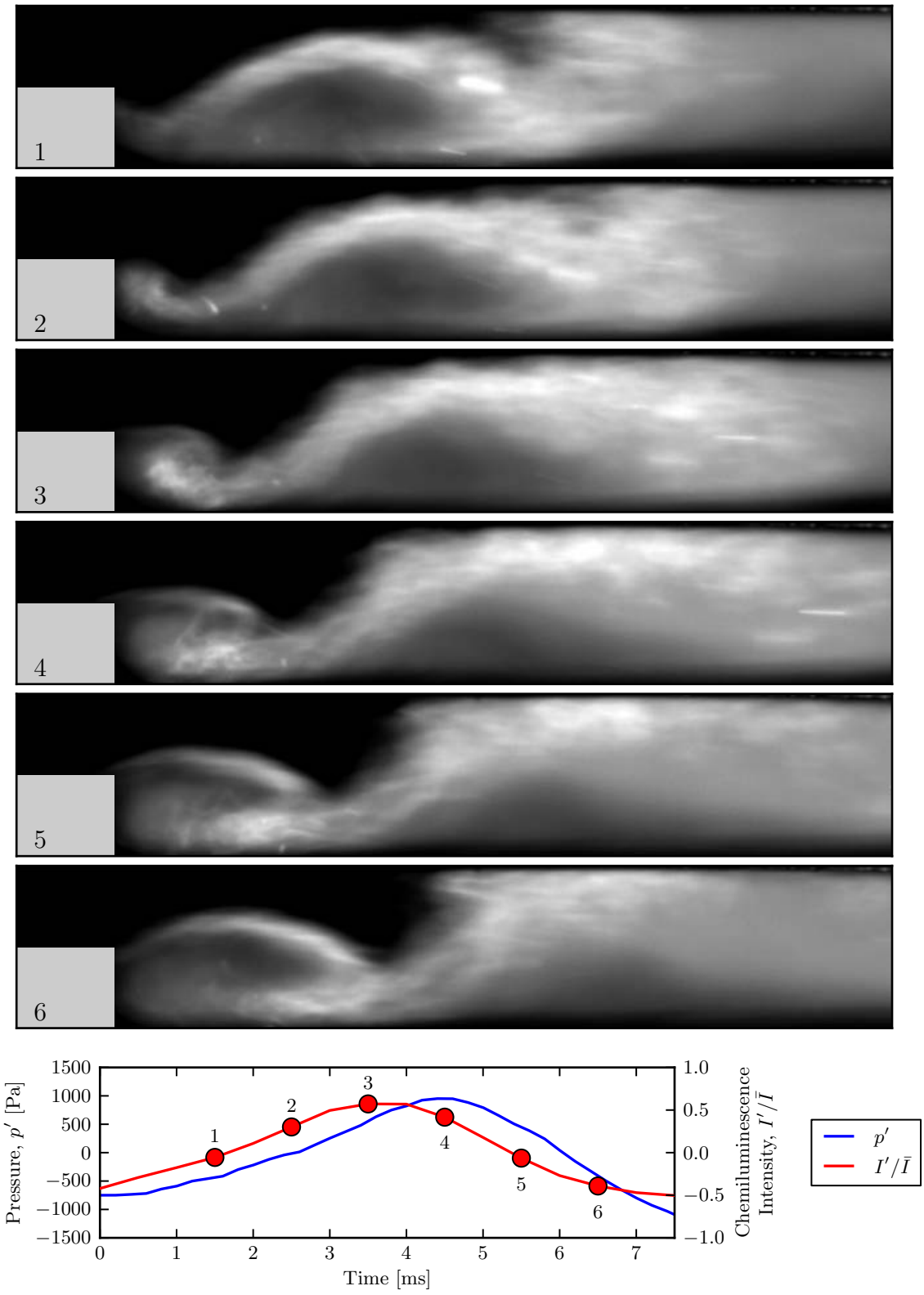

Figure 4.7: Flame chemiluminescence images for a typical cycle in Mode IIIb.

this is partially offset by the increase in inlet velocity associated with the elevated inlet temperature. The pressure oscillations in this mode are somewhat weaker than the low-frequency unstable mode, with an amplitude of approximately 1000 Pa.

4.4 Combustion Time-Delay Model

The combustion time-delay model developed in Section 3.5.2 can also be applied to the backward-facing step combustor. We have seen that unstable flames in the step combustor evolve over a longer period of time than in the swirl combustor, so the maximum allowable flame propagation time constant τ_f is taken to be $\tau_f < 1.25/f$, where f is the frequency of the acoustic mode. The phase between the velocity and the formation of the vortex in the recirculation zone is taken to be $\theta_{ur} = -90°$. This corresponds to the dynamic model for the step combustor developed by Altay et. al [1] which showed that the vortex formation begins at the moment of peak flow acceleration.

The acoustics of the backward-facing step combustor are quite similar to those of the swirl-stabilized combustor, and an analysis similar to that of Section 3.5.1 has been carried out for this geometry by Altay et al. [1]. This analysis showed that the acoustic modes of the step combustor fall near the $\beta = 0$ limit. The first three mode frequencies, corresponding to 1/4-, 3/4- and 5/4-wave mode shapes, are 36 Hz, 84 Hz, and 132 Hz, respectively.

Using the expected acoustic frequencies, and taking the phase between pressure and velocity oscillations to be $\pm 90°$ as determined by the model, we obtain the predicted instability bands of the backward-facing step combustor as shown in Figure 4.8. Starting at high flame speeds, the flame is coupled with acoustic mode at 132 Hz, corresponding to Mode IIIb of the combustor. When the flame speed decreases below the point where $\tau_f^{-1} = 105\,\mathrm{s}^{-1}$, the heat release rate and pressure

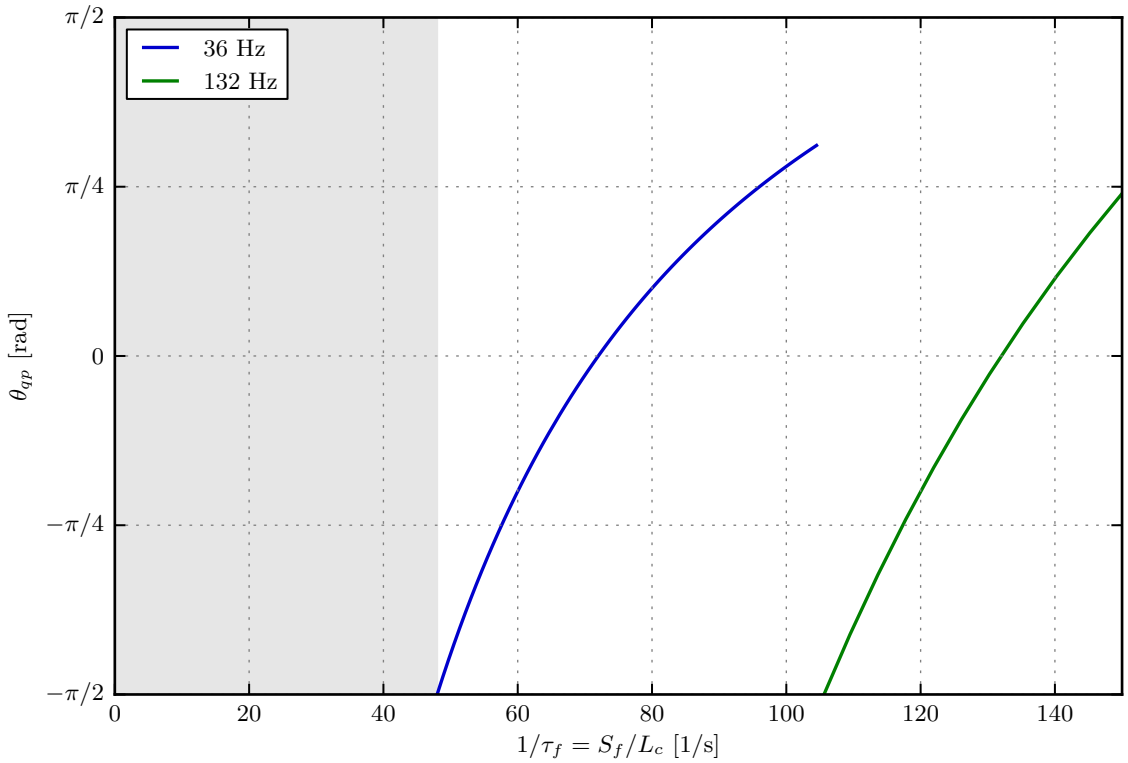

Figure 4.8: Predicted phase between heat release rate and pressure oscillations in the backward-facing step combustor as a function of flame speed.

oscillations at 132 Hz are no longer in phase, and the flame couples with the acoustic mode at 36 Hz, corresponding to Mode IIIa of the combustor where the pressure and heat release rate oscillations are in phase. Despite the existence of an unstable mode at 84 Hz, it is only unstable at flame speeds for which the 132 Hz mode is also unstable. This occlusion of the 84 Hz mode is reflected in the experimental results as well, where we see a direct transition between the instabilities at 132 Hz and 36 Hz. Further decreasing the flame speed causes the phase pressure and heat release rate oscillations at this frequency to grow until it reaches $-\pi/2$ at $\tau_f^{-1} = 44\,\mathrm{s}^{-1}$. Below this value of τ_f^{-1}, the flame is unable to couple with any of the acoustic modes, corresponding to the stable operating region (Mode I) of the combustor. The quasi-stable mode of the combustor (Mode II) is not predicted by this time-delay model. In the quasi-stable region, the phase between heat release rate and pressure is stable at

90° over a range of equivalence ratios, and correspondingly, flame speeds. For this to occur, there must be some non-linear effect which is not accounted for in the present model.

As we saw before for the swirl-stabilized combustor, the sequence of operating modes in the backward-facing step combustor can be explained by assuming that the phase between heat release rate and velocity oscillations is a consequence of a time delay which scales inversely with the flame speed. This implies that the kinematics of the flame propagating in the oscillating flow field determine the stability of the combustor, and that similar stability characteristics should be expected for fuel mixtures with similar flame speeds.

4.5 Strained Flame Model

In this section, we will apply a variant of the strained flame model developed in Section 3.6 to show that the operating modes of the backward-facing step combustor also obey a similarity relationship between the flame speed and the stretch rate. As before, we assume that the dependence of the operating modes on flame shape, flame speed and stretch rate can be expressed in the form of Equation 3.45. In order to find the appropriate constants, we look to the experimental data for distinct operating points that we can correlate with a particular flame shape and corresponding stretch rate and flame speed. Because the step combustor has fewer mode dynamic mode transitions than the swirl-stabilized combustor, and because we lack the heat release rate measurements from which to measure the phase between heat release rate and pressure under all operating conditions, there are just three identifiable operating points: the transition from Mode II to Mode I, the transition from Mode IIIa to Mode II, and the transition from Mode IIIb to Mode IIIa. A search of the space defined by the undetermined parameters p, q, b, and c introduced in Equation 3.45

reveals that the best fit for the experimental data occurs for $p = -0.5$, $q = -1.5$, and $b = c = 0$. The density-weighted flame speed is thus defined as:

$$\tilde{S} \equiv \left(\frac{\rho_u}{\rho_b}\right)^{-0.5} S^* = \left(\frac{\rho_u}{\rho_b}\right)^{-0.5} \frac{S_c}{U_u} \tag{4.1}$$

and density weighted stretch rate is:

$$\tilde{\kappa} \equiv \left(\frac{\rho_u}{\rho_b}\right)^{-1.5} \kappa^* = \left(\frac{\rho_u}{\rho_b}\right)^{-1.5} \frac{\kappa H}{U_u} \tag{4.2}$$

where H is the height of the backwards-facing step.

Figure 4.9 shows the density-weighted flame speed $\tilde{S}$ as a function of the density-weighted stretch rate $\tilde{\kappa}$ for each of the previously identified operating points. For each transition, the curves for all fuel compositions and inlet temperatures intersect (approximately) at a constant value of $\tilde{\kappa}$. Thus, for the step combustor, the relationship between $\tilde{S}$ and $\tilde{\kappa}$ is degenerate:

$$\tilde{\kappa} = 0.15 \tag{4.3}$$

This corresponds to stretch rates in the range of 400–800 s^{-1}, depending on the inlet conditions; κ increases with both equivalence ratio and inlet temperature.

We can now use this extraordinarily simple relationship to calculate the values of $\tilde{S}$ corresponding to the experimental conditions across all fuel compositions, equivalence ratios, and inlet temperatures, using the stretch rate indicated by Equation 4.3. In Figure 4.10, we show the overall sound pressure level as a function of $\tilde{S}$ for series of tests using propane–hydrogen fuel mixtures. For each inlet temperature and fuel composition, the transition between the quasi-stable and unstable modes (Mode II and Mode IIIa) occurs at $\tilde{S} = 0.010$. At higher inlet temperatures, the onset of the high-frequency unstable mode occurs at $\tilde{S} = 0.021$. From the time-delay model developed

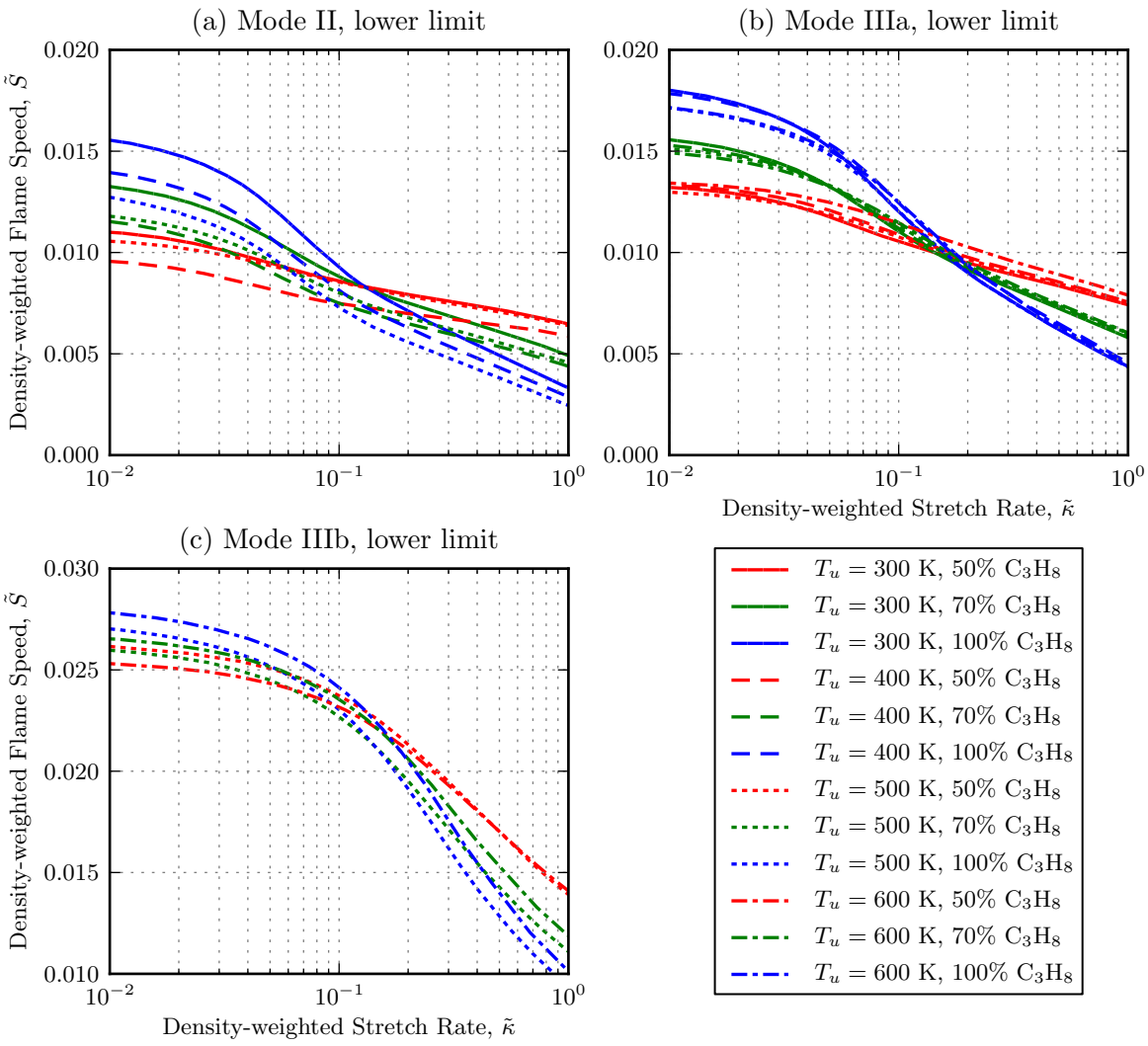

Figure 4.9: Density-weighted flame speed as a function of density-weighted stretch rate for selected operating points in the step combustor.

in Section 4.4, we expect that the ratio of these flame speeds should match the ratio of flame speeds at which $\theta_{qp} = -\pi/2$. From Figure 4.8, this ratio is 106 s^{-1}/48 s^{-1}= 2.21 for the model, which is very close to the ratio of 2.10 calculated from the experimental data.

The same relationship can also be used to transform the series of tests using syngas fuel mixtures, as shown in Figure 4.11. Again, the transition between Mode II and Mode IIIa is clustered around $\tilde{S} = 0.010$, though there is more scatter to the data here than in the case of the propane–hydrogen flames. In particular, the unstable mode

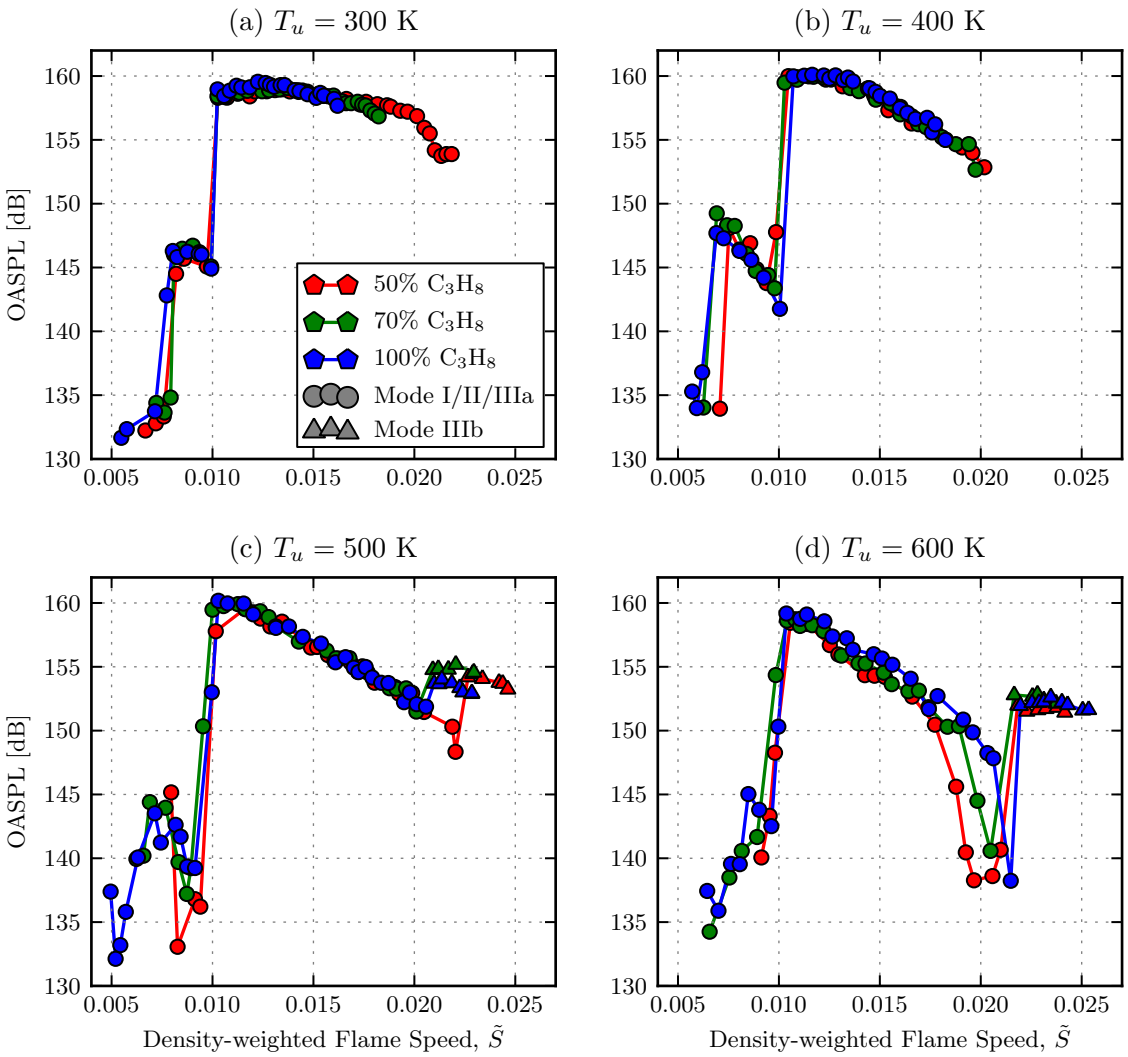

Figure 4.10: Overall sound pressure level as a function of density-weighted flame speed for all propane–hydrogen mixtures, equivalence ratios, and inlet temperatures in the backward-facing step combustor.

seems to last to slightly lower values of $\tilde{S}$ for the cases with the highest hydrogen concentrations in the fuel. In order to understand this trend, we first recognize that these cases have much lower equivalence ratios, and consequently flame temperatures, than the low-hydrogen fuel mixtures at the point of transition. This in turn leads to a (slight) shift in the acoustic frequency associated with the instability, and, according to the time-delay of Section 4.4, a different flame speed at the stability limit for that mode.

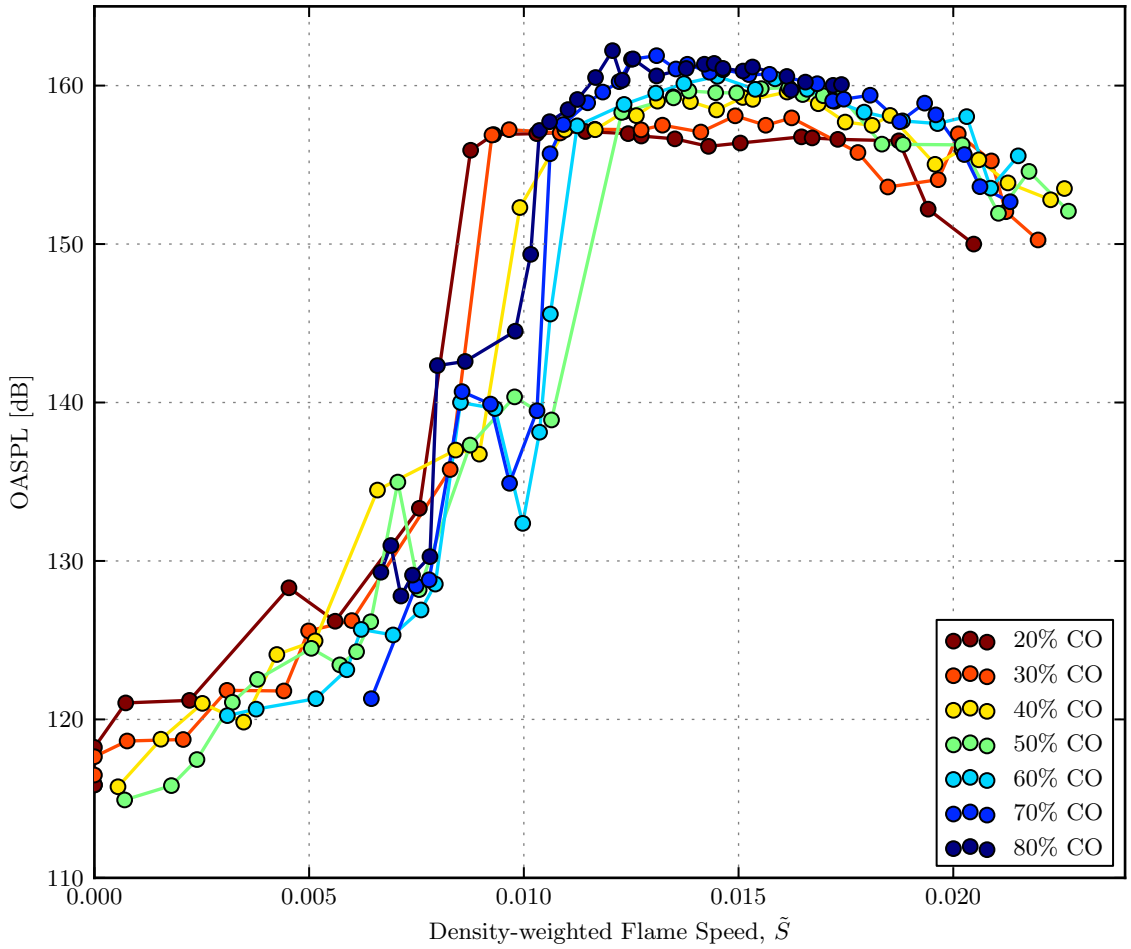

Figure 4.11: Overall sound pressure level as a function of density-weighted flame speed for syngas mixtures in the backward-facing step combustor.

4.6 Summary

In this chapter, we explored the dynamics of hydrogen-rich combustion in a laboratory-scale backwards-facing step combustor over a range of fuel compositions, equivalence ratios, and inlet temperatures. We found that there are a number of distinct operating modes, which can be characterized by the dynamic flame shape along with the amplitude and frequency of acoustic pressure oscillations in the combustor. The unstable modes are characterized by the periodic growth and shedding of a large wake vortex from the step. The formation and consumption of the pocket of reactants formed between each pair of vortices creates large flame area oscillations

and subsequent heat release rate oscillations.

The modeling tools developed to explain the dynamics of the swirl-stabilized combustor are applicable to the step combustor as well, and we used them to predict the unstable frequencies and relate the dynamic mode selection to the flame propagation speed. We developed a similarity transformation which converts the dependence of operating mode on inlet temperature, fuel composition, and equivalence ratio into a dependence on the density-weighted flame speed. The difference in the form of the similarity transformation reflects the differences in the combustor geometries. The dependence of the similarity transform on intrinsic properties of the inlet mixture demonstrates the importance of these local properties in determining the global system response.

Chapter 5

Conclusions

In this thesis, we studied premixed combustion of hydrogen-rich fuels in two laboratory-scale combustors: a planar backward-facing step combustor, and an axisymmetric swirl-stabilized combustor. Fuels consisting of carbon monoxide and hydrogen or propane and hydrogen were tested over a range of equivalence ratios and at various inlet temperatures. Dynamic pressure and chemiluminescence measurements were taken for each case. High-speed video and stereographic particle imaging velocimetry were used to explore the dynamic interactions between the flame and the flow field of the combustor.

Stable, quasi-stable and unstable operating modes were identified in each combustor, with each mode characterized by a distinct combination of dynamic flame shape, oscillation frequency, and pressure amplitude that depends on the composition of the reactants, the equivalence ratio, and the inlet temperature. In both combustors, we observe stable flames near the lean flammability limit. As the equivalence ratio increases, the flame becomes unstable, coupling at first with the lowest-frequency acoustic mode of the combustor, and then with higher-frequency acoustic modes at higher equivalence ratios. The quasi-stable and unstable modes are associated with flame–vortex interactions driven by acoustically-coupled velocity oscillations in the

flame-anchoring region. Velocity oscillation amplitudes in excess of the mean flow velocity accompany the unstable modes in each combustor.

In the planar combustor, the flame is convoluted around a large wake vortex, which is periodically shed from the step. The formation of a pocket of reactants between each pair of vortices and its subsequent consumption create flame area oscillations which lead to the heat release rate oscillations that sustain the instability.

In the swirl-stabilized combustor, the flame shape is controlled by the dynamics of the inner recirculation zone formed as a result of vortex breakdown. In the unstable mode, high-amplitude velocity oscillations in the flame-anchoring region result in the periodic growth and collapse of the inner recirculation zone, as well as oscillations in the strength of the annular jet which brings fresh reactants to the flame. The flame, anchored in the shear layer between the inner recirculation zone and the jet, grows along with the inner recirculation zone and is extinguished as the inner recirculation zone collapses.

The apparent similarity between the response curves and flame dynamics in the two combustors indicates that the intrinsic local dynamics, instead of global acoustics, govern the flame response. For both combustors, a linear model of the acoustics shows that the onset of combustion instability at a particular frequency can be related to a time delay between the velocity and the exothermic response of the flame that is inversely proportional to the local burning velocity. We show that for each combustor, the pressure response curves across a range of operating conditions can be collapsed onto a single curve by introducing an appropriate similarity parameter, the density-weighted strained flame consumption speed, that captures the response of the flame to the local flow dynamics. Simulations of stretched flames in hydrogen-rich fuels are used to define the form of the similarity parameter and compute its value at each combination of experimental parameters. The constants which define the similarity parameter are different in each combustor, reflecting the differences in flame anchoring

geometry.

This similarity transform works equally well for both experiments, across fuel compositions, and at different inlet temperatures, demonstrating that it fundamentally embodies the reciprocity between the flow and the combustion process that drives the instability. The analysis captures the impact of the fuel composition and operating temperature on the mode selection through an appropriately-weighted strained flame consumption speed, further emphasizing the influence of local transport–chemistry interactions on the system response.

Our results show a strong dependence of combustion dynamics on the strained flame consumption speed calculated at conditions which represent the local interaction between the flame and the surrounding flow field. This establishes several key requirements for numerical simulations which hope to accurately capture these kinds of dynamics. Simulations must resolve the flow at a scale where the the effects of stretch can influence the flame, and this information must be propagated to the flame model. This is especially true for hydrogen-rich fuels, where the effects of stretch on flame speed are the strongest. Furthermore, these results suggest that strained flame computations should be used to validate reduced chemical kinetic models if they are to be used in predicting the kinds of behavior demonstrated in these experiments.

The practical goal of studying combustion instability is to develop techniques for modifying combustor designs which eliminate it. In the absence of equivalence ratio oscillations, combustion instability is driven by interactions between the flame and the velocity field. Changes in the flame shape are dictated by the changes in the flame speed, which is determined by the composition of the inlet mixture and the geometry of the flame anchoring zone. So long as there are modes where the flame area responds to velocity perturbations, there will be flame speeds for which the combustor is unstable. In this situation, the best that we can do is to design the system such that, for some range of flame speeds, there are no unstable acoustic modes where

the pressure and heat release rate oscillations will be in phase. This can potentially be done either by changing the way the flame is anchored, and consequently the relationship between heat release rate and pressure, or by changing the resonant frequencies of the combustor.

The results obtained and models developed in this thesis have a number of implications for future studies of combustion dynamics, and particularly the dynamics associated with hydrogen-rich fuels. In order to develop the similarity transformation and produce the desired reduction of the experimental data, we needed to integrate models of processes occurring at several different scales to explain the combustor response: the acoustic model which incorporates the overall combustor geometry, the time-delay flame model which relates the velocity oscillations in the flame-anchoring zone to changes in the flame structure, and the strained flame model which relates the flame propagation to the local flow conditions and the properties of the fuel mixture. The most significant refinement that could be made to the model developed here would be to improve the bi-directional coupling between the constituent submodels. For instance, we have shown here that the response of the combustor depends on the flame speed, which in turn depends on the stretch rate experienced by the flame. While we have captured some of the dependence of the stretch rate on the flow field in our model, in principle the stretch rate should also be a function of the amplitude of the instability, which can only be predicted if we have a reasonable model for the acoustic damping present in the system. Likewise, there is the issue of the transfer function between the heat release rate and the acoustic pressure and velocity fields. We assumed that there was simply a time lag between the velocity and the flame, and were able to obtain reasonable predictions of the acoustic response using this model. Better predictions of the acoustic frequencies could be obtained by developing a flame transfer function that incorporated the kinematics of the flame front revealed from the PIV measurements and the response to stretch predicted by the strained

flame calculations. Improvements in all of these areas are necessary to advance our understanding of combustion dynamics driven by flame–vortex interactions and to develop models that can not only describe the combustion dynamics of a system, but also predict the conditions which will lead to thermoacoustic instability.

Bibliography

[1] H. M. Altay, R. L. Speth, D. E. Hudgins, and A. F. Ghoniem. Flame–vortex interaction driven combustion dynamics in a backward-facing step combustor. *Combustion and Flame*, 156(5):1111–1125, 2009.

[2] H. M. Altay, R. L. Speth, D. E. Hudgins, and A. F. Ghoniem. The impact of equivalence ratio oscillations on combustion dynamics in a backward-facing step combustor. *Combustion and Flame*, 156(11):2106–2116, 2009.

[3] B. F. Armaly, F. Durst, J. C. F. Pereira, and B. Schoenung. Experimental and theoretical investigation of backward-facing step flow. *Journal of Fluid Mechanics*, 127:473–496, 1983.

[4] D. Ascher, P. F. Dubois, K. Hinsen, J. Hugunin, and T. Oliphant. *Numerical Python*. Lawrence Livermore National Laboratory, Livermore, CA, 1999. UCRL-MA-128569.

[5] N. Bouvet, S.-Y. Lee, I. Gökalp, and R. J. Santoro. Flame speed characteristics of syngas (H_2–CO) with straight burners for laminar premixed flames. In *Third European Combustion Meeting*, 2007.

[6] K. N. C. Bray. Studies of the turbulent burning velocity. *Proceedings: Mathematical and Physical Sciences*, 431(1882):315–335, 1990.

[7] S. M. Candel and T. J. Poinsot. Flame stretch and the balance equation for the flame area. *Combustion Science and Technology*, 70:1–15, 1990.

[8] S. H. Chung and C. K. Law. An invariant derivation of flame stretch. *Combustion and Flame*, 55:123–125, 1984.

[9] A. Collette. H5Py: A Python interface to the HDF5 library, 2010.

[10] J. J. Conti, P. D. Holtberg, J. A. Beamon, A. M. Schaal, G. E. Sweetnam, and A. S. Kydes. Annual energy outlook. Technical Report DOE/EIA-0383(2009), Energy Information Administration, 2009.

[11] C. J. Dasch. One-dimensional tomography: A comparison of Abel, onion-peeling, and filtered backprojection methods. *Applied Optics*, 31(8):1146–1152, March 1992.

[12] J. David and H. Herzog. The cost of carbon capture. In *Fifth International Conference on Greenhouse Gas Control Technologies*, 2000.

[13] L. P. H. de Goey and J. H. M. ten Thije Boonkkamp. A flamelet description of premixed laminar flames and the relation with flame stretch. *Combustion and Flame*, 119:253–271, 1999.

[14] A. P. Dowling and S. R. Stow. Acoustic analysis of gas turbine combustors. *Journal of Propulsion and Power*, 19(5):751–764, 2003.

[15] D. R. Englund and W. B. Richards. The infinite line pressure probe. Technical Report NASA TM-83582, National Aeronautics and Space Administration, 1984.

[16] D. Fritsche, M. Furi, and K. Boulouchos. An experimental investigation of thermoacoustic instabilities in a premixed swirl-stabilized flame. *Combustion and Flame*, 151:29–36, 2007.

[17] J. L. Gauducheau, B. Denet, and G. Searby. A numerical study of lean CH_4/H_2/air premixed flames at high pressure. *Combustion Science and Technology*, 137:81–99, 1998.

[18] A. G. Gaydon. *The Spectroscopy of Flames*. Chapman and Hall, London, 1974.

[19] A. F. Ghoniem, A. Annaswamy, D. Wee, T. Yi, and S. Park. Shear flow-driven combustion instability: Evidence, simulation, and modeling. *Proceedings of the Combustion Institute*, 29:53–60, 2002.

[20] D. Goodwin. Cantera: Object-oriented software for reacting flows, 2005.

[21] B. Higgins, M. Q. McQuay, F. Lacas, and S. Candel. An experimental study on the effect of pressure and strain rate on CH chemiluminescence of premixed fuel-lean methane/air flames. *Fuel*, 80(11):1583–1591, 2001.

[22] A. C. Hindmarsh, P. N. Brown, K. E. Grant, S. L. Lee, R. Serban, D. E. Shumaker, and C. S. Woodward. SUNDIALS: Suite of nonlinear and differential/algebraic equation solvers. *ACM Transactions on Mathematical Software*, 31(3):363–396, 2005.

[23] Y. Huang and V. Yang. Bifurcation of flame structure in a lean-premixed swirl-stabilized combustor: transition from stable to unstable flame. *Combustion and Flame*, 136(3):383–389, 2004.

[24] J. D. Hunter. Matplotlib: A 2D graphics environment. *Computing in Science & Engineering*, 9(3):90–95, 2007.

[25] G. S. Jackson, R. Sai, J. M. Plaia, C. M. Boggs, and K. T. Kiger. Influence of H_2 on the response of lean premixed CH_4 flames to high strained flows. *Combustion and Flame*, 132:503–511, 2003.

[26] E. Jones, T. Oliphant, P. Peterson, et al. SciPy: Open source scientific tools for Python, 2001–.

[27] G. A. Karim, I. Wierzba, and Y. Al-Alousi. Methane–hydrogen mixtures as fuels. *International Journal of Hydrogen Energy*, 21(7):625–631, 1996.

[28] J. Kim and P. Moin. Application of a fractional-step method to incompressible Navier-Stokes equations. *Journal of Computational Physics*, 59:308–323, 1985.

[29] C. K. Law. Dynamics of stretched flames. *Proceedings of the Combustion Institute*, 22:1381–1402, 1988.

[30] C. K. Law. *Combustion Physics*. Cambridge University Press, 2006.

[31] T. Lieuwen, V. McDonnell, E. Petersen, and D. Santavicca. Fuel flexibility influences on premixed combustor blowout, flashback, autoignition and stability. 2006. ASME Paper GT2006-90770.

[32] T. Lieuwen, H. Torres, C. Johnson, and B. T. Zinn. A mechanism of combustion instability in lean premixed gas turbine combustors. *Journal of Engineering for Gas Turbines and Power*, 123:182–189, 2001.

[33] L. Lombardi. Life cycle assessment comparison of technical solutions for CO_2 emissions reduction in power generation. *Energy Conversion and Management*, 44(1):93–108, 2003.

[34] F. Lundh. Python imaging library (PIL), 2009.

[35] Y. M. Marzouk. The effect of flow and mixture inhomogeneity on the dynamics of strained flames. Master's thesis, Massachusetts Institute of Technology, August 1999.

[36] Y. M. Marzouk, A. F. Ghoniem, and H. N. Najm. Toward a flame embedding model for turbulent combustion simulation. *AIAA Journal*, 41(4):641–652, 2003.

[37] M. Matalon and B. J. Matkowsky. Flames as gasdynamic discontinuities. *Journal of Fluid Mechanics*, 124:239–259, 1982.

[38] A. J. Minchener. Coal gasification for advanced power generation. *Fuel*, 84(17):2222 – 2235, 2005. The 5th European Conference on Coal Research and its Applications.

[39] R. F. D. Monaghan. *Dynamic Reduced Order Modeling of Entrained Flow Gasifiers*. PhD thesis, Massachusetts Institute of Technology, 2009.

[40] J. Natarajan, T. Lieuwen, and J. Seitzman. Laminar flame speeds of H_2/CO mixtures: Effect of CO_2 dilution, preheat temperature, and pressure. *Combustion and Flame*, 151:104–119, 2007.

[41] T. E. Oliphant. Python for scientific computing. *Computing in Science & Engineering*, 9(3):10–20, 2007.

[42] F. Pérez and B. E. Granger. IPython: A system for interactive scientific computing. *Computing in Science & Engineering*, 9(3):21–29, May 2007.

[43] T. J. Poinsot, A. C. Trouve, D. P. Veynante, S. M. Candel, and E. Esposito. Vortex-driven acoustically coupled combustion instabilities. *Journal of Fluid Mechanics*, 177:265–292, 1987.

[44] L. Rayleigh. The explanation of certain acoustic phenomena. *Nature*, 18:319–321, 1878.

[45] J.-C. Saghbini. Simulation of vorticity dynamics in swirling flows, mixing and vortex breakdown. Master's thesis, Massachusetts Institute of Technology, 1997.

[46] J.-C. Saghbini and A. F. Ghoniem. Numerical simulation of the dynamics and mixing in a swirling flow. 1997. AIAA Paper AIAA-1997-507.

[47] J. M. Samaniego, F. N. Egolfopoulos, and C. T. Bowman. CO_2^* chemiluminescence in premixed flames. *Combustion Science and Technology*, 109:183–203, 1995.

[48] K. C. Schadow and E. Gutmark. Combustion instability related to vortex shedding in dump combustors and their passive control. *Progress in Energy and Combustion Science*, 18(2):117–132, 1992.

[49] M. Slack and A. Grillo. High temperature rate coefficient measurements of CO + O chemiluminescence. *Combustion and Flame*, 59:189–196, 1985.

[50] G. P. Smith, D. M. Golden, M. Frenklach, N. W. Moriarty, B.Eiteneer, M. Goldenberg, C. T. Bowman, R. K. Hanson, J. S. Songand W. C. Gardiner, V. V. Lissianski, and Z. Qin. GRI-Mech 3.0. `http://www.me.berkeley.edu/gri_mech/`.

[51] M. C. Soteriou and A. F. Ghoniem. The vorticity dynamics of an exothermic, spatially developing, forced, reacting shear layer. *Proceedings of the Combustion Institute*, 25:1265–1272, 1994.

[52] R. L. Speth, Y. M. Marzouk, and A. F. Ghoniem. Impact of hydrogen addition on flame response to stretch and curvature. In *41st Aerospace Sciences Meeting*. AIAA, 2005.

[53] C. Uykur, P. F. Henshaw, D. S.-K. Ting, and R. M. Barron. Effects of addition of electrolysis products on methane/air premixed laminar combustion. *International Journal of Hydrogen Energy*, 26:265–273, 2001.

[54] H. A. van der Vorst. Bi-CGSTAB: A fast and smoothly converging variant of Bi-CG for the solution of nonsymmetric linear systems. *SIAM Journal on Scientific Computing*, 13:631–644, 1992.

[55] K. K. Venkataraman, L. H. Preston, D. W. Simons, B. J. L. andJ. G. Lee, and D. A. Santavicca. Mechanism of combustion instability in a lean premixed dump combustor. *Journal of Propulsion and Power*, 15(6):909–918, 1999.

[56] R. Villarreal and P. L. Varghese. Frequency-resolved absorption tomography with tunable diode lasers. *Applied Optics*, 44:6786–6795, 2005.

[57] D. M. Wicksall and A. K. Agrawal. Acoustics measurements in a lean premixed combustor operated on hydrogen/hydrocarbon fuel mixtures. *International Journal of Hydrogen Energy*, 32:1103–1112, 2007.

[58] F. A. Williams. Chemical-kinetic mechanisms for combustion applications, December 2005.

[59] Q. Zhang, D. R. Noble, and T. Lieuwen. Characterization of fuel composition effects in $H_2/CO/CH_4$ mixtures upon lean blowout. *Journal of Engineering for Gas Turbines and Power*, 129:688–694, 2007.